

UVM ScholarWorks

Mechanistic Insights Into Nitrogen-Doped Carbon Quantum Dot- Per-And Polyfluoroalkyl Substances (pfas) Interactions In Drinking Water For Advanced Optical Sensing

Item Type	thesis;article
Authors	Chonnambi, Abhina
Download date	2026-05-13 09:44:28
Link to Item	https://hdl.handle.net/20.500.14849/4143

MECHANISTIC INSIGHTS INTO NITROGEN-DOPED CARBON
QUANTUM DOT– PER-AND POLYFLUOROALKYL SUBSTANCES
(PFAS) INTERACTIONS IN DRINKING WATER FOR ADVANCED
OPTICAL SENSING

A Thesis Presented

by

Abhina Chonnambi

to

The Faculty of the Graduate College

of

The University of Vermont

In Partial Fulfilment of the Requirements
For the Degree of Master of Science
Specializing in Civil and Environmental Engineering

October, 2025

Defense date: July 29, 2025
Thesis Examination committee:

Appala Raju Badireddy, Ph.D., Advisor
Rory Waterman, Ph.D., Chairperson
Matthew Scarborough, Ph.D.
Holger Hooch, DPhil, Dean of the Graduate College

ABSTRACT

Per- and polyfluoroalkyl substances (PFAS) have become integral to modern life due to their unique chemical and physical properties. However, growing concerns persist regarding their toxicity and environmental persistence. Current detection methods - primarily chromatographic techniques coupled with mass spectrometry- are accurate but costly, time-intensive, and confined to laboratory settings. To more effectively evaluate human exposure risks, there is a pressing need for a simpler, faster, and more affordable detection approach that is well-suited for field deployment.

This study presents a novel optical sensing approach employing nitrogen-doped carbon quantum dots (N-CDs) for detection of PFAS in drinking water. Existing PFAS sensors often face challenges related to limited selectivity, sensitivity, and portability. In response, this research aims to establish a foundation for the deployment of practical, field-deployable sensors. As an initial step, we explored the interaction mechanisms between N-CDs and five PFAS compounds regulated by the U.S. Environmental protection Agency (EPA): perfluorooctanoic acid (PFOA), perfluorooctane sulfonic acid (PFOS), perfluorohexanoic acid (PFHxA), perfluorononanoic acid (PFNA), and nonafluorobutane-1-sulfonic acid (PFBS), selected for their diverse carbon chain lengths and functional groups.

To elucidate these interactions, we conducted a comprehensive suite of physicochemical characterizations, including hydrodynamic size, zeta potential, UV-vis absorbance, and fluorescence properties. Bond formation and surface chemistry changes were further confirmed using X-ray photoelectron spectroscopy (XPS). These analysis enabled us to monitor binding interactions and aggregation behavior, offering crucial insights into the sensitivity and selectivity of N-CDs toward the target PFAS compounds.

Our findings indicate that PFAS compounds with similar functional groups exhibit comparable interaction profiles, with electrostatic interactions emerging as the dominant mechanism. Selectivity assessment revealed that the primary interferences stem from structurally similar PFAS, underscoring the potential of this N-CDs based sensing platform to differentiate among various PFAS types. Overall, this work provides a fundamental understanding of the physicochemical interactions between N-CDs and PFAS, paving the way for the development of highly selective and sensitive optical sensors for real-time monitoring of drinking water quality.

ACKNOWLEDGEMENTS

Words cannot express my gratitude for the support and encouragement that Dr. Appala Raju Badireddy has provided me throughout my research journey. From the moment I proposed my research proposal to the defence committee they provided me with valuable feedback that pushed me to take my work further than I ever thought it could go. The feedback from Dr. Rory Waterman, Dr. Matthew Scarborough and Dr. Gregory Rowangould is highly acknowledged. The contributions of additional researchers Monireh Dehabadi and Taylore Dall are recognized and appreciated.

Furthermore, I would like to express my heartfelt gratitude to the National Science Foundation/Experimental Program to Stimulate Competitive Research (NSF EPSCoR) Grant OIA- 2418750 for funding this research. I am also fortunate to have had the support of my lab mates, Eshita Jhahan, Monireh Dehabadi, Kehinde Ojasanya, Cooper Petrie, and Sajjad Eftekhari whose camaraderie and encouragement have been invaluable throughout my graduate journey.

Finally, I would like to appreciate the support and encouragement that my parents and family provided me during my work. This unwavering support and encouragement kept me motivated during hard times. I could never complete my thesis without their support.

TABLE OF CONTENTS

ACKNOWLEDGEMENTS.....	ii
LIST OF TABLES.....	v
LIST OF FIGURES.....	vi
1. INTRODUCTION.....	1
2.LITERATURE REVIEW.....	4
2.1 Per- and polyfluoroalkyl substances (PFAS).....	4
2.2 Overview of existing sensors for PFAS.....	6
2.3 Current limitations in PFAS sensor technology that hinder compliance with EPA standards and practical field use.....	11
2.4 Summary of optical-based sensors	12
3. OVERALL GOAL AND OBJECTIVE.....	14
3.1 Overall Goal.....	14
3.2 Objectives.....	15
4. MATERIALS AND METHODS.....	16
4.1 Materials.....	16
4.2 Material characterization.....	16
4.3 Effect of pH on N-CDs fluorescence.....	19
4.4 N-CDs properties with PFOA at pH 4.0.....	19
4.5 Sensitivity test with five PFAS.....	20
4.6 Background ions effect.....	21
4.7 Statistical analysis.....	22
5. RESULTS AND DISCUSSION.....	22
5.1 Characterization of N-CDs in ultrapure water.....	22
5.1.1 Size and zeta potential.....	22
5.1.2 Absorbance and fluorescence of N-CDs.....	25
5.1.3 Stern-Volmer plot.....	28

5.1.4 Elemental composition and chemical bonding.....	30
5.1.5 Effect of pH on N-CDs fluorescence.....	33
5.2 Preliminary study with PFOA.....	34
5.3 Hypothesized interaction mechanism.....	37
5.4 Detailed study of five individual PFAS.....	41
5.4.1 Perfluorooctanoic acid (PFOA).....	41
5.4.2 Perfluorooctane sulfonic acid (PFOS).....	44
5.4.3 Perfluorohexanoic acid (PFHxA).....	46
5.4.4 Perfluorononanoic acid (PFNA).....	49
5.4.5 Nonafluorobutane-1-sulfonic acid (PFBS).....	51
5.5 Comparing the size and zeta potential based on chain length.....	53
5.6 Selectivity test.....	56
5.7 Elemental composition and bonding information after the addition of PFAS.....	57
5.8 Mechanistic interactions between PFAS and N-CDs.....	63
5.8.1 Electrostatic interactions.....	63
5.8.2 Hydrophobic interactions.....	66
6. CONCLUSIONS.....	68
7. RECOMMENDATION FOR FUTURE WORK.....	70
8. INTELLECTUAL MERITS AND BROADER IMPACTS.....	72
9. REFERENCES.....	74

LIST OF TABLES

Table 2.1. Presents current state of optical-based sensors developed for detecting targeted PFAS.	12
Table 3.1. List of five PFAS regulated by the EPA used in the sensing mechanism study	15
Table 5.1. Stability behaviour of colloidal suspension to zeta potential values.	24
Table 5.2. XPS elemental composition and peak parameters of N-CDs	32
Table 5.3. Bond information from C1s spectrum	32
Table 5.4. Elemental composition of N-CDs after interaction with PFOA	59
Table 5.5. Elemental composition of N-CDs after interaction with PFOS	61

LIST OF FIGURES

Figure 4.1. (a) Dynamic light scattering (DLS) (b) Nanoparticle track analyzer NTA.....	17
Figure 4.2. (a) Prepared N-CDs and PFAS-interacted samples for XPS analysis; b) Sample loading onto the XPS holder; (c) Drop-casting of samples on TEM grid; and (d) TEM grid loaded for imaging.....	18
Figure 4.3. Schematic representation of the experimental procedure for analyzing the interaction between nitrogen-doped carbon dots (N-CDs) and PFAS.....	20
Figure 5.1. TEM images of N-CDs (a) (magnification = 3000×) (b) (magnification 12000×) (c) (magnification =12000×) (d) Histogram of particle size distribution for nitrogen-doped carbon dots (N-CDs) obtained from TEM analysis. All images were taken at accelerating voltage of 80 kV. The orange bars represent the frequency of particle sizes binned across measured diameters, while the red curve indicates the Gaussian fit applied to the data. The average particle size of the N-CDs was calculated to be 25.6 ± 0.44 nm suggesting a narrow and symmetric size distribution.....	23
Figure 5.2. Absorbance and fluorescence spectrum of N-CDs in ultrapure water at pH 6.9.....	27
Figure 5.3. The images show N-CDs solution under (a) ambient light and (b) UV-A light.....	27
Figure 5.4. Schematic Stern–Volmer plot showing the transition from fluorescence quenching to enhancement with increasing PFOA concentration.....	30
Figure 5.5. (a) Wide scan spectrum of nitrogen-doped carbon dots (N-CDs) showing the presence of Na 1s, O 1s, N 1s, C 1s, Cl 2p, and Si 2p peaks. (b) High resolution C1s spectra of N-CDs, (c) High resolution O 1s spectrum of N-CDs (d) High resolution N1s spectra of N-CDs.....	31
Figure 5.6. Potential surface functional groups of nitrogen-doped carbon dots (N-CDs).....	33
Figure 5.7. Fluorescence emission spectra of nitrogen-doped carbon dots (N-CDs) at different pH values ranging from 3 to 8. The emission wavelength is 490nm.....	34
Figure 5.8. Hydrodynamic size of N-CDs with the addition of 5 mg/L PFOA incubation time (after 10 min and 72 h) with no mixing at ambient temperature. The size 98.32 nm represents the well-vortexed initial condition of the N-CDs at pH 6.9.....	35
Figure 5.9. Zeta potential of N-CDs with the addition of 5 mg/L PFOA and	

incubation time (after 10 min and 72 h) with no mixing at ambient temperature. The size 98.32 nm represents the well-vortexed initial condition of the N-CDs at pH 6.9.....	37
Figure 5.10. Speciation diagram of carboxyl amine.....	38
Figure 5.11. Potential electrostatic interaction between PFOA and N-CDs at pH 4.....	39
Figure 5.12. Representing the change in absorbance of N-CDs with the addition of 5mg/L PFOA.....	39
Figure 5.13. Representing the change in fluorescence of N-CDs with the addition of 5mg/L PFOA.....	40
Figure 5.14. Effect of hydrodynamic size and zeta potential of N-CDs at different concentration of PFOA (1-7.5 ppm) at pH 4 ultrapure water.....	42
Figure 5.15. Stern – Volmer plot showing the variation in fluorescence intensity of N-CDs by the addition of PFOA at pH 4.....	43
Figure 5.16 Schematic illustration depicting the trends in (a) hydrodynamic size and (b) zeta potential of N-CDs with increasing PFOA concentration, highlighting the mechanisms responsible for these changes.....	43
Figure 5.17. Effect of hydrodynamic size and zeta potential of N-CDs at different concentration of PFOS (1-7.5 ppm) at pH 4 ultrapure water.....	45
Figure 5.18. Stern–Volmer plot showing the variation in fluorescence intensity of N-CDs by the addition of PFOS (1-7.5 ppm) at pH 4.....	46
Figure 5.19. Effect of hydrodynamic size and zeta potential of N-CDs at different concentration of PFHxA (1-7.5 ppm) at pH 4 ultrapure water.....	47
Figure 5.20. Stern–Volmer plot showing the variation in fluorescence intensity of N-CDs by the addition of PFHxA (1-7.5 ppm) at pH 4.....	48
Figure 5.21. Effect of hydrodynamic size and zeta potential of N-CDs at different concentration of PFNA (1-7.5 ppm) at pH 4 ultrapure water.....	49
Figure 5.22. Stern–Volmer plot showing the variation in fluorescence intensity of N-CDs by the addition of PFNA (1-7.5 ppm) at pH 4.....	50

Figure 5.23. Effect of hydrodynamic size and zeta potential of N-CDs at different concentration of PFBS (1-7.5 ppm) at pH 4 ultrapure water.....	51
Figure 5.24. Stern–Volmer plot showing the variation in fluorescence intensity of N-CDs by the addition of PFBS (1-7.5 ppm) at pH 4.....	53
Figure 5.25. Hydrodynamic size variation of N-CDs upon interaction with long- chain PFAS Compounds (PFOA, PFOS, PFNA) at pH 4.....	54
Figure 5.26. Hydrodynamic size variation of N-CDs upon interaction with long- chain PFAS Compounds (PFHxA, PFBS) at pH 4.....	54
Figure 5.27 (a) Zeta potential variation of N-CDs upon interaction with long –chain PFAS Compounds (PFOA, PFOS, PFNA) at pH 4.....	55
Figure 5.28 (a) Zeta potential variation of N-CDs upon interaction with long –chain PFAS Compounds (PFHxA, PFBS) at pH4.....	55
Figure 5.29. Fluorescence response $((F-F_0)/F_0)$ of nitrogen-doped carbon dots (N-CDs) upon interaction with different interfering ions (cations and anions), individual PFAS compounds (PFOS, PFHxA, PFNA, PFBS), and their mixture. Measurements were conducted at pH 4 with excitation at 365 nm.....	57
Figure 5.30. Wide scan spectrum of N-CDs with the interaction of PFOA showing the presence of Na 1s O 1s, N 1s, C 1s, F 1s, Cl 2p, and Si 2p peaks.....	58
Figure 5.31. High-Resolution C 1s XPS spectra of N-CDs after interaction with PFOA.....	59
Figure 5.32. High-Resolution N 1s XPS spectra of N-CDs after interaction with PFOA.....	60
Figure 5.33. High-Resolution O 1s XPS spectra of N-CDs after interaction with PFOA.....	60
Figure 5.34. Wide scan spectrum of N-CDs with the interaction of PFOS showing the presence of Na 1s O 1s, N 1s, C 1s, F 1s, Cl 2p, and Si 2p peaks.....	61
Figure 5.35. High-Resolution C 1s XPS spectra of N-CDs after interaction with PFOS.....	62

Figure 5.36. High-Resolution N1s XPS spectra of N-CDs after interaction with PFOS.....	62
Figure 5.37. High-Resolution O 1s XPS spectra of N-CDs after interaction with PFOS.....	63
Figure 5.38. (a) Electrostatic attraction and (b) Electrostatic repulsion.....	64
Figure 5.39. Hydrophobic interaction.....	66
Figure 5.40 Schematic mechanism between N-CDs and PFAS showing the combined effect of electrostatic and hydrophobic effect.....	67

1. INTRODUCTION

Per- and polyfluoroalkyl substances (PFAS) are a class of emerging environmental pollutants that are now ubiquitously present in the environment (Leung et al., 2023a). An estimated 18-80 million people in the United States consume drinking water with combined perfluorooctanoic acid (PFOA) and perfluorooctanesulfonic acid (PFOS) levels of 10 ng/L or higher, while 200 million people likely receive water with a PFOA and PFOS (Andrews & Naidenko, 2020). Even though there is no direct evidence showing that exposure to PFAS is linked to human death, several studies are showing that there is a positive correlation between exposure to certain PFAS and neurodevelopmental disorders in humans, immunotoxicity, various types of cancer, diabetes, high cholesterol, hypertension, attention deficit hyperactivity disorder (ADHD), and autism spectrum diseases (ASD)(Naidu et al., 2020),(Currie et al., 2024), (Qian et al., 2024). In the present scenario, there is an increased trait of ASD disease among children over these years, also making it suspicious how much this is linked with exposure to PFAS (Choi et al., 2024). A 2023 U.S. study revealed that 45.1% of respondents had never heard of PFAS, while 31.6% were unaware of its implications. Surprisingly, 97.4% of respondents did not believe their drinking water was affected by these chemicals (Berthold et al., 2023),(Smalling et al., 2023).

PFAS is an aliphatic substance containing a $-C_nF_{2n+1}$ (where n is at least 1) moiety within its structure, while the Organisation for Economic Cooperation and Development (OECD) / United Nations Environment programme (UNEP) global PFC Group proposed to include the chemical with at least one aliphatic perfluoro carbon moiety ($-C_nF_{2n-}$) as PFAS (Buck et al., 2011). The use of these compounds began nearly nine decades ago, in the 1930s, when scientists successfully replaced hydrogen

(H) with fluorine (F) bonded to carbon, creating one of the strongest bonds in organic chemistry. This breakthrough led to the development of 5,000 synthetic compounds (Lin et al., 2019) with unique physical and chemical properties that significantly improved human life often without people realizing their impact (Perera & Meegoda, 2024; Petkowski et al., 2024). Among all these chemicals, despite being banned in the United States, most problems have arisen due to the use of PFOA and PFOS, as these compounds have a wide range of applications due to their unique properties (Rehman et al., 2023). Their legacy and persistence in the environment continue to pose significant challenges. Their chemical structure includes a charged functional group carboxylic or sulfonic acids attached to one end. According to Organization for Economic Cooperation and Development (OECD), the term long-chain compound in perfluoroalkyl carboxylic acids (PFCAs) with eight or more carbons, and perfluoroalkyl sulfonic acids (PFSA) with six or more carbons whereas, short-chain related to PFCAs with seven or fewer carbon and PFSA with five or fewer carbons. This is one of the reasons this study focuses primarily on these two compounds, PFOA and PFOS. These long-chain compounds contain eight carbon atoms, which are highly mobile and capable of contaminating various sources such as water, air, and soil through multiple pathways. Despite clear evidence of the significant problems caused by these chemicals, industries that have relied on them for decades have attempted to replace them with short-chain alternatives. These replacements include six-carbon compounds like hexafluoropropylene oxide dimer acid (HFPO-DA), commonly known as GenX, and four-carbon compounds like perfluorobutanesulfonate (PFBS) (Mahoney et al., 2022). However, these alternatives have not significantly mitigated the severity of the environmental and health issues associated with these compounds (Brendel et al., 2018).

PFAS contain a hydrophobic alkyl chain and a hydrophilic functional group such as carboxylate, sulfonate, or phosphonate (Buck et al., 2011). The atomic structure of fluorine has a very important role in developing its unique properties, especially its high electronegativity, high ionization potential, and low polarizability (Leung et al., 2023b). This behavior makes them act as a surfactant and helps reduce the surface tension properties. It is widely used in aqueous film-forming foams, coatings, waterproof clothing, paints, cosmetics, and nonstick cookware. Due to widespread applications, they are even detected in arctic circle samples of ice cores, surface snow, and water samples (Kwok et al., 2013). The contamination caused by these compounds primarily occurs when they are released during manufacturing, production, transportation, product use, and improper disposal into the environment (Qian et al., 2024). This can lead to their presence in public water sources, ultimately entering the bodies of humans and wildlife. So far, we know that PFAS are a large group of human-made chemicals that are extremely persistent in the environment, widespread in air, water, soil, and living organisms, and that some have been linked to adverse health effects in humans and animals. Despite growing research, there are still many unanswered questions about PFAS, including how to detect them more efficiently in air, water, soil, and wildlife; how much people are exposed to; how toxic they are to humans and ecosystems; how to effectively remove them from drinking water; and how to safely manage and dispose of PFAS containing materials. Among all of these problems we are trying to look more into how we can detect PFAS in drinking water using a cost-effective, rapid and more sensitive and selective method. To ensure water quality and safety requires rapid and efficient testing in contaminated environments. The need to test a large number of samples across various times and locations is very challenging for the current laboratory methods, such as high-performance liquid

chromatography coupled with mass spectrometry and gas chromatography (Ateia et al., 2024). This leads to necessity of sensors for detecting PFAS in drinking water.

In sensor science, sensitivity and selectivity are regarded as critical performance metrics that define the overall effectiveness, accuracy, and applicability of a sensor in detecting target analytes (Peveler et al., 2016). To enhance both sensitivity and selectivity, it is essential to understand the mechanistic interactions between analyte and receptor molecule. In this study, we selected five representative PFAS, including PFOA, PFOS, perfluorohexanoic acid (PFHxA), perfluorononanoic acid (PFNA), and PFBS to capture a diverse range of carbon chain lengths and functional groups. These compounds are among the most frequently detected PFAS in environmental and drinking water samples and are listed in the U.S. Environmental Protection Agency's regulatory guidelines and health advisories. By examining their interactions with nitrogen-doped carbon dots, we aim to gain fundamental insight into the sensing mechanism, which can inform the development of highly sensitive and selective PFAS detection methods.

2. LITERATURE REVIEW

2.1 Per- and polyfluoroalkyl substances (PFAS)

Humans always tried to create and modify chemicals to make our life easier. Among all these chemicals, one of the most popular and recently got a lot of attention to PFAS due to its environmental toxicity.

Reliable and accurate methods are required to understand the concentration of PFAS in drinking water. In April 2024, the EPA established the first-ever national drinking water standards for six PFAS compounds to protect public health. The

Maximum Contaminant Level (MCL) for PFOA and PFOS was set at 4 parts per trillion (ppt), reflecting their high toxicity even at low concentrations. For PFNA, PFHxS, hexafluoropropylene oxide dimer acid (HFPO-DA), commonly known as GenX and PFBS, the MCL was set at 10 ppt (EPA, 2024). When it comes to Vermont regulations, which are stricter than EPA's, the cumulative maximum contamination level (MCL) for five PFAS compounds which are PFOA, PFOS, PFNA, PFHxS and perfluoroheptanoic acid (PFHpA) should not exceed 20 ppt (Agency of Natural Resources, 2023). As the maximum contamination level is set in parts per trillion (ppt), any detection method must be sensitive to reliably measure concentrations at or below this threshold. Without such precision, the method would lack the utility necessary to accurately assess contamination levels and inform the public about the presence of these compounds in their environment.

The standard methods approved by the EPA for analyzing PFAS in drinking water include 537.1, 537 and 533. Among them 537.1 method is the most updated and advanced version in which samples are concentrated using a solid phase extraction (SPE) followed by liquid chromatography-tandem mass spectrometry (LC-MS/MS) analysis. It helps to detect around 18 PFAS with a detection limit range of approximately 0.7 - 2 ppt (Dorian Thompson, 2024). In method 533, an additional 11 more PFAS can be detected, which are mostly short-chain substances. In the case of non-potable (groundwater, surface water, and wastewater), there are methods like 8327, which uses multiple reaction monitoring (MRM) LC-MS/MS and helps to determine 24 types of PFAS (Kamrun Nahar, 2023). However, these methods face significant analytical challenges. The challenges include variations in the purity and isomer profiles of commercially available standards, matrix interferences, and their impact on ionization efficiency (Valsecchi et al., 2013). Additionally, these methods are complex,

costly, and time-intensive, often requiring hours to produce results (Thompson et al., 2024). As a result, they are unsuitable for rapid, low-cost, on-site detection, highlighting the need for simpler, more accessible alternatives to address the growing demand for PFAS monitoring. Additionally, these methods require extensive pretreatment, which involves the use of toxic solvents, which contaminate the environment.

To overcome these problems, sensor technology is a promising tool that can use chemical or biological molecular receptors that are designed to respond to specific targets selectively (Ateia et al., 2024). They are vital for evaluating sudden environmental incidents and for efficient routine testing in daily environmental monitoring. By translating binding effects into electrical or optical properties the sensors can detect the different contaminants in different matrixes (Leung et al., 2023a). To develop a sensor for PFAS, researchers have been focusing on electrochemical sensors (Karimian et al., 2018), (Clark & Dick, 2020a), fluorescent-based sensors (Cheng et al., 2019), (Zhang et al., 2022), (Yin et al., 2021) and smartphone-app based monitoring systems (Fang et al., 2018) which are economically feasible and can be used on sites. Effective sensor development must address key factors, including the type of PFAS detected, background signal elimination, wide detection range, and compatibility with various environmental matrices (Nahar et al., 2023).

2.2 Overview of existing sensors for PFAS

Scientists around the globe are racing to develop sensors capable of detecting PFAS at trace levels. Depending on output signals and underlying processes with materials, PFAS sensor are classified into different types in which electrochemical sensors are pioneers, converting chemical interactions into measurable electrical signals. Electrochemical sensors utilize quantifiable electrical signals such as potentiometric (Thompson et al., 2024), voltammetric (Islam & Arrigan, 2022),

amperometric (Clark & Dick, 2020b), impedimetric (Khan et al., 2024), and conductometric methods (Rehman et al., 2023). Since PFAS is not electroactive, this method uses a surface functionalization strategy to enable detection. In this technique redox active mediator is used. When PFAS interact with electrode surface, the mediator's oxidation/ reduction current decreases, this change serves as detection signal (Clark & Dick, 2021). These methods often incorporate materials like molecularly imprinted polymers (MIPs), metal-organic frameworks (MOFs), and ion-selective membranes (ISMs) on electrode surfaces, with metals like gold, platinum, and nickel for enhancing sensitivity (Clark & Dick, 2020b). Gold electrodes modified with MIPs via anodic electropolymerization offer detection limits as low as 0.04 nM for PFOS (Karimian et al., 2018), comparable to chromatographic methods. Their precision rivals the best chromatographic methods, but their complexity poses a hurdle for widespread application.

Meanwhile, optical sensors illuminate the path with their brilliance, and they use different phenomena that can be employed to generate meaningful signals for PFAS detection, such as fluorescence, color variation, and surface plasmon resonance. Due to rapid signal change and adaptability, fluorescence is most commonly used among them (Sendão et al., 2023). They consist of at least one fluorescent compound used as a probe that will emit radiation upon excitation. Through electrostatic and hydrophobic interaction, PFAS interact with their probes to alter the changes in the fluorescent signal, which is proportional to the concentration of PFAS. Based on the signal change, fluorescent sensors can be classified into “turn on” if there is an enhancement in the fluorescent signal and “turn off” if there is a reduction in the signal. They mostly rely on gold nanoparticles (AuNPs), quantum dots (QDs), and fluorescein as probes. Fluorescent indicator displacement assays using guanidinocalix[5] arene and

fluorescein achieve limits of detection (LODs) of 10.9 ppb for PFOA and 11.3 ppb for PFOS (Zhencog et al., 2019). Another approach utilizing aggregation induced emission luminous (AIEgens) demonstrates LODs of 40 ppb for PFAS containing samples (Fang et al., 2019). While effective, these methods are solvent dependent and sensitive to droplet size, complicating field application. In the realm of nanotechnology, nanoparticles emerge as tiny yet mighty heroes. With unique optical and electrical properties, materials like AuNPs push the boundaries of PFAS detection. Nanoparticles are widely used due to their high surface area, quantum size effects, and exceptional sensitivity to trace analytes. AuNPs functionalized with thiol-terminated compounds exhibit colorimetric changes based on PFAS concentration, enabling detection limits of 10 ppb for long-chain PFAS. However, short-chain PFAS detection remains challenging due to lower hydrophobicity (Takayose, 2012; Niu et al., 2014).

Fluorescence spectrometry has been widely used because it is simple, rapid, and sensitive properties attract increasing attention. Nanoparticles, such as quantum dots (QDs) take the center stage as selective fluorescent probes, promising efficient and economical PFAS monitoring which are tiny particles engineered to glow under specific conditions. Cadmium sulfide quantum dot, which is stabilized 3-mercaptopropanoic acid, is a promising tool for detecting PFOS. In the presence of PFOS, quantum dots aggregate due to F-F interaction resulting in a decrease in the photoluminescence intensity which is proportional to the concentration of PFOS with a limit of detection (LOD) 124.2 ppb and a broad sensing range from 207.03 ppb to 16.56 ppm (Sendão et al., 2023). However, despite their sensitivity to PFAS, these quantum dots have certain drawbacks, including toxicity due to the incorporation of heavy metals, reduced dispersion in water, and smaller stokes shifts (Sendão et al., 2023).

Carbon dots (CDs) have emerged as selective fluorescent probes for PFAS detection, offering a promising alternative for efficient and economical monitoring. Because one of the fundamental properties exhibited by carbon dots is their fluorescence emission. Carbon quantum dots are small nanoparticles found to exhibit photoluminescent properties when first discovered accidentally by (Xu et al., 2004). The alteration in fluorescence behaviour of carbon dots can be achieved by surface functionalization and heteroatom doping. The doping of carbon dots using heteroatoms such as nitrogen, phosphorous, sulphur results in the increase of quantum yield, thus enriching the optical properties of carbon dots. The doping improves their sensing efficiency by altering their electronic structure, introducing new energy levels, and creating more active sites on the surface. (Jiao et al., 2018) fabricated a chitosan-based molecularly imprinted polymer (MIP) doped with fluorescent carbon quantum dots (CQDs) for selective PFOS recognition. The CQDs (Ex/Em 350/460 nm) showed PFOS enhanced fluorescence that was stronger in the MIP than in a non-imprinted control (imprinting factor = 2.75), with good specificity over related PFAS and surfactants. The sensor gave a linear response for 20–200 pg/L and quantified PFOS in spiked serum and urine with limit of detection of 66 and 85 pg/L, recoveries of 81–98%, and relative standard error of 1.8–8.2%. Compared with LC-MS/MS, the assay is flexible, convenient, and suitable for on-site screening.

Among these, nitrogen-doped carbon dots (N-CDs) are attaining remarkable attention as they display excellent optical and chemical properties. Nitrogen is the seventh element on the periodic table with five coordinating electrons and an atomic size similar to carbon, such makes nitrogen as an ideal dopant. Incorporation of nitrogen atom into the sp^2 hybridized carbon framework leads to more surface defects on carbon dots and allows tuning of bandgap energy which results in the magnification of

fluorescence intensity and boosting of the quantum yields in carbon dots. The higher nitrogen content tends to increase surface passivation in carbon dots resulting in the amplification of the fluorescence intensity of N-CDs. Compared to other fluorescent dyes and quantum dots, carbon dots are less expensive, less toxic, have high resistance to photobleaching, have wide excitation spectra, are water-soluble, have robust chemical inertness, and have good biocompatibility (Lin et al., 2019). A study by (Cheng et al., 2019) has been proposed for the highly selective fluorescent visual detection of PFOS in aqueous solution based on carbon dots and berberine chloride hydrate (BH). The addition of PFOS restores the fluorescence, likely due to the electrostatic interactions between the positively charged BH and PFOS. This change in fluorescence can be measured quantitatively. When tested in spiked water samples, the carbon dot-BH complex showed promising results for PFOS detection, achieving a limit of detection of 10.8 ppb. This method's key benefit is its ability to differentiate between PFOS and PFOA. The greater hydrophobicity of PFOS and its stronger electrostatic interaction with BH result in a lower fluorescence intensity than PFOA, thereby improving detection specificity. Walekar et.al explored the development of CDs doped with nitrogen and selenium, finding that the fluorescence of these doped CDs is diminished in the presence of PFOA. This quenching is attributed to forming an excited state complex, which facilitates internal electron transfer within the complex. Although the limit of detection for this method is 745.3 ppb, there is potential for further surface modifications of the carbon quantum dots to enhance sensitivity and achieve lower detection limits for other PFAS. Other perfluoro carboxylic acids might also induce fluorescence quenching through similar interactions with the CDs; however, PFNA showed a lesser response compared to PFOA, while PFOS had minimal impact on fluorescence quenching. (Mohammadi et al., 2024a) developed a fluorescence sensor

using fluorine and nitrogen-doped carbon dots (F, N-CDs) for sensitive PFOA detection in drinking water, optimized by tuning the PEI: TFTA precursor ratio (best QY 10.6% at 1:3). The F, N-CDs showed blue emission (Ex/Em 350/470 nm), strong selectivity, and a linear response over 10–1660 ppt. The method achieved a limit of detection of 3 ppt and accurately quantified PFOA in groundwater. (Mohammadi et al., 2025) has developed sodium alginate hydrogel sensor functionalized with nitrogen and fluorine-doped carbon dots (SA–N, F-CDs) to detect PFOA in water. The optimized composite emitted at 480 nm and achieved an ultra-low detection limit of 0.001 ppt, with a linear fluorescence response from 1 to 66 ppq. The platform showed high selectivity for PFOA over other PFAS with minimal interference. Spiked tap-water tests yielded 94–106.6% recoveries, indicating strong suitability for real-world monitoring.

2.3 Current limitations in PFAS sensor technology that hinder compliance with EPA standards and practical field use

Detecting PFAS in water remains challenging due to their lack of chromophore or electroactive groups, making them optically and electrochemically inactive and unsuitable for direct quantification using conventional UV-vis spectroscopy or electrochemical methods (Rehman et al., 2023). To overcome this, sensor materials must be functionalized with selective receptor molecules capable of binding specifically to PFAS. However, the absence of such receptor molecules in current studies has resulted in detection limits far above the EPA’s stringent regulation of 4 ppt, hindering commercial viability. While sensors for emerging contaminants like PFAS have been extensively researched, most remain confined to proof-of-concept studies with limited practical field use, unlike well-established sensors for basic parameters like pH and turbidity (Ateia et al., 2024). Despite their potential, emerging contaminant sensors face several challenges in real-world development. A major limitation is the need for sample pretreatment, which can be time-consuming and resource intensive.

Electrochemical sensors, however, offer advantages such as miniaturization for in situ applications and reduced sensitivity to interference from light-absorbing compounds and turbidity. On the contrary, optical sensors rely on the interaction between light and target analytes to generate measurable signals. These sensors can reveal electronic or vibrational structures of contaminants and detect changes in light excitation or refractive index upon analyte binding, making them promising tools for PFAS detection in complex environmental matrices. Both electrochemical and optical sensing modalities can be integrated into portable platforms including lateral flow devices, miniaturized multiplexed probes, and microfluidic systems.

Nitrogen-doped carbon quantum dots (N-CDs), known for their enhanced optical properties, offer a promising platform for PFAS detection, but their full potential remains untapped due to insufficient understanding of the molecular interactions between PFAS and N-CD materials. By focusing on these mechanistic interactions, particularly at the nanoscale, this research aims to enhance understanding of sensor sensitivity and selectivity, bridging the gap between laboratory innovation and practical implementation while moving closer to the EPA’s regulatory standards.

2.4 Summary of optical-based sensors

Table 2.1. Presents current state of optical-based sensors developed for detecting targeted PFAS.

PFAS	Detection techniques	Detection mechanism	Limit of detection	Concentration range	Reference
PFOA	Colorimetry	Thiol-terminated polystyrene modified gold nanoparticles (PS-SH-AuNPs)	100 ppm	10 – 1000 ppm	(Takayose et al., 2012)

PFBS, PFHxS, PFHpA, PFOA, PFNA, PFTTrDA, PFTeDA, PFHxDA PFOS, PFODA	Colorimetry	Polyethylene glycol and thiols modified gold nanoparticles (Au-PEG-F-NPs)	10 ppb	1 ppb – 1 ppm	(Niu et al., 2014)
PFOS	Colorimetry	Methylene green	10 ppm	0 – 500 ppm	(Menger et al., 2022)
PFOA	Absorbance/ Colorimetry	Fluorinated porphyrin	3 ppm	3 – 30 ppm	(Taylor et al., 2021)
PFOA	Fluorescence	Cadmium sulphide quantum dots	124 ppm	200 ppb – 16 ppm	(Liu, Huang, Wang, Zheng, & Zhu, 2015)
PFOS, PFOA	Fluorescence	Guanidinocalix [5] arene	11 ppb	0 – 300 ppb	(Zheng et al., 2019)
PFOA	Luminescence	Metal-organic framework	19 ppb	0 – 80 ppm	(Yin et al., 2021)
PFOS, PFNA, PFDA,	Optical	Magnetite nanoparticles (MNPs)	10 – 1000 ppb	0.075 – 0.14 ng/L	(Fang et al., 2018)

Table 2.1 presents the status of optical based detection techniques, sensing probes, and the limits of detection for various types of PFAS. Despite the development of various optical sensing methods, significant knowledge gaps remain in understanding the physicochemical interactions between nanoprobe and target PFAS. This understanding is essential for engineering optical probes such as N-CDs with enhanced sensitivity and selectivity.

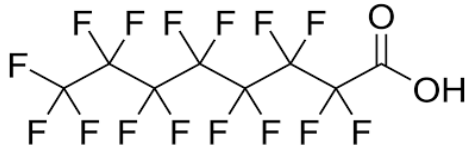
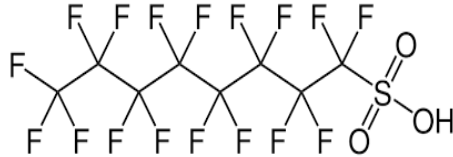
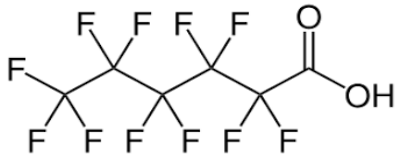
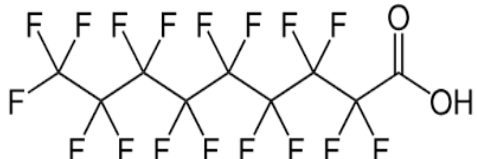

Therefore, in this study, our emphasis is on elucidating the interaction mechanisms between N-CDs and the five PFAS. This investigation involves a comprehensive analysis of changes in key physicochemical properties, including particle hydrodynamic size, zeta potential, absorbance, and fluorescence behavior. By examining alterations in particle size and surface charge upon interaction with PFAS, we seek to understand the nature of binding and aggregation phenomena. Additionally, shifts in optical properties such as absorbance and fluorescence intensities offer critical insights into the electronic and structural modifications of N-CDs in response to varying PFAS concentrations. These findings serve as a foundational step toward the development of a sensitive and selective PFAS sensing platform.

3. OVERALL GOAL AND OBJECTIVE

3.1 Overall Goal

The overall goal is to develop a low-cost, accessible fluorescent sensor using nitrogen-doped carbon quantum dots (N-CDs) to detect five regulated PFAS in drinking water. These five PFAS are selected for this study, and their chemical structure are presented in Table 3.1.

Table 3.1. List of five PFAS regulated by the EPA used in the sensing mechanism study.

Name of the compound	Functional group	Carbon chain length	Structure
Perfluorooctanoic acid (PFOA)	Carboxylic	C8	
Perfluorooctane sulfonic acid (PFOS)	Sulfonic	C8	
Perfluorohexanoic acid (PFHxA)	Carboxylic	C6	
Perfluorononanoic acid (PFNA)	Carboxylic	C9	
Nonafluorobutane-1-sulfonic acid (PFBS)	Sulfonic	C4	

3.2 Objective

The specific objective of the study is to evaluate the effectiveness of nitrogen-doped carbon dots (N-CDs) as fluorescent probes for detecting PFAS in water. This study will focus on elucidating the physicochemical interaction mechanisms between N-CDs and both individual and mixed PFAS (five selected types) in ultrapure water and drinking water matrices. Key parameters to be investigated include changes in particle size, zeta

potential, absorbance, and fluorescence of N-CDs in response to PFAS chain length, functional groups, and background ion concentrations.

4. MATERIALS AND METHODS

4.1 Materials

Nitrogen-doped carbon quantum dots (N-CDs) were obtained from Sabanci University Nanotechnology Research and Application Center (SUNUM), Istanbul, Turkey. The stock solution had a concentration of 2 mg/mL, with a quantum yield of 32%, and was supplied as an aqueous dispersion. The N-CDs exhibited strong green fluorescence with an emission maximum at 490 nm upon excitation at 365 nm. Perfluorooctanoic acid (PFOA, 96% purity), including perfluorohexanoic acid (PFHxA, 98% purity), perfluorononanoic acid (PFNA, 97% purity), and nonafluorobutane-1-sulfonic acid (PFBS, 97% purity), were purchased from Sigma-Aldrich, while perfluorooctanesulfonic acid (PFOS, 97% purity) was obtained from Fisher Scientific. The solution of metal ions used for the sensing application experiments were prepared using chloride salts of (Na^+ , NH_4^+ , K^+ , Ca^{2+} , Mg^{2+} , Cd^{2+} , Li^+ , Ni^{2+} , Zn^{2+} , Ba^{2+} , Pb^{2+}), nitrate salts of (Cu^{2+}) and sodium salts of (Cl^- , NO_3^- , HCO_3^- , CH_3COO^- , SO_4^{2-} , F^- and Br^-). These chemicals were purchased from Sigma-Aldrich and were used as received. Ultrapure deionized water (resistivity: 18.2 $\text{M}\Omega\cdot\text{cm}$ at 25 °C, total organic carbon (TOC: 2 ppb) was produced using a Milli-Q® Q-POD® water purification system (Millipore, USA) was used for all the experiments.

4.2 Material Characterization

To investigate and understand physicochemical properties of N-CDs microscopic, spectrometric techniques and elemental analysis techniques are used. The dry size was measured using transmission electron microscopy (TEM, JEOL JEM-

1400, JEOL Ltd., Japan) at an acceleration voltage of 80 kV. TEM samples were prepared by diluting the quantum dot suspension to 0.1 mg ml^{-1} and depositing a drop onto a 100-mesh nickel grid backed by a carbon support film (LADD Research Industries, USA). The hydrodynamic diameter was measured using nanoparticle tracking analyzer (NTA), ZetaviewTwin PMX-110, Particle Metrix GmbH, Germany) and dynamic light scattering (DLS, Zetasizer NanoZSP, Malvern Panalytical Inc., UK) (Fig. 4.1a and b). Additionally, zeta potential measurements and polydispersity index (PDI) were also conducted using DLS system using electrophoretic light scattering mode.

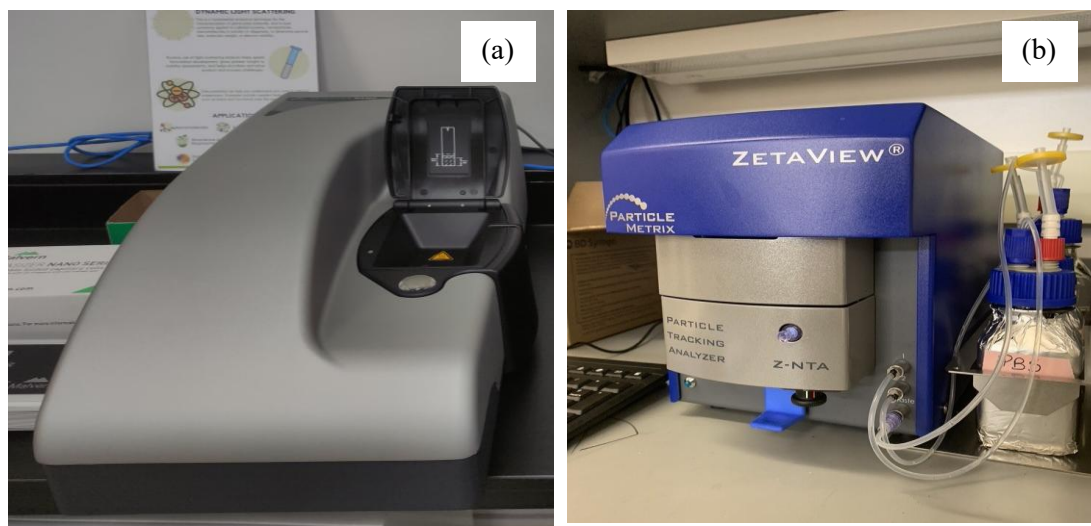


Figure 4.1. (a) Dynamic light scattering (DLS) (b) Nanoparticle track analyzer (NTA)

For NTA and DLS the samples were vortexed for 30 seconds and bath sonicated for 15 min to achieve homogenous dispersion before analysis. In NTA, sample was introduced into the flow chamber at a concentration of 0.1 mg ml^{-1} at room temperature using a disposable syringe. For DLS 1000 microliters (μL) of 0.1 mg ml^{-1} concentration of sample was added in to DTS1070 folded capillary cell for analysis. To account for the repeatability of our study, NTA and DLS was conducted in triplicates. To obtain maximum fluorescence intensity and absorbance of the sample was diluted to $20\times$

factor from the stock solution before conducting the experiments. The absorbance spectra were recorded on a UV-vis spectrophotometer (Cary 7000 series 00instrument version 3.07 Agilent UV-vis-NIR Spectrophotometer, USA). The fluorescence emission spectra were recorded with a slit width of 5 nm for both excitation and emission using (MY2227CG02 model Agilent Cary Eclipse fluorescence spectrophotometer, USA).

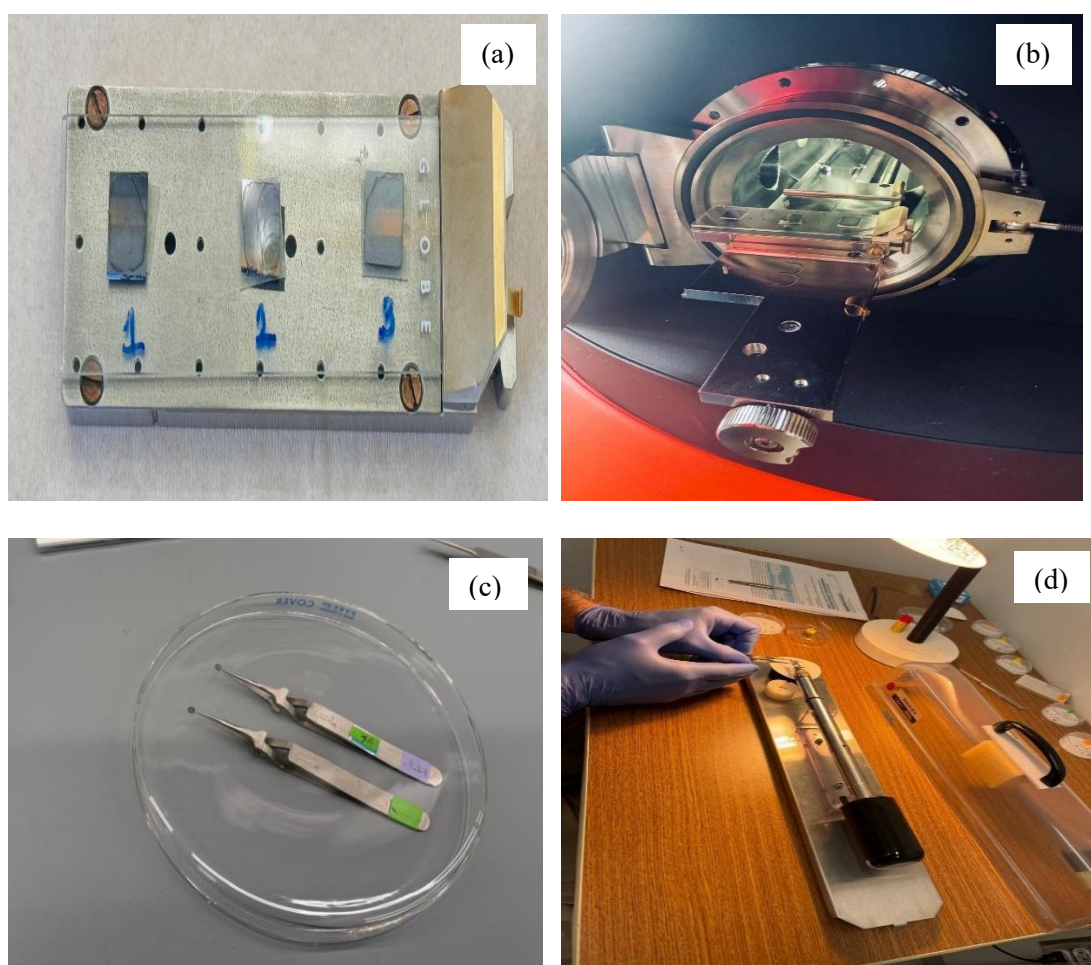


Figure 4.2. (a) Prepared N-CDs and PFAS-interacted samples for XPS analysis; (b) Sample loading onto the XPS holder; (c) Drop-casting of samples on TEM grid; and (d) TEM grid loaded for imaging.

The elemental composition and bond information of the quantum dot surface were investigated by X-ray photoelectron spectroscopy (XPS, The Kratos Axis Supra XPS, UK). XPS samples were prepared by diluting the quantum dot suspension to 0.1 mg ml

⁻¹ deposited on a silicon wafer drop by drop about 1 cm square and 10 nm thickness and dried overnight using a vacuum desiccator (Fig. 4.2).

All spectra were acquired using a Kratos Axis Ultra spectrometer equipped with a monochromatic Al K α X-ray source ($h\nu = 1486.6$ eV). Wide scans were collected at a pass energy of 160 eV, while high-resolution elemental scans were conducted at a pass energy of 40 eV to resolve individual chemical states. The instrument was operated using ESCApe software (Kratos Analytical Ltd.). All measurements were carried out under ultra-high vacuum conditions, with the chamber pressure maintained in the range of approximately 10^{-7} to 10^{-8} Torr during data acquisition.

4.3 Effect of pH on N-CDs fluorescence

To investigate the pH-dependent fluorescence behavior of N-CDs, aqueous 100 ppm N-CDs solutions were prepared and adjusted to pH values ranging from 3 to 8. pH modification was carried out by the incremental addition of 1.0 M hydrochloric acid (HCl) or 1.0 M sodium hydroxide (NaOH) under continuous stirring. The final pH of each solution was measured and verified using a calibrated pH meter. Fluorescence emission spectra of the pH-adjusted N-CDs solutions were recorded using an Agilent Cary Eclipse Fluorescence Spectrophotometer. The excitation wavelength was set at 365 nm, and emission was monitored over a range of 400–700 nm to capture the full emission profile of the N-CDs. All measurements were conducted at room temperature (approximately 25 °C) in quartz cuvettes with a path length of 1 cm. Care was taken to minimize light exposure and avoid photobleaching during the analysis.

4.4 N-CDs properties with PFOA at pH 4.0

Initial experiments were conducted to assess changes in the size, surface charge, absorbance, and fluorescence properties of N-CDs upon exposure to 5 mg/L PFOA.

PFOA was selected as the target PFAS for initial experiments due to its environmental relevance. Two experimental conditions were considered: in the first case, the prepared sample was incubated at room temperature for 10 minutes at pH 6.9; in the second case, the sample was incubated for 72 hours at pH 4. The response of hydrodynamic size, zeta potential, absorbance and fluorescence of N-CDs was recorded for each sample.

4.5 Sensitivity tests with five PFAS

Figure 4.3 shows the schematic of the experimental procedure employed for analyzing the interactions between the N-CDs and PFAS. The detection of five PFAS was performed in aqueous solution at room temperature.

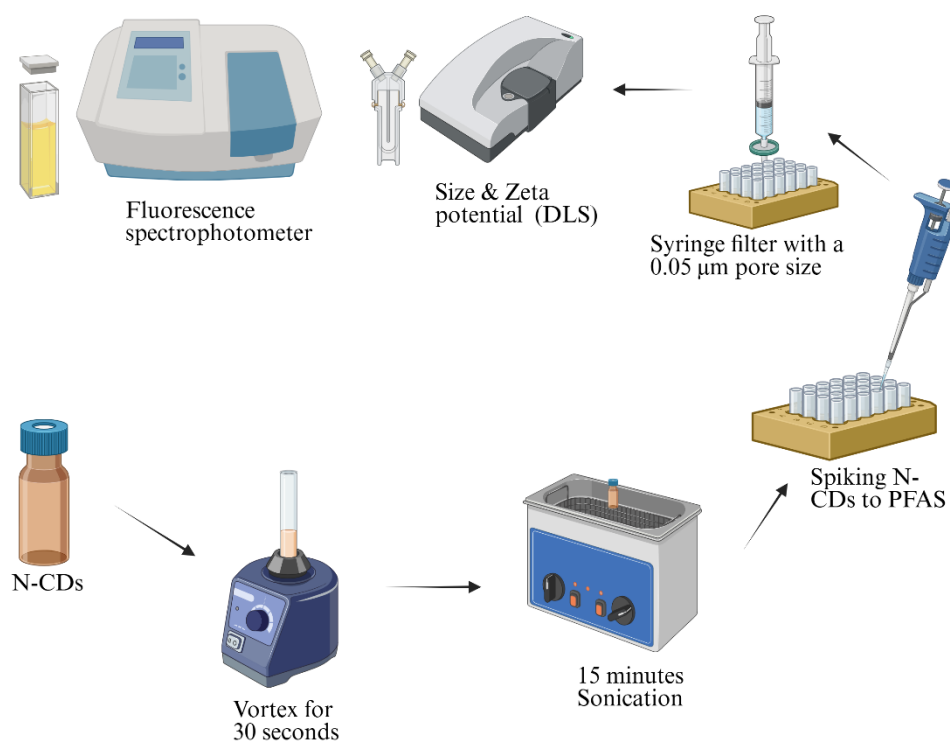


Figure 4.3. Schematic representation of the experimental procedure for analyzing the interaction between nitrogen-doped carbon dots (N-CDs) and PFAS.

In a typical detection procedure, the stock solutions for five PFAS (100 ppm) was first dissolved in ultrapure water. A total volume of 4 mL was prepared for each sample,

containing varying PFAS concentrations (1, 2.5, 5, and 7.5 ppm) while maintaining a fixed concentration of N-CDs (0.1 mg/mL). pH modification was carried out by the incremental addition of 1.0 M hydrochloric acid (HCl) or 1.0 M sodium hydroxide (NaOH) under continuous stirring. After sample preparation the samples were incubated in the room temperature for 10 minutes. The solution was transferred into 4 ml cuvettes for measuring absorbance and fluorescence spectra recording at an excitation wavelength of 365 nm. All the experiments were performed in duplicate and average was obtained. Similarly, to understand the change in hydrodynamic size and zeta potential is measured using DLS.

4.6 Background ions effect

The selectivity of N-CDs as fluorescent probe was evaluated by measuring the fluorescent responses of other ions often present at surface water, such as common metallic ions or cations (Na^+ , NH_4^+ , K^+ , Ca^{2+} , Mg^{2+} , Pb^{2+} , Cd^{2+} , Li^+ , Ni^{2+} , Zn^{2+} , Ba^{2+}), anions (Cl^- , SO_4^{2-} , NO_3^- , HCO_3^- , CH_3COO^- , HPO_4^- , F^- , Br^-) structural analogues of PFOA (PFOS, PFHxA, PFNA and PFBS), mixture of ions (both cations and anions), and mixture of ions and PFAS. The concentrations of PFOA and other ions were all kept to 7.5 ppm. For interference study, same concentration of (Na^+ , NH_4^+ , K^+ , Ca^{2+} , Mg^{2+} , Pb^{2+} , Cd^{2+} , Li^+ , Ni^{2+} , Zn^{2+} , Ba^{2+}), anions (Cl^- , SO_4^{2-} , NO_3^- , HCO_3^- , CH_3COO^- , HPO_4^- , F^- , and Br^-) were all added with N-CDs solution. For measurement, 7.5 ppm PFOA was added to the probe solution containing mixed interfering ions and fluorescence spectra were recorded. The fluorescence intensities of ion blank (N-CDs + PFOA, denoted as F_0) and ion-containing samples (N-CDs + PFOA + ion, denoted as F) were compared, and the fluorescence change ($\Delta F = F - F_0$) was calculated.

4.7. Statistical Analysis

All experiments were conducted in triplicate to ensure reproducibility, and the average values were used for analysis. Statistical analysis was performed to evaluate the significance of changes observed in hydrodynamic size, zeta potential, absorbance, and fluorescence intensity of N-CDs upon interaction with different PFAS. Standard deviation was calculated for each measurement to assess variability and reliability. To evaluate the statistical significance of changes in hydrodynamic size and surface charge of N-CDs upon interaction with PFOA, independent two-sample t-tests were conducted across three experimental conditions: (i) N-CDs alone, (ii) N-CDs with 5 ppm PFOA, and (iii) N-CDs with 5 ppm PFOA after 72 hours incubation at pH 4. One-way analysis of variance (ANOVA) was applied to determine whether the changes across different PFAS compound.

5. RESULTS AND DISCUSSION

5.1 Characterisation of N-CDs in ultrapure water

5.1.1 Size and Zeta potential

Particle size has direct influence on material properties. TEM images provide the dry particle size and particle visualization that allow for the exact size measurement of individual quantum dots. TEM images show the core size and the diameters of N-CDs ranging from 20 to 34.2 nm, with an average size of 25.6 ± 0.44 nm (Fig 5.1a-d).

When N-CDs are dispersed in an aqueous medium, their surface functional groups interact with surrounding molecules, such as water, ions, or other solutes present in the solution, through the formation of an electrical double layer. These interactions lead to increasing the N-CDs apparent size compared to their core size, which is referred as hydrodynamic size.

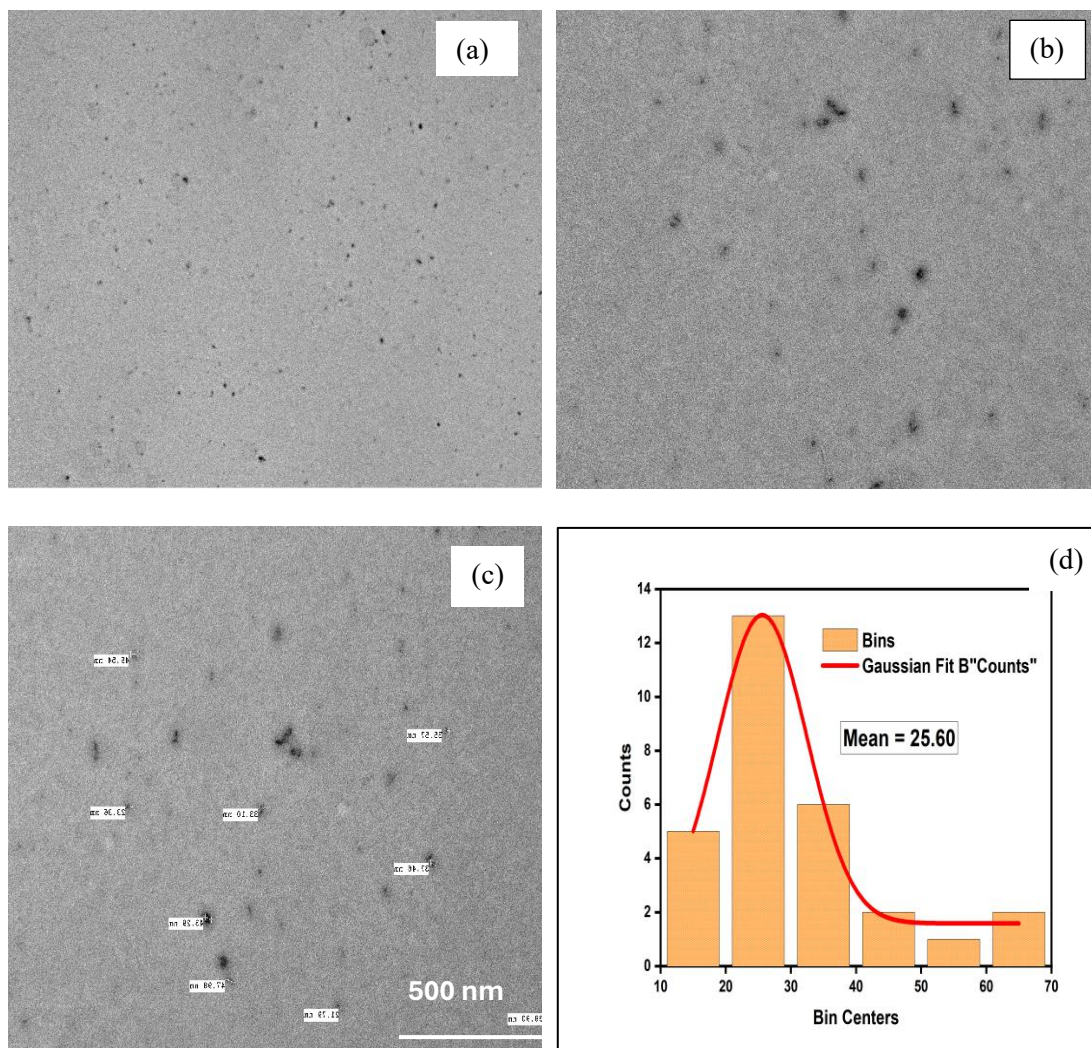


Figure 5.1. TEM images of N-CDs (a) (magnification = 3000 \times) (b) (magnification = 12000 \times) (c) (magnification = 12000 \times) (d) Histogram of particle size distribution for nitrogen-doped carbon dots (N-CDs) obtained from TEM analysis. All images were taken at accelerating voltage of 80 kV. The orange bars represent the frequency of particle sizes binned across measured diameters, while the red curve indicates the Gaussian fit applied to the data. The average particle size of the N-CDs was calculated to be 25.6 ± 0.44 nm suggesting a narrow and symmetric size distribution.

In this study, both DLS and NTA were used to measure the hydrodynamic size of N-CDs. NTA tracks the Brownian motion of individual particles using laser illumination and a high-resolution camera, enabling particle-by-particle analysis (Noel et al., 2025). This method provides a detailed size distribution and facilitates the distinction between individual N-CDs and potential aggregates. DLS, in contrast, measures fluctuations in

the intensity of scattered light caused by brownian motion of particles, providing an intensity-weighted average particle size. The average hydrodynamic size measured through DLS is 98.32 ± 2.46 nm and NTA is 99.5 ± 27.1 nm. Both techniques yield a similar average size which validate the reliability of the particle size measurements in aqueous medium.

Poly dispersity index (PDI) represents the particle size distribution of N-CDs in the aqueous phase. Numerically, the PDI ranges from 0.0, which indicates a perfectly uniform sample with respect to particle size, to 1.0, which reflects a highly polydisperse system containing multiple particle size populations. In practice, values of 0.2 or lower are generally considered acceptable for polymer based nanoparticle materials (Danaei et al., 2018). The measured PDI for the N-CDs sample is 0.240, suggesting a relatively narrow distribution and indicating that the particles are uniformly dispersed in the medium.

Table 5.1. Stability behaviour of colloidal suspension to zeta potential values.

Zeta Potential range (mV)	Stability Level in Water
0 to ± 10	Highly unstable, rapid coagulation/flocculation
± 10 to ± 20	Limited stability
± 20 to ± 30	Moderately stable
$> \pm 30$	Highly stable

In addition to size measurements, the zeta potential measurements were carried out. These measurements reflect the surface charge of nanoparticles, which is a key indicator of colloidal stability (Table 5.1). A high absolute zeta potential suggests strong

electrostatic repulsion between particles, minimizing aggregation. The N-CDs exhibited a zeta potential of -29.63 ± 0.99 mV, indicating good colloidal stability in aqueous suspension under the tested conditions.

5.1.2 Absorbance and fluorescence of N-CDs

Absorbance quantifies the extent of light absorption by a sample. The energy required to promote an electron is determined by the energy difference between ground and excited states, which is a function of the type of molecular orbital involved in the transition (n VS. π) and the presence of electron delocalization or conjugation (Korak & McKay, 2024). The N-CDs shows two absorbance peaks in UV-vis range - one at 272 nm and other at 320 nm corresponding to $\pi - \pi^*$ and $n - \pi^*$ transitions, respectively. The strong absorbance at 272 nm is due to the $\pi - \pi^*$ transition of conjugated C = C units in carbon core. This indicates that the N-CDs possess a well-developed conjugated π -electron system which is essential for efficient delocalization. And at the 320 nm assigned to the $n - \pi^*$ transition of C – N, C – O, C = O functional groups present at the edge of N-CDs, which involve non-bonding electrons (n) and heteroatoms, such as nitrogen (N) and oxygen (O). Hence, UV-vis absorption spectrum confirm that the N-CDs possess both a well-structured carbon core and a variety of O- and N-containing functional groups.

Fluorescence arises when a molecule, after absorbing light and forming a singlet excited state, relaxes non-radiatively to the lowest vibrational level of S_1 and then returns to the ground state S_0 by emitting a photon. The emission wavelength corresponds to the $S_1 \rightarrow S_0$ energy gap and is typically longer than the excitation/absorbance wavelength because energy is lost during vibrational relaxation and solvent reorganization (Stokes shift) (Korak & McKay, 2024). The fluorescence

mechanism of N-CDs is complex and influenced by multiple factors, including molecular/surface states, size effects, and crosslinking-enhanced emission. Initially, emission is driven by molecular states during polymerization. As carbonization progresses, crosslinking-enhanced emission and eventually size and surface state effects dominate, leading to a core-shell structure. The surface state depends on the hybridization between the carbon core and attached chemical groups. In fully carbonized quantum dots, size effects become predominant. Thus, by tuning the carbon core structure and surface functional groups, such as through sp^2/sp^3 ratio adjustments, fluorescence properties can be controlled. The N-CDs shows maximum emission at 490 nm at an excitation wavelength 365 nm with a quantum yield of 32 %. The efficiency of fluorescence process is measured by the quantum yield. It is defined as the ratio of the number of photons emitted per the total number of photons absorbed by the sample (Nawara & Waluk, 2017).

Under ambient light, N-CDs solution exhibits a brown color, while under UV light, it displays a bright green color (Fig. 5.3). The optical stability of the N-CDs at room temperature and under UV-A irradiation was further evaluated to assess their potential in optical sensing. The underlying principle on which spectrofluorimetric method is based on the variations in fluorescence intensity during the physicochemical interaction between fluorescent N-CDs and PFAS.

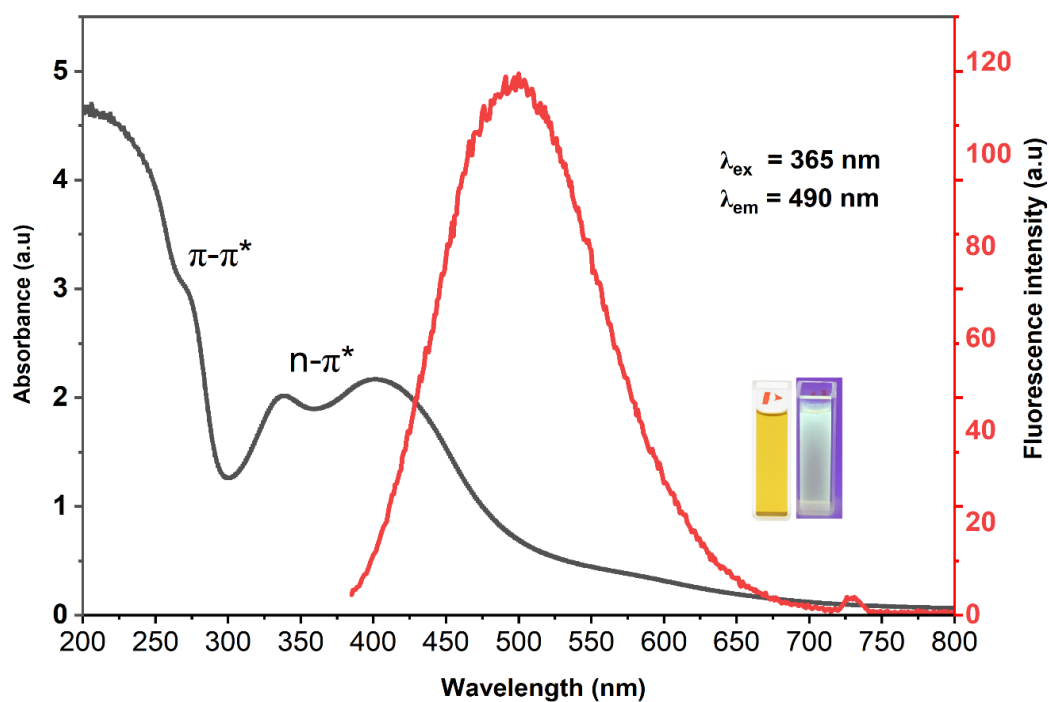


Figure 5.2. Absorbance and fluorescence spectra of N-CDs in ultrapure water at pH 6.9.

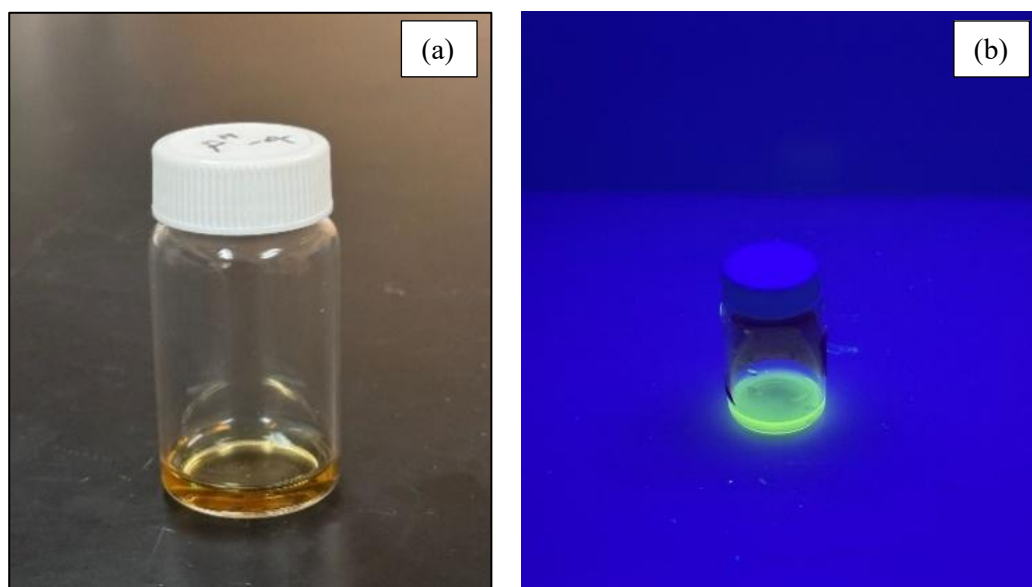


Figure 5.3. The images show N-CDs solution under (a) ambient light and (b) UV-A light.

5.1.3 Stern-Volmer plot

In this study, the Stern-Volmer plot is used to understand how the fluorescence intensity of N-CDs is influenced by the presence PFAS. The Stern-Volmer plot is generated by measuring the fluorescence intensity of the N-CDs at different PFAS concentrations and then plotting the ratio of the initial fluorescence intensity (F_0 , in the absence of PFAS) to the observed intensity (F , in the presence of PFAS) against the different concentration of PFAS.

$$\frac{F_0}{F} = 1 + K_{sv}[Q] \dots\dots\dots 1$$

K_{sv} is the quenching constant and $[Q]$ is the concentration of the quencher (Shaw et al., 2023). This relationship can be used to understand how fluorescence response of N-CDs changes with the concentration of PFAS. Depending on the interaction between N-CDs and PFAS, the fluorescence response may exhibit either a quenching, an enhancement or remain unchanged. In an aqueous system, aggregation, electrostatic and hydrophobic interactions between the fluorescent probe and PFAS molecules can cause measurable variations in fluorescence intensity with changing PFAS concentrations (Mohammadi et al., 2024b). (Zhang et al., 2022) study observed that CdTe quantum dots undergo fluorescence quenching upon interaction with PFOA and PFOS, achieving detection limits of 32.02 pM for PFOA and 43.96 pM for PFOS. The fluorescence quenching mechanism includes dynamic and static quenching. Dynamic quenching is due to the collision between the quencher and fluorescence molecule whereas static quenching resulted from the formation of a non-fluorescence complex molecule does not change in the presence of quencher. Both mechanisms leading to the decrease in both quantum yield and intensity of the fluorescence. They distinguished between static and dynamic quenching by comparing the fluorescence lifetimes of CdTe

quantum dots in the absence and presence of PFAS, where an unchanged lifetime indicated a static quenching mechanism and a Stern-Volmer plot is used to understand how efficiently fluorescence intensity decreased by the addition of PFOA/PFOS. Similarly (Shaw et al., 2023) in this study, Nitrogen and Sulfur co-doped carbon dots (NSCDs) acted as the fluorescent probe, while crotonaldehyde (CT) served as the quencher. The SV plots (F_0/F vs $[Q]$) in both aqueous and ethanol media exhibited a positive deviation from linearity rather than a straight line, reflecting complex quenching behavior. The upward curvature (positive slope) at higher CT concentrations suggested a combination of static and dynamic quenching in aqueous solution, whereas the deviation in ethanol medium was attributed predominantly to static quenching. Stern-Volmer relationship with a positive slope typically indicates quenching. However, if fluorescence enhancement occurs upon the addition of PFAS, it will result in a decrease in the slope according to the Stern–Volmer equation. Unlike the classic case where only either fluorescence quenching or enhancement is observed, the present system displayed a dual behaviour: an initial fluorescence quenching at low PFAS concentrations, followed by fluorescence enhancement at high concentrations. In most reported studies, receptor molecules or amine-functionalized carbon dots are employed to enhance the interaction and sensitivity toward PFAS compounds. However, the N-CDs used in this study contained only 5.1% nitrogen, which may account for the irregular fluorescence trend and the relatively lower sensitivity toward PFAS. By systematically varying PFAS concentrations and examining changes in emission intensity, the Stern-Volmer method provides a quantitative framework to evaluate the sensitivity, selectivity, and detection limit of the N-CDs toward PFOA. Figure 5.4 schematically illustrates the Stern–Volmer fluorescence response for the present

system, where the transition from quenching to enhancement is observed with increasing PFOA concentration.

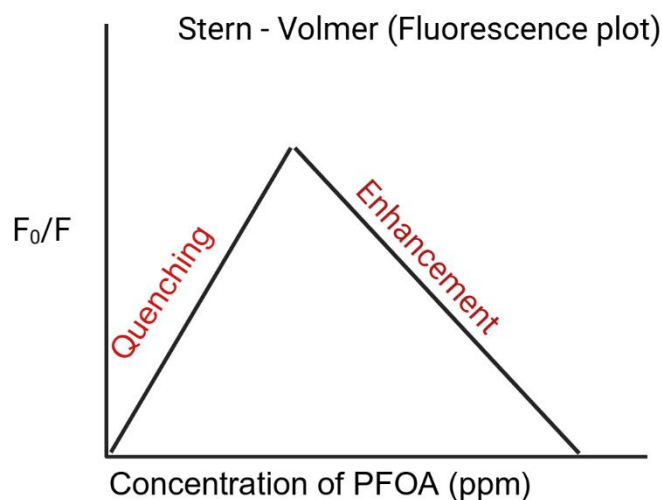


Figure 5.4. Schematic Stern–Volmer plot showing the transition from fluorescence quenching to enhancement with increasing PFOA concentration.

5.1.4 Elemental composition and chemical bonding

The elemental composition and functional groups of N-CDs were analyzed by XPS. In wide scan three main peaks at 285, 400, 531.5 eV were observed and attributed to C 1s, N 1s and O 1s, respectively (Fig 5.5a). The atomic percentage of C, N and O was recorded as 41.6 %, 5.1 % and 33.2 %, respectively (Table 5.2).

The detailed peak fitting of C 1s spectrum indicated mainly four types of carbon bonds which are graphitic or aliphatic C = C/C – C (285.49 eV), nitrous C – N (286.99 eV), oxygenated C = C/O – C = O (288.99 eV), and $\pi - \pi^*$ stack bonding (293.69 eV) (Fig 5.5b-d). Every photoelectric process is not that simple ones which lead to the formation of ions in the ground state. There is a finite probability that the ion will be left in an excited state a few electron volts above the ground state. In this case, the kinetic energy of the emitted photoelectron is reduced, with the difference corresponding to the energy difference between the ground state and the excited state. This results in the formation

of a satellite peak a few electron volts lower in kinetic energy that means higher in binding energy than the main peak. This is called a shake-up process. Because of this, the energy of the ejected electron becomes slightly lower, and this shows up as an extra small peak next to the main peak in the XPS spectrum. The characteristic shake-up line for carbon in aromatic compounds, a shake up process involving the energy of $\pi - \pi^*$ transition which is observed in C1s spectrum of N-CDs. This extra peak is called a shake-up line (Jolm F. Moulder, 1978).

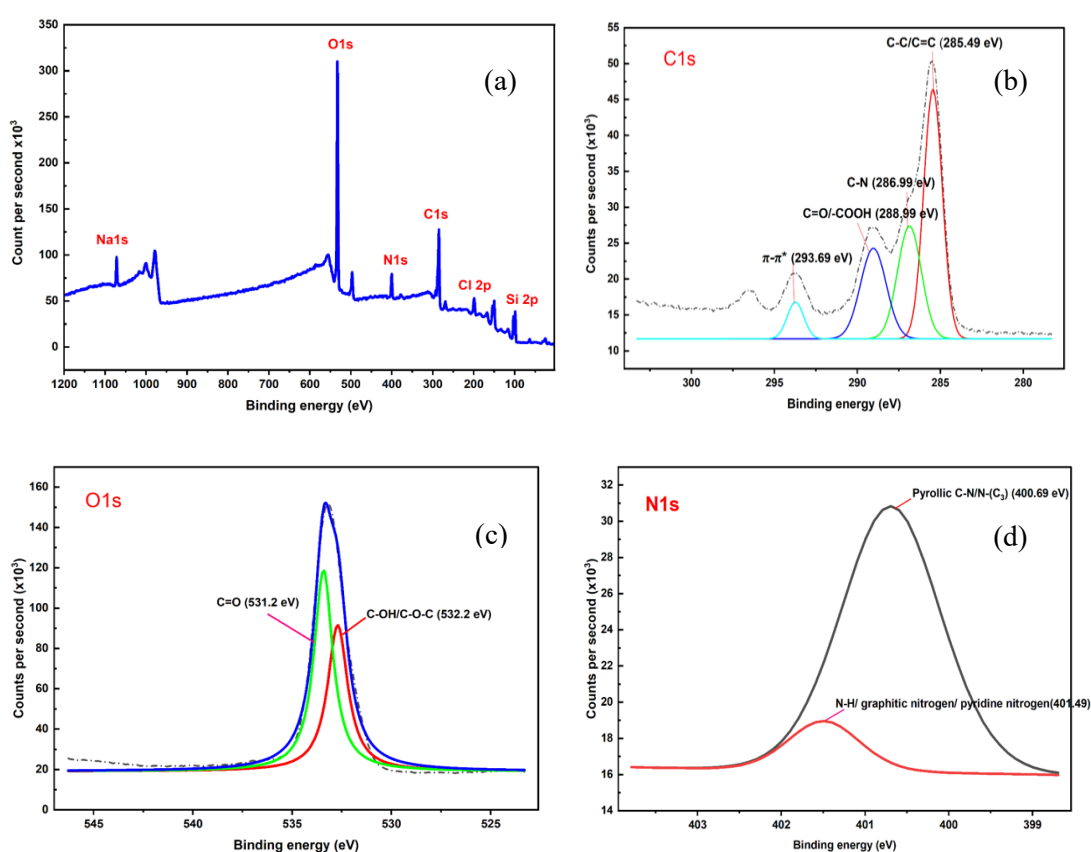


Figure 5.5. (a) Wide scan spectrum of nitrogen-doped carbon dots (N-CDs) showing the presence of Na 1s, O 1s, N 1s, C 1s, Cl 2p, and Si 2p peaks. (b) High resolution C1s spectrum of N-CDs, (c) High resolution O1s spectrum of N-CDs (d) High resolution N1s spectrum of N-CDs.

The appearance of these lines in the C 1s region is a sign that the N-CDs have graphitic or aromatic structures, which are important for their fluorescence and other properties

(Table 5.3). The two N1s peak present testified that Nitrogen existed mostly as N – C₃/pyrrolic-N (400.69 eV), N – H/pyridine like nitrogen /graphitic nitrogen (401.49 eV). The two fitted peaks 531.2 and 532.2 eV corresponding to C = O/–COOH and C – O – C groups, respectively.

Table 5.2. XPS elemental composition and peak parameters of N-CDs

What is this?	Binding energy (eV)	Full width at half maximum (FWHM) (eV)	Relative sensitivity factor (RSF)	Atomic conc. (%)	Error (%)	Mass conc. (%)	Error (%)
Si 2p	99.00	6.59	0.33	15.3	0.31	25.6	0.45
Cl 2p	199.00	4.05	0.89	3.0	0.21	6.3	0.43
C 1s	285.00	3.25	0.28	41.6	0.71	29.7	0.62
N 1s	400.00	2.77	0.48	5.1	0.31	4.3	0.26
O 1s	533.00	2.91	0.78	33.2	0.48	31.6	0.42
Na 1s	1072.0	2.81	1.69	1.8	0.13	2.5	0.18

Table 5.3. Bond information from C1s spectrum.

Binding energy (eV)	Corresponding bond	Interpretation
284.49	C-C/C=C	Graphitic carbon
286.99	C-N	Carbon nitrogen bond from nitrogen doping
288.99	C=O/-COOH	Carboxylic acid (Passivation)
293.69	$\pi-\pi^*$	Conjugated carbon bond in graphite

The presence of pyridine nitrogen, pyrrolic nitrogen, graphitic nitrogen, and amino nitrogen functionalities on the N-CDs surface provided strong evidence for the successful nitrogen doping on the carbon dots. Since it contains nitrogen in special forms such as graphitic nitrogen and pyridine nitrogen, which can help to control how the carbon dots absorb and emit light. The band gap is the energy difference that decides the color of the light the carbon dot can absorb and emit. When there is more graphitic

nitrogen, this energy gap gets smaller, and that changes the color of light the dots give off. So, green emitting N-CDs have a moderate band gap not too big like blue and not too small like red. For green color, the band gap is usually 2.3 to 2.4 eV. Based on the XPS bond information, we confirm that the functional groups present on the surface of quantum dots are $-\text{COOH}$, $-\text{OH}$ and $-\text{NH}_2$ (Fig 5.6).

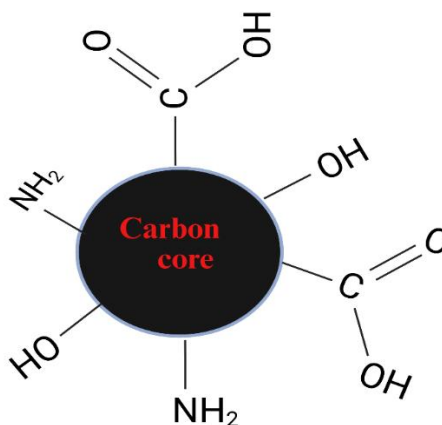


Figure 5.6. Potential surface functional groups of nitrogen-doped carbon dots (N-CDs)

5.1.5 Effect of pH on N-CDs fluorescence

The fluorescence response of N-CDs was evaluated across a pH range of 3.0 to 8.0 to determine the optimal condition for enhanced sensing performance. As N-CDs has various functional groups including carboxyl and amine they are sensitive to changing pH environments (Prado et al., 2023). The results showed that the N-CDs exhibited maximum fluorescence intensity at pH 4 compared to any other tested pH (Fig 5.7), indicating enhanced optical stability and surface activity under mildly acidic conditions. The emission intensity of N-CDs was found to vary significantly with pH, reflecting the strong influence of protonation and deprotonation equilibria of surface functional groups such as hydroxyl, carboxyl and amine groups. Consequently, all

subsequent analyses and sensing experiments were conducted at pH 4 to ensure consistent and optimal performance.

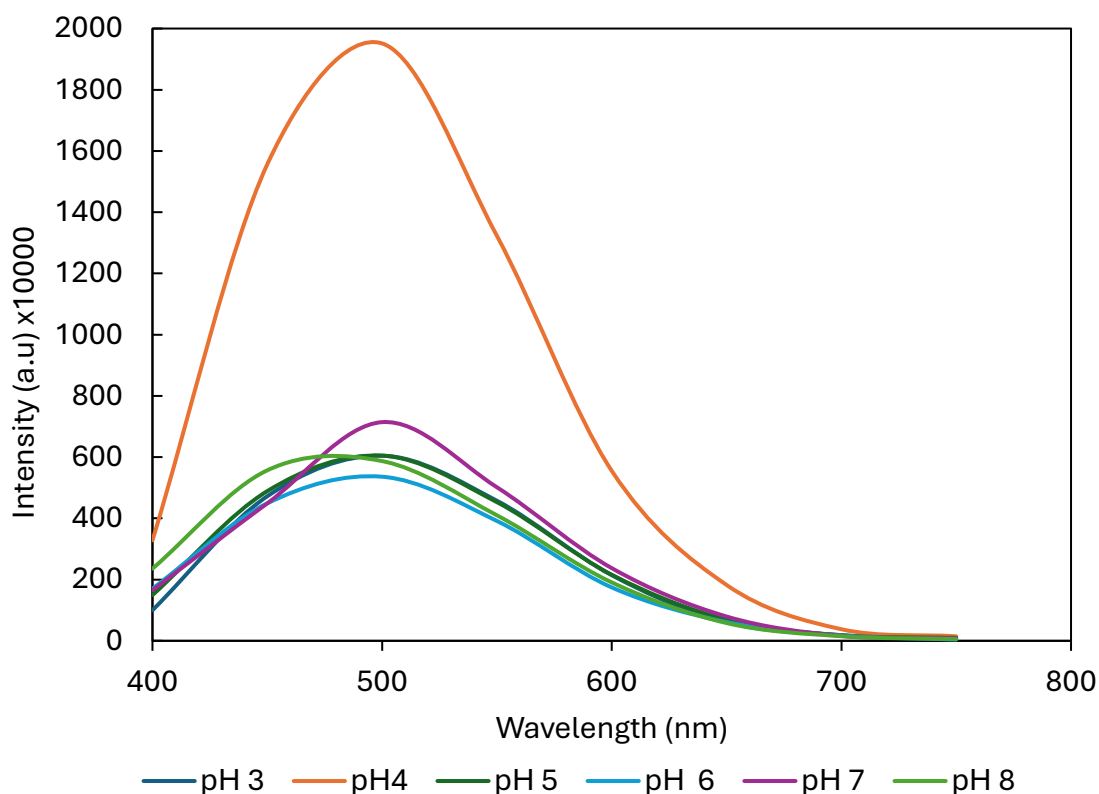


Figure 5.7. Fluorescence emission spectra of nitrogen-doped carbon dots (N-CDs) at different pH values ranging from 3 to 8. The emission wavelength is 490 nm.

5.2 Preliminary study with PFOA

To assess the extent to which PFOA alters the stability of N-CDs, it is important to measure the hydrodynamic size and surface charge (or zeta potential) of the suspended quantum dots in ultrapure water. Figures 5.8 and 5.9 illustrate the change in hydrodynamic size and zeta potential of N-CDs (pH 6.9) before and after exposure to 5 mg/L PFOA under two conditions: 10-minute incubation at pH (6.9) and 72-hour incubation at pH 4. After exposure to PFOA for 10 minutes, N-CDs increased in effective hydrodynamic diameter from 98.32 ± 2.46 nm to 192 ± 3.22 nm and after 72 hours there was a gradual increase to 296 ± 37.99 nm. This increase is most likely a

result of PFOA sorption to N-CDs, resulting a larger effective size; this change in effective size could be either an actual increase in size or an increase in mass that is reported as a change in size. The zeta potential after 10 minutes when PFOA exposed with N-CDs significantly changed to -29.63 ± 0.99 eV to -17.87 ± 4.36 eV and 72 hours significantly changed to -6.33 ± 0.99 eV, further indicating the sorption PFOA molecule with N-CDs. This indicates more extensive interactions due to increased protonation of N-CDs at pH 4 results in additional aggregation.

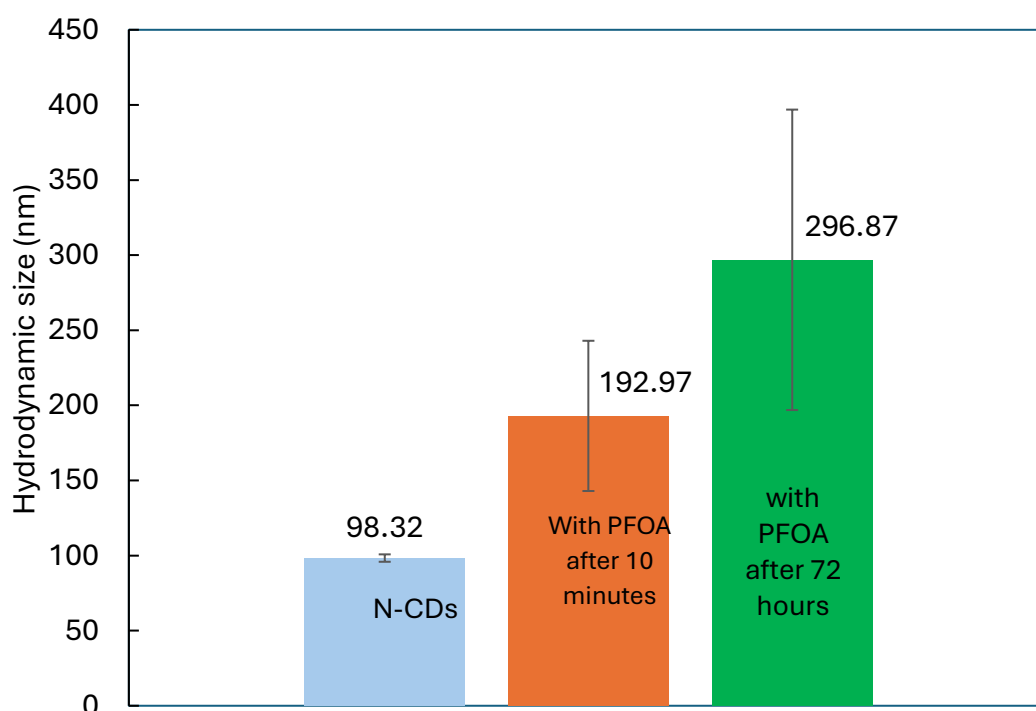


Figure 5.8. Hydrodynamic size of N-CDs with the addition of 5 mg/L PFOA and incubation time (after 10 min and 72 h) with no mixing at ambient temperature. The size 98.32 nm represents the well-vortexed initial condition of the N-CDs in ultrapure water at pH 6.9.

Similar trends are reported in (Lewis et al., 2023) wherein a significant increase in the hydrodynamic size of PEI-functionalized carbon dots (PEI-CDs) upon exposure to PFOA, indicating sorption-driven interaction, was observed. This pattern supports the

hypothesis that PFOA binding induces surface modification or aggregation in N-CDs, which is consistent with our findings. Furthermore, Lewis et al. observed a reduction in zeta potential from +38.6 mV to +26.4 mV, which was attributed to the masking of positive surface charge by negatively charged PFOA. In our test samples, the zeta potential of N-CDs became progressively less negative over time, shifting from -29.63 ± 0.99 mV to -17.87 ± 4.36 mV after 10 minutes, and to -6.33 ± 0.99 mV after 72 hours, further confirming the role of electrostatic interactions and charge neutralization by PFOA. The correlation between size enhancement and surface charge reduction validates our interpretation that PFOA sorption occurs on the surface of N-CDs, most likely through electrostatic interactions between the protonated amine groups on N-CDs and the negatively charged carboxylate group of PFOA at pH 6.9.

We have tested three experimental conditions: (i) N-CDs alone (pH 6.9), (ii) N-CDs with 5 ppm PFOA (pH 6.9), and (iii) N-CDs with 5 ppm PFOA after 72 h incubation at pH 4. The results revealed a significant increase in hydrodynamic size of N-CDs with 5 ppm PFOA after 10 minutes ($p = 0.000005$) compared to N-CDs with no PFOA, indicating rapid binding and aggregation of N-CDs in the presence of PFOA. The size of N-CDs with 5 ppm PFOA after 72 hours further increased significantly compared to the samples after 10 min incubation period ($p = 0.018$), suggesting continued sorption/aggregation or agglomerate structural rearrangement over time under acidic conditions (pH 4). Overall, the size difference between N-CDs with 5 ppm PFOA and N-CDs with 5 ppm PFOA after 72 h was highly significant ($p = 0.0018$), confirming substantial PFAS-induced aggregation.

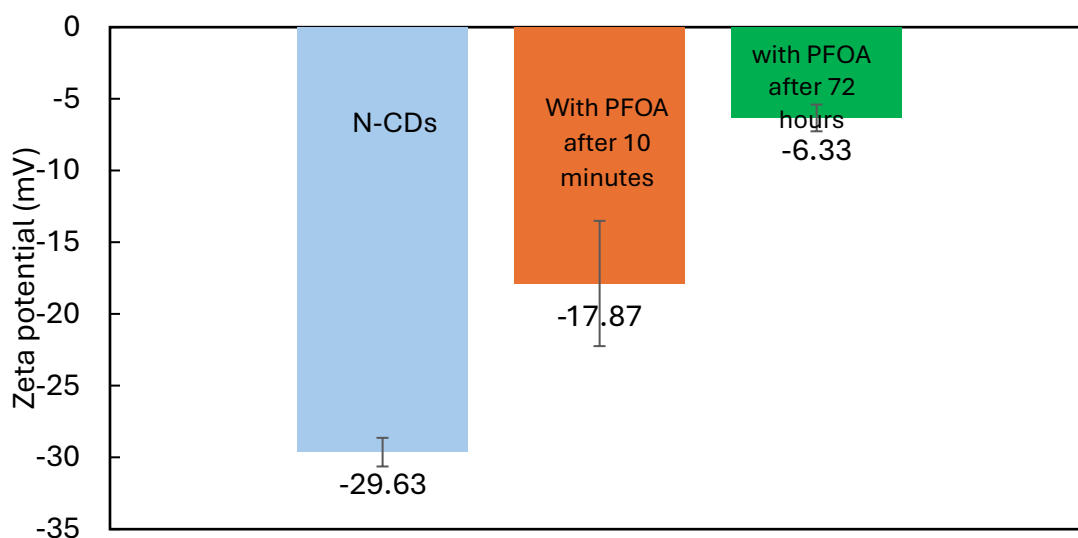


Figure 5.9. Zeta potential of N-CDs with the addition of 5 mg/L PFOA and incubation time (after 10 min and 72 h) with no mixing at ambient temperature. The size 98.32 nm represents the well-vortexed initial condition of the N-CDs in ultrapure water at pH 6.9.

Similarly, the zeta potential also showed significant changes across all comparisons, with $p = 0.0206$ between experimental conditions (i) and (ii), and $p = 0.0217$ between experimental conditions (ii) and (iii), indicating a progressive reduction in surface charge, likely due to PFOA adsorption and N-CDs surface charge neutralization by the carboxylic groups of PFOA. These findings provide strong evidence for concentration and time-dependent interaction of PFOA with N-CDs, validated by statistically significant alterations in both size and zeta potentials.

5.3 Hypothesized interaction mechanism

The potential structure of the N-CDs predominantly contains carboxylic and amine functional groups. The effect of pH on the fluorescence intensity of the N-CDs confirms that pH 4 exhibits the maximum fluorescence intensity. Figure 5.10 illustrates the speciation diagram of a carboxyl-amine functional group, showing the relative fraction of each ionic species across varying pH. Around pH 4, the zwitterionic form where the carboxylic group is deprotonated ($-\text{COO}^-$) and the amine group is protonated ($-\text{NH}_3^+$) is the predominant species.

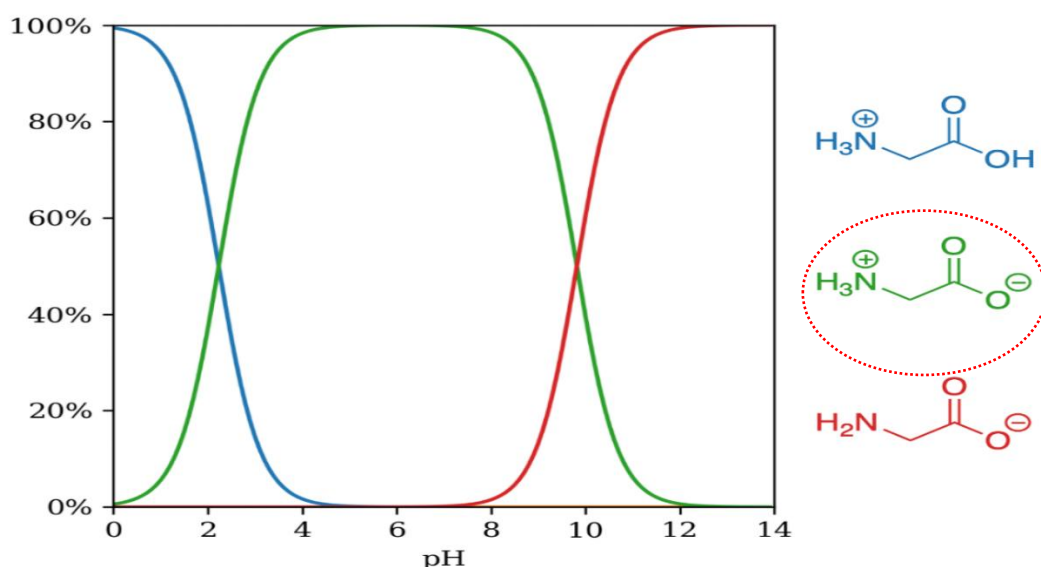


Figure 5.10. Speciation diagram of carboxyl amine.

As shown in Figure 5.10, with increasing pH, the surface functional groups of N-CDs tend to deprotonate, resulting in negatively charged species due to loss of protons from $-\text{COO}^-$ and $-\text{NH}_3^+$ groups. This affects the surface charge and interaction behavior of N-CDs with PFOA in solution. PFOA, on the other hand, readily dissociates in water to form its anionic form, perfluorooctanoate, and a proton (H^+) over a wide range of pH due to their low acid dissociation constant (Fatima et al., 2025). This means that even at pH 4 to neutral conditions, PFOA exists predominantly in its negatively charged anionic form which can interact electrostatically with positive charges on N-CDs.

In addition to hydrodynamic size and zeta potential, the quenching in absorbance and enhancement in the fluorescence spectra further validate that N-CDs can potentially serve as a fluorescent probe for PFOA (Dalapati et al., 2024; Lin et al., 2019; Liu et al., 2015). The absorbance and fluorescence responses obtained for PFOA (Fig 5.12 and 5.13) suggest a likely interaction mechanism between N-CDs and PFOA involves both hydrophobic and electrostatic forces. To advance this study further, we have studied

other PFAS, including PFOS (C8), PFHxA (C6), PFNA (C9), and PFBS (C4), which were selected based on the differences in carbon chain length and functional groups.

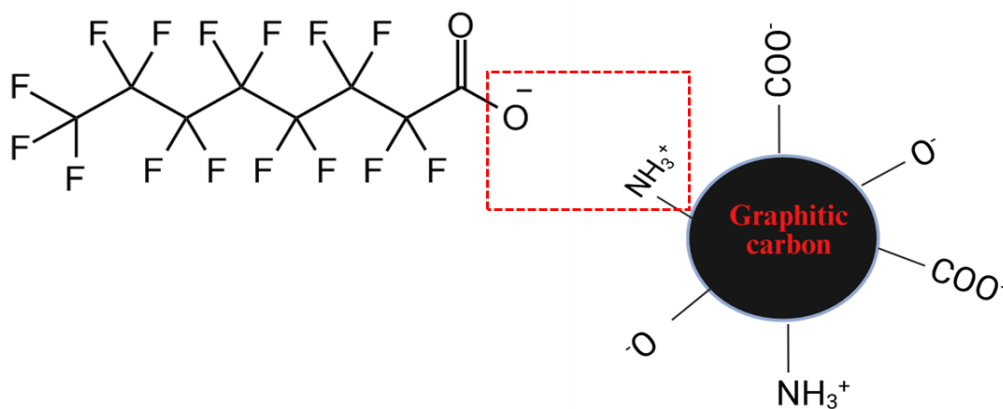


Figure 5.11. Potential electrostatic interaction between PFOA and N-CDs at pH 4.

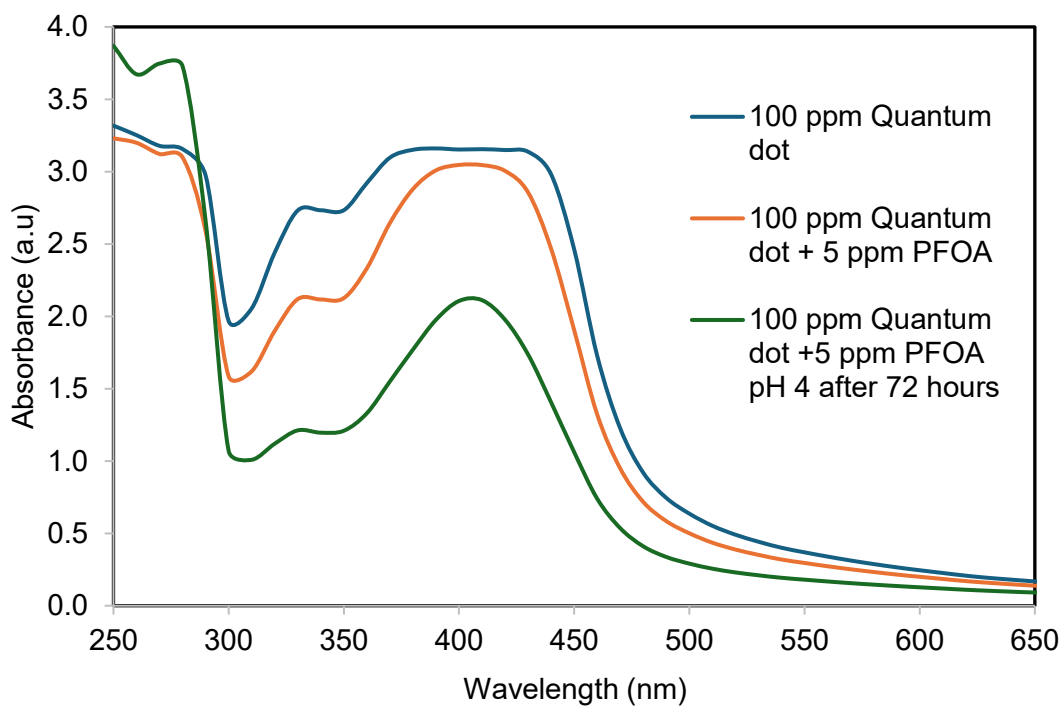


Figure 5.12. Representing the change in absorbance of N-CDs with the addition of 5mg/L PFOA

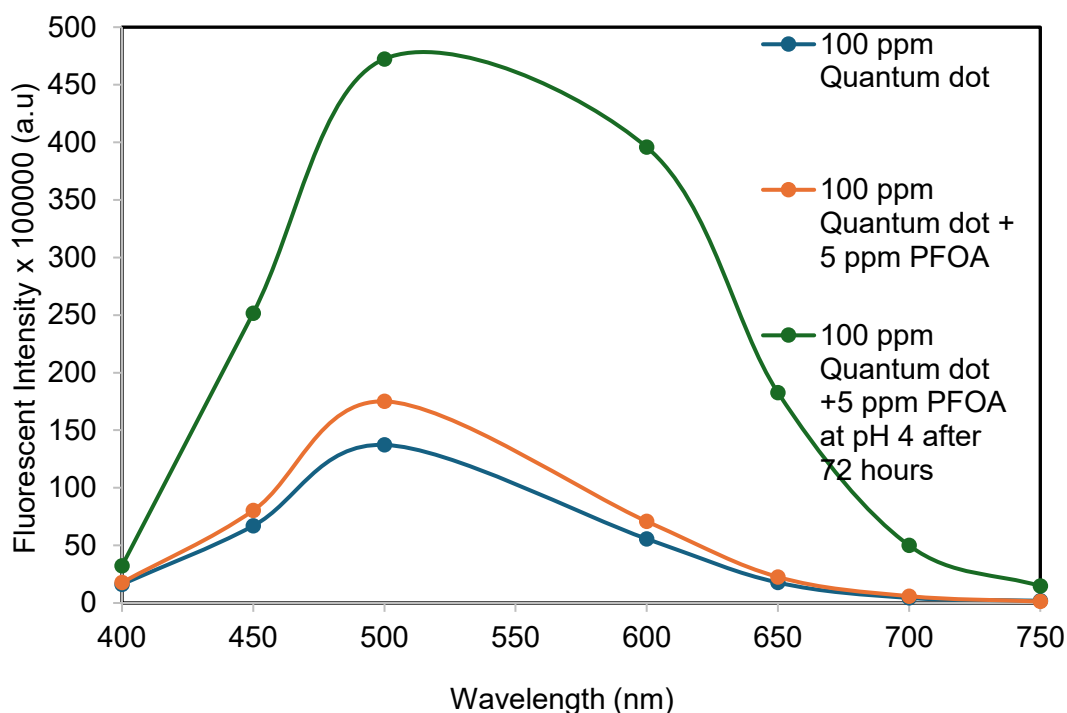


Figure 5.13. Representing the change in fluorescence of N-CDs with the addition of 5 mg/L PFOA.

Size, zeta potential, absorbance, and fluorescence measurements were conducted at various concentrations 1 ppm, 2.5 ppm, 5.0 ppm, and 7.5 ppm during the initial phase of experimentation. While these concentrations are significantly higher than typical environmental concentrations and often found in the range of parts per trillion (ppt) to parts per billion (ppb) they were intentionally selected to facilitate a clear and measurable assessment of the interaction mechanisms between N-CDs and PFAS (Perera & Meegoda, 2024). At these higher concentrations, physicochemical changes such as shifts in hydrodynamic size, zeta potential, absorbance and fluorescence intensities become more pronounced, allowing for a more accurate characterization of sorption behavior, electrostatic and hydrophobic interactions, and surface modifications. These mechanistic interactions form the foundation for developing a sensitive and selective quantum dot-based detection platform.

The findings from the current study could inform future experiments with more environmentally relevant PFAS concentrations to evaluate the sensitivity, selectivity, detection limits, and practical applicability of the N-CDs based sensing platform for drinking water monitoring. This study provides an approach to evaluate whether there any observable changes in the physicochemical properties of N-CDs upon interaction with various PFAS.

5.4 Detailed study of five individual PFAS

5.4.1 Perfluorooctanoic acid (PFOA)

Figure 5.14 illustrates the changes in hydrodynamic size and zeta potential of N-CDs at different concentrations of PFOA. The N-CDs exhibited their maximum size upon the addition of 1 ppm PFOA. As the PFOA concentration increased from 1 ppm to 5 ppm, the N-CDs size progressively decreased. Between 5 ppm and 7.5 ppm, the size reverted to its original value observed in the absence of PFOA. The observed increase in hydrodynamic size is likely due to particle destabilization driven by charge neutralization and subsequent aggregation. Conversely, the observed decrease in size may be attributed to particle re-stabilization, driven by enhanced electrostatic repulsion arising from excess negative charge introduced by PFOA molecules. The findings are also supported by the observed trend in the zeta potentials of N-CDs. Upon the addition of 1 ppm PFOA, the zeta potential markedly decreased from -13 mV to -6 mV, charge neutralization likely due to the interaction between carboxyl groups of PFOA and the amine functionalities of the N-CDs surface.

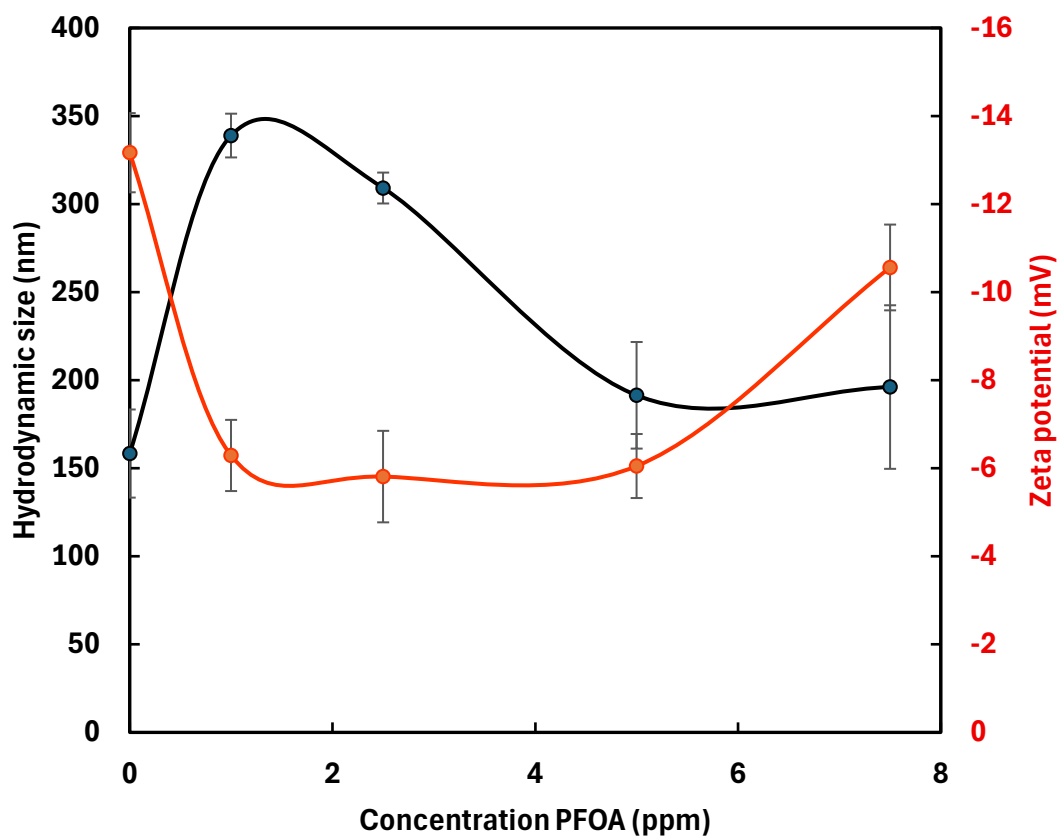


Figure 5.14. Effect of hydrodynamic size and zeta potential of N-CDs at different concentration of PFOA (1-7.5 ppm) at pH 4 ultrapure water.

As the PFOA concentration increased up to 5 ppm, the zeta potential remained relatively stable, suggesting saturation or equilibrium in surface binding. However, a further increase in concentration to 7.5 ppm resulted in a notable shift in zeta potential from -6 mV to -11 mV, implying additional surface interactions or changes in colloidal stability. The increase in size at 7.5 ppm is likely due to hydrophobic-hydrophobic interactions between N-CDs particle-bound PFOA and excess PFOA. Furthermore, the observed variations in hydrodynamic size and zeta potentials align well with the fluorescence behavior of N-CDs. Upon the addition of 1 ppm PFOA, fluorescence quenching was accompanied by an increase in particle size, suggesting aggregation or surface interaction effects. As PFOA concentration continued to rise, fluorescent intensity was progressively enhanced (Fig 5.15), indicating possible stabilization or

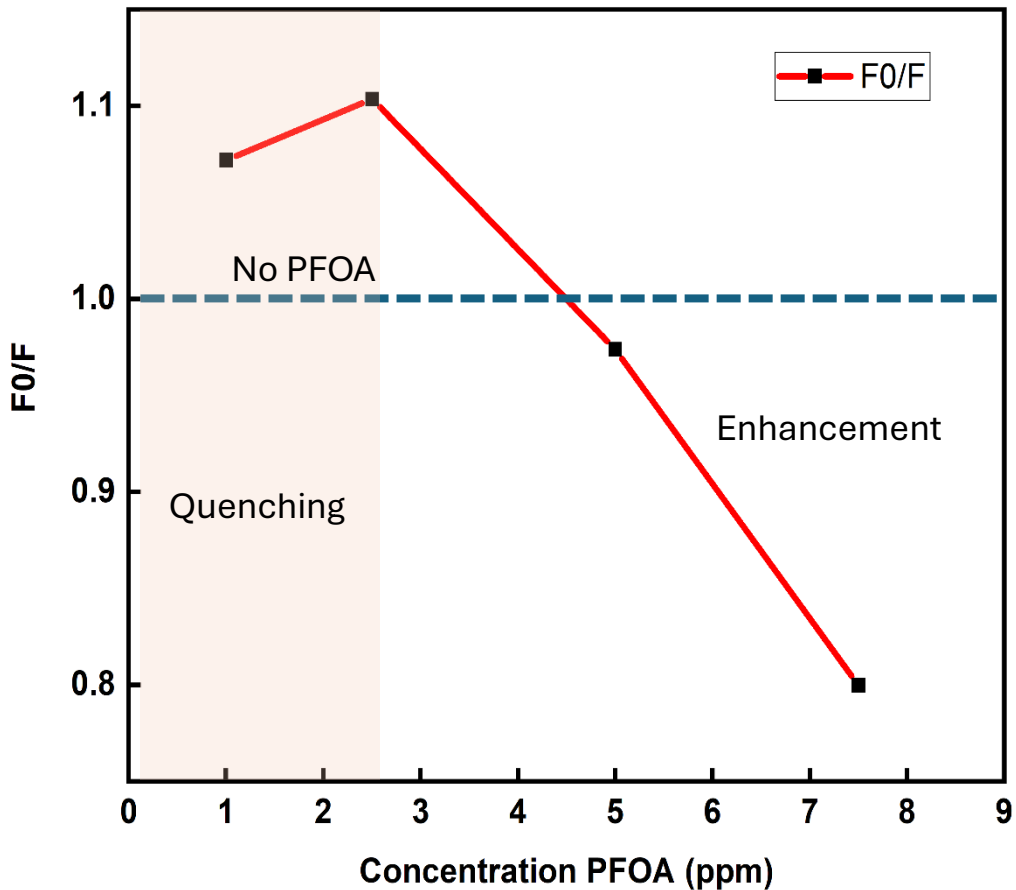


Figure 5.15. Stern – Volmer plot showing the variation in fluorescence intensity of N-CDs by the addition of PFOA at pH 4.

reconfiguration of surface states that favor fluorescence. The schematics of mechanism responsible for the observed changes in hydrodynamic size, zeta potential are illustrated in Fig 5.16.

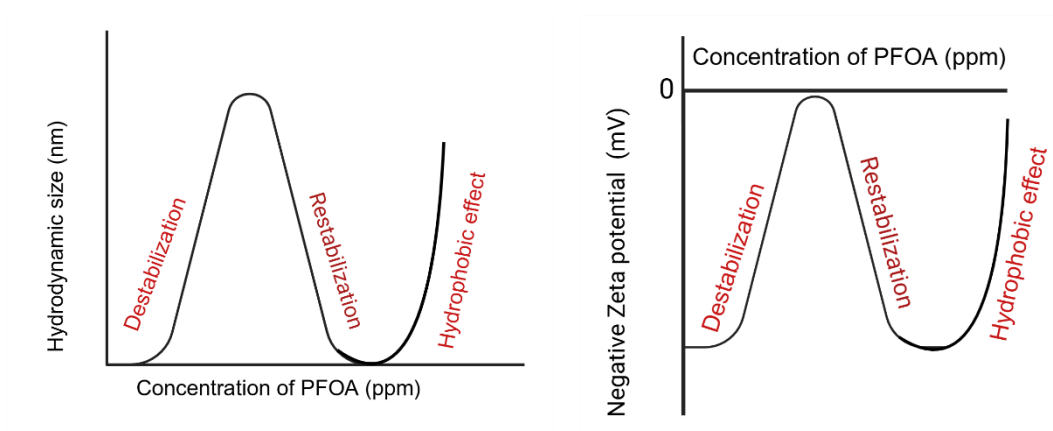


Figure 5.16. Schematic illustration depicting the trends in (a) hydrodynamic size and (b) zeta potential of N-CDs with increasing PFOA concentration, highlighting the mechanisms responsible for these changes.

5.4.2 Perfluorooctane sulfonic acid (PFOS)

Figure 5.17 illustrates the changes in hydrodynamic size and zeta potential of N-CDs at different concentrations of PFOS. Although PFOS and PFOA possess the same number of carbon atoms, their physicochemical behaviors differ significantly due to structural variations. PFOS contains an additional CF_2 unit, contributing to increased hydrophobicity, and features a sulfonate group which is relatively hard base that interacts more readily with oxide surfaces compared to the carboxylic group in PFOA (Fatima et al., 2025). PFOS exhibits a pronounced increase in hydrodynamic size, reaching 271 nm at 1 ppm and peaking at 356 nm at 2.5 ppm. In contrast, its zeta potential decreases gradually from -13 mV (control) to -5 mV at 5 ppm, indicating a consistent but less abrupt reduction in surface charge compared to PFOA.

At pH 4, the ionization of PFOS and PFOA diverges due to differences in their acid dissociation constants. PFOA, with a pK_a near 4, exists as a mixture of neutral ($-\text{COOH}$) and partially deprotonated ($-\text{COO}^-$) species. PFOS, with lower pK_a of 3.27, remains fully deprotonated as $-\text{SO}_3^-$, enhancing its electrostatic attraction to the protonated $-\text{NH}_3^+$ groups on N-CDs. This stronger ionic interaction is further supported by the higher charge density of the sulfonate group. Additionally, PFOS's increased hydrophobicity facilitates interparticle bridging at concentrations ≥ 5 ppm, potentially leading to associations with multiple N-CDs or other PFOS molecules. This results in larger aggregate formation and elevated hydrodynamic size and zeta potential values.

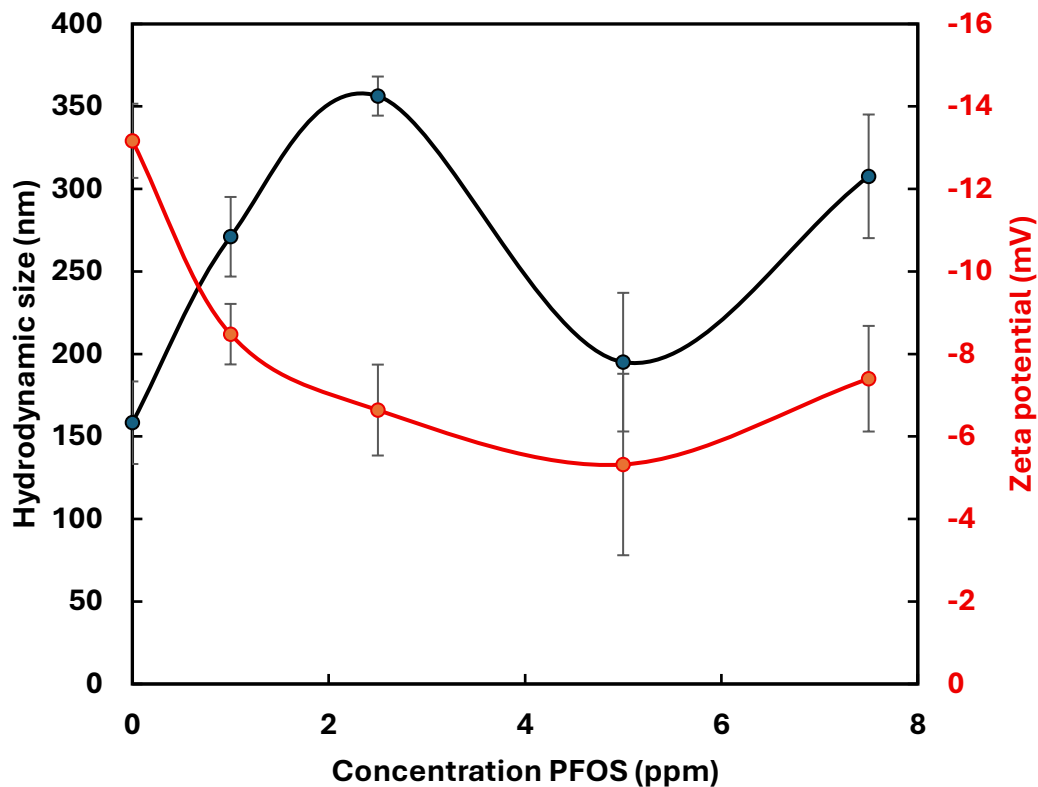


Figure 5.17. Effect of hydrodynamic size and zeta potential of N-CDs at different concentration of PFOS (1-7.5 ppm) at pH 4 in ultrapure water.

One-way ANOVA analysis confirms that PFOS significantly influences the physicochemical properties of N-CDs across varying concentrations. For hydrodynamic size, ANOVA yielded an F-value of 7.26 with a p-value of 0.0052, indicating statistically significant differences. The peak size at 2.5 ppm (356 nm), which was significantly higher than the control (158 nm), suggesting enhanced aggregation or surface interaction. For zeta potential, one-way ANOVA revealed a statistically significant effect of PFOS concentration, with an F-value of 9.98 and a p-value of 0.0016. As PFOS concentration increased from 0 to 5 ppm, the zeta potential became less negative (-13 mV to -5 mV), indicating adsorption of PFOS onto the N-CDs surface and a reduction in electrostatic stability. At 7.5 ppm, the zeta potential shifted slightly more negative (-7 mV), possibly due to surface reorganization or partial desorption. Furthermore, the observed variations in hydrodynamic size and zeta potentials align

well with the fluorescence behavior of N-CDs. Upon the addition of 1 ppm PFOA, fluorescence quenching was accompanied by an increase in particle size, suggesting aggregation or surface interaction effects. As PFOS concentration continued to rise, fluorescent intensity was progressively enhanced (Fig 5.18), indicating possible stabilization or reconfiguration of surface states that favor fluorescence. The findings of hydrodynamic size, zeta potential and fluorescence demonstrate that PFOS significantly influences the colloidal behavior of N-CDs in a concentration-dependent manner.

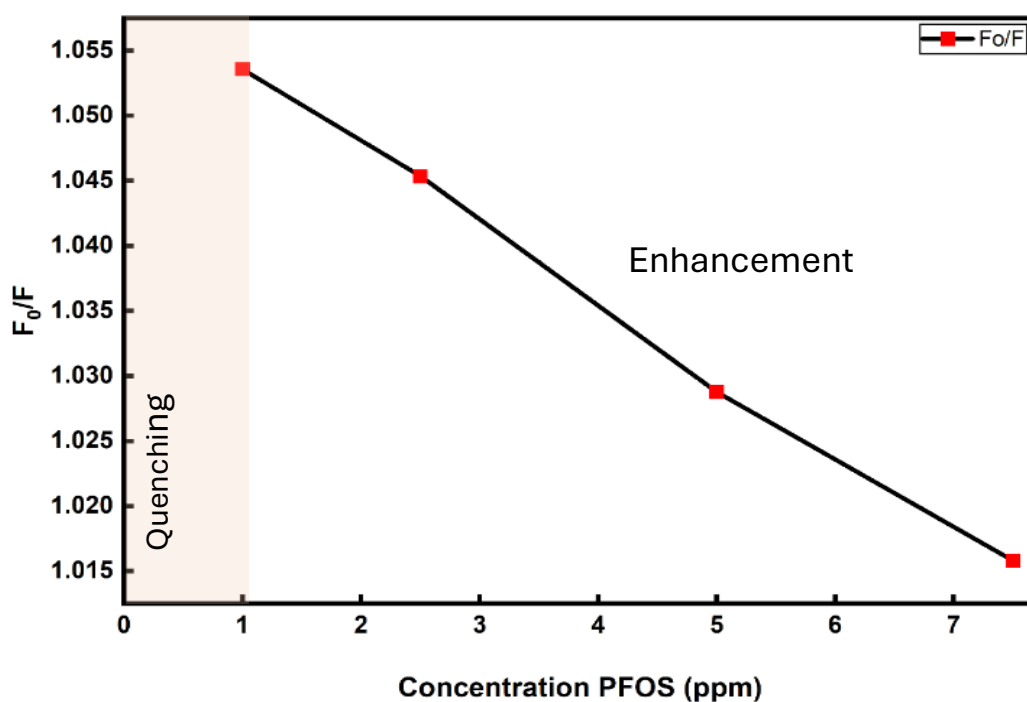


Figure 5.18. Stern–Volmer plot showing the variation in fluorescence intensity of N-CDs by the addition of PFOS (1-7.5 ppm) at pH 4.

5.4.3 Perfluorohexanoic acid (PFHxA)

Figure 5.19 illustrates the changes in hydrodynamic size and zeta potential of N-CDs at different concentrations of PFHxA. Shorter-chain PFAS, such as PFHxA, are

increasingly employed as substitutes for longer-chain analogs due to regulatory constraints. Their elevated aqueous mobility enhances their environmental dispersion and detection frequency in drinking water systems (Brendel et al., 2018). Figure 5.19 reveals that PFHxA induces pronounced fluctuations in hydrodynamic size and zeta potential of N-CDs across a range of concentrations, in contrast to PFOA and PFOS. At low PFHxA concentrations, a notable increase in hydrodynamic size coupled with a decline in zeta potential indicates N-CDs destabilization, likely driven partial surface neutralization and the initiation of weak interparticle bridging (aggregation).

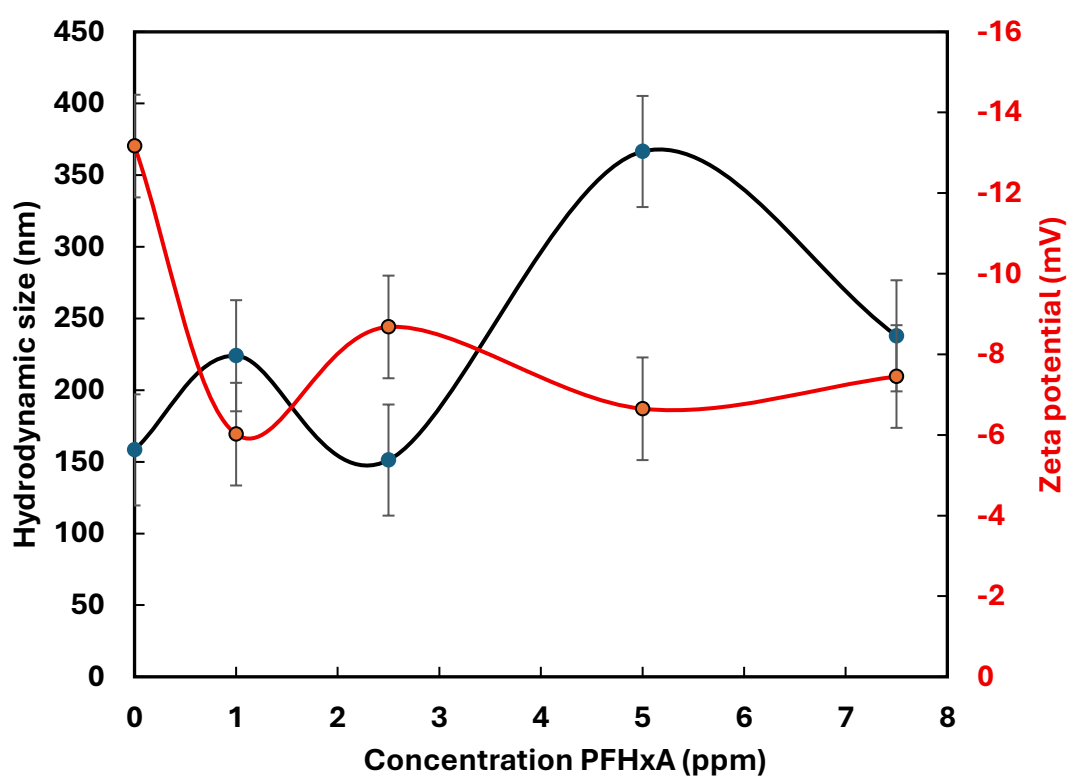


Figure 5.19. Effect of hydrodynamic size and zeta potential of N-CDs at different concentration of PFHxA (1-7.5 ppm) at pH 4 in ultrapure water.

A transitional restabilization phase emerges around 2.5 ppm, characterized by moderate increases in both hydrodynamic size and zeta potential, suggesting the formation of small, compact aggregates. At 5 ppm, a notable peak in hydrodynamic size and zeta potential stabilization around -10 mV denotes the formation of larger, cooperative

aggregates, potentially facilitated by surface charge crowding and cumulative hydrophobic interactions. Despite PFHxA's inherently lower hydrophobicity and surface activity, the observed non-linear aggregation behavior implies a concentration-dependent threshold effect, where extensive molecular adsorption onto N-CDs surfaces reduces electrostatic repulsion (zeta potential near 6.7 mV), enhancing particle-particle interactions.

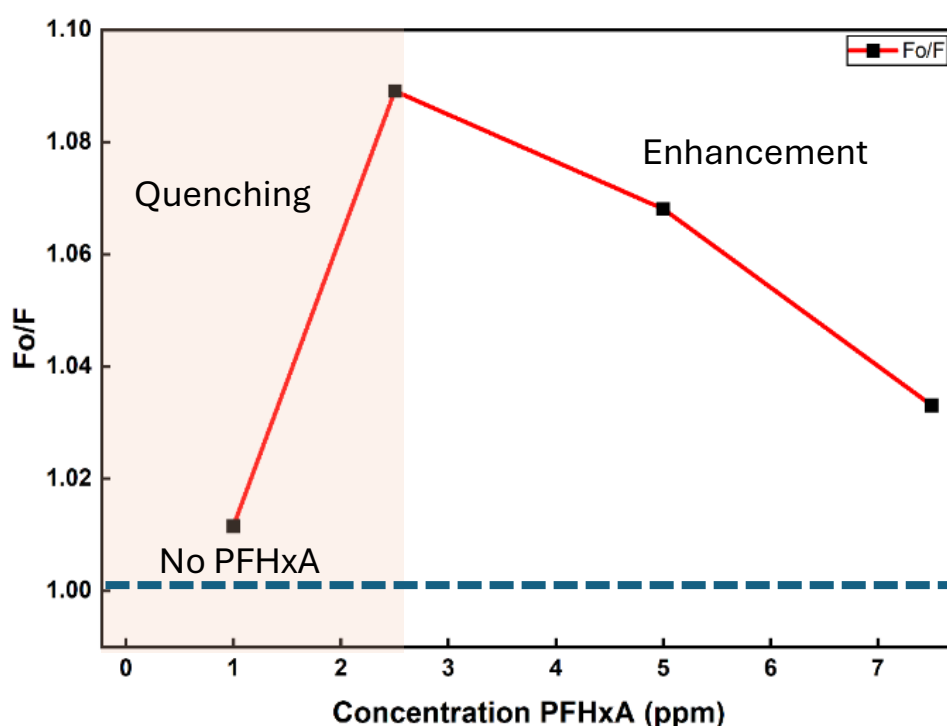


Figure 5.20. Stern – Volmer plot showing the variation in fluorescence intensity of N-CDs by the addition of PFHxA (1-7.5 ppm) at pH 4.

Furthermore, the observed variations in hydrodynamic size and zeta potentials align well with the fluorescence behavior of N-CDs. Upon the addition of 1 ppm PFHxA, fluorescence quenching was minimal, but the quenching became significant when the concentration was raised to 2.5 ppm. As PFHxA concentration increased further, fluorescent intensity continued to rise progressively (Fig 5.20), indicating possible stabilization or reconfiguration of surface states that favor fluorescence. These findings

underscore the distinct colloidal interaction mechanisms of short-chain PFAS and their potential implications for N-CDs stability and fluorescence in aqueous samples.

5.4.4 Perfluorononanoic acid (PFNA)

Figure 5.21 illustrates the changes in hydrodynamic size and zeta potential of N-CDs at different concentrations of PFNA. PFNA, a long-chain perfluoroalkyl carboxylic acid (C₉-COOH), exhibited strong physicochemical interactions with N-CDs, as evidenced by significant alterations in both hydrodynamic size and zeta potential.

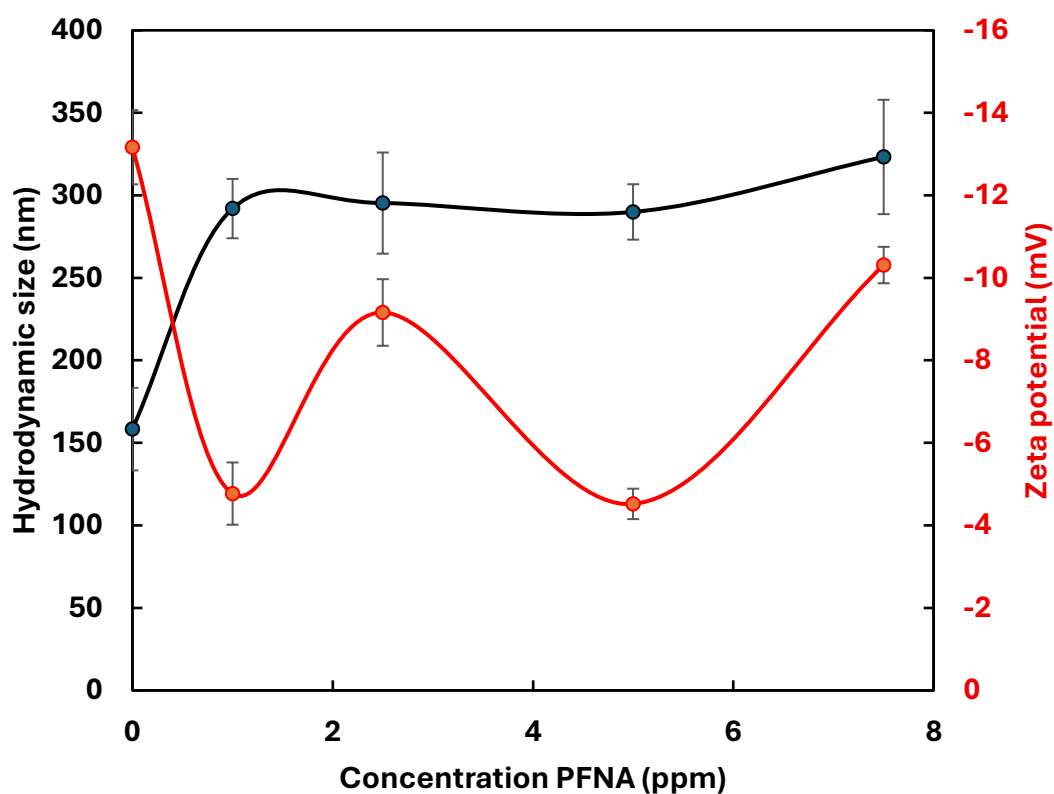


Figure 5.21. (a) Effect of hydrodynamic size and zeta potential of N-CDs at different concentration of PFNA (1-7.5 ppm) at pH 4 in ultrapure water.

At specific concentrations, PFNA adsorption onto N-CDs surfaces resulted in substantial modulation of surface charge without inducing changes in the hydrodynamic size of N-CDs, indicating surface-level interactions rather than bulk aggregation. The reduction in zeta potential magnitude, from -13 mV (control) to -4.5 mV at 5 ppm (ANOVA: $F= 58.37$, $p< 0.0001$), is attributed to the incorporation of

PFNA's carboxylate groups, which partially neutralize the N-CDs surface. Concurrently, the fluorinated alkyl chains of PFNA orient outward, forming a hydrophobic corona that enhances steric stabilization and interparticle repulsion. This configuration suppresses Van der Waals attraction and prevents interparticle bridging (aggregation), thereby maintaining colloidal stability.

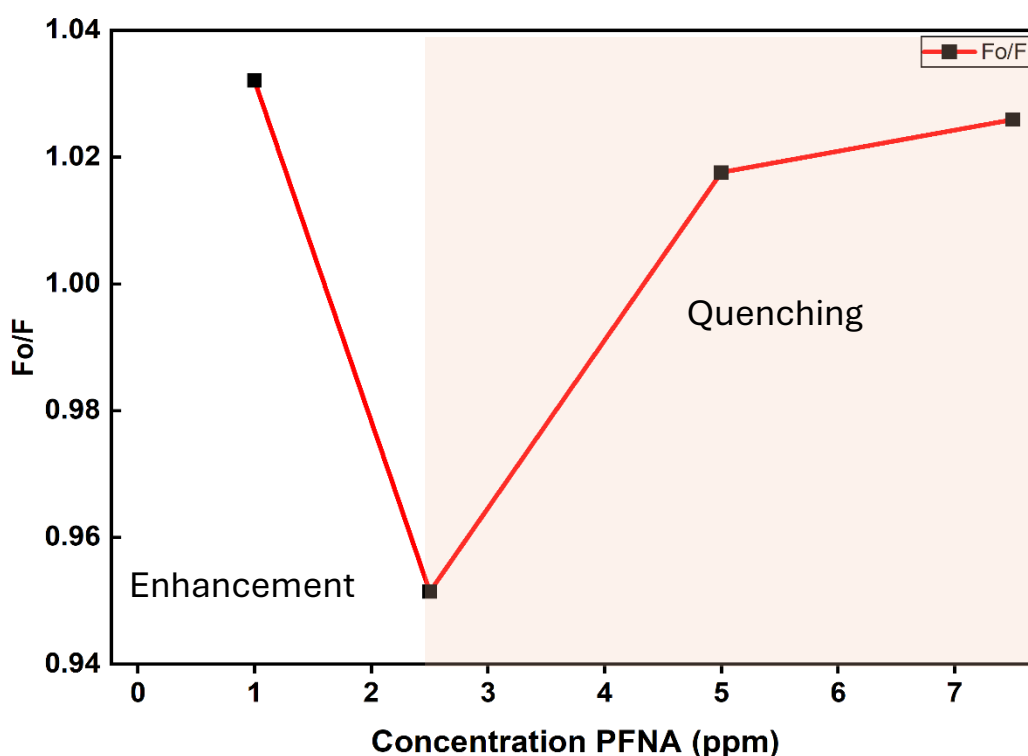


Figure 5.22. Stern–Volmer plot showing the variation in fluorescence intensity of N-CDs by the addition of PFNA (1-7.5 ppm) at pH 4.

Despite initial stability, a concentration-dependent increase in hydrodynamic size was observed, peaking at 323 nm at 7.5 ppm (ANOVA: $F= 17.98$, $p= 0.00015$), suggesting a threshold-driven transition possibly linked to surface saturation or rearrangement of adsorbed PFNA layers. Notably, zeta potential at 7.5 ppm decreased again to -10 mV, implying a secondary electrostatic reorganization or multilayer adsorption effect. Compared to PFOA (C8, $-\text{COOH}$) and PFOS (C8, $-\text{SO}_3\text{H}$), PFNA induced a more

gradual and sustained increase in hydrodynamic size across all tested concentrations, likely due to its extended fluorinated chain enhancing hydrophobic interactions and steric effects.

While PFOS promoted rapid aggregation and PFOA caused more abrupt zeta potential shifts at intermediate concentrations, PFNA's behavior suggests a dominant hydrophobic stabilization mechanism, modulated by electrostatic surface interactions and concentration-dependent adsorption dynamics. Furthermore, the observed changes in fluorescence behavior, followed by quenching, align well (Fig. 22) with the variations in hydrodynamic size and zeta potentials of N-CDs (Fig. 21).

5.4.5 Nonafluorobutane-1-sulfonic acid (PFBS)

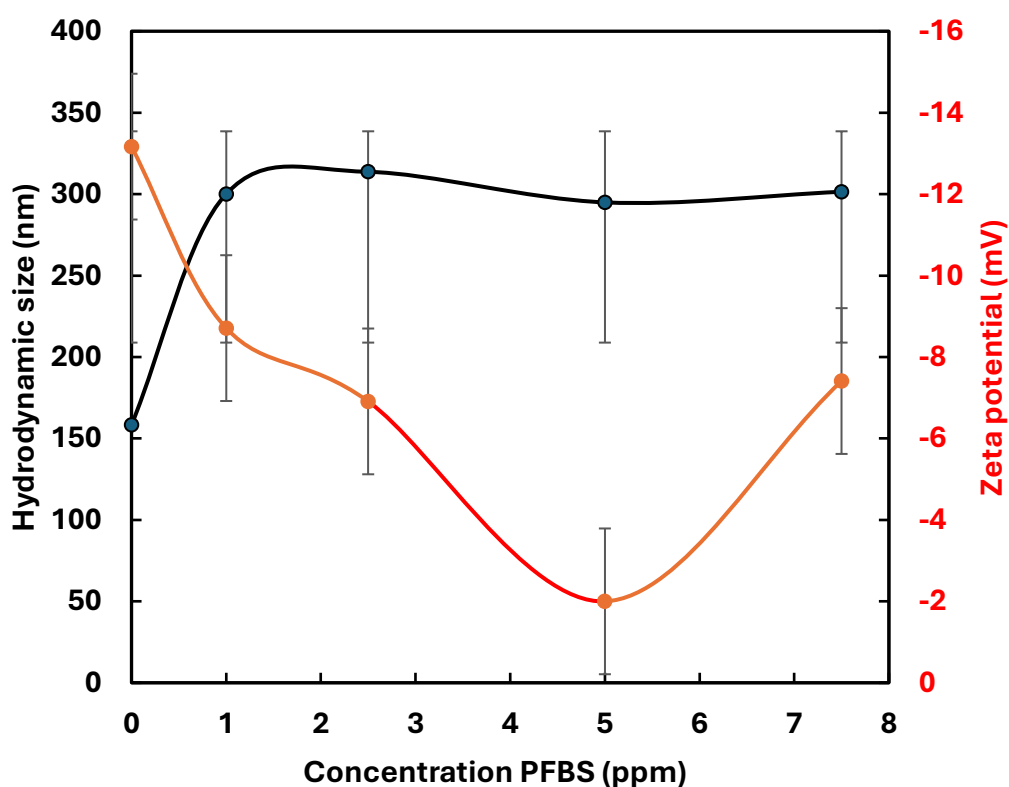


Figure 5.23. (a) Effect of hydrodynamic size and zeta potential of N-CDs at different concentration of PFBS (1-7.5 ppm) at pH 4 in ultrapure water.

Figure 5.23 illustrates the changes in hydrodynamic size and zeta potential of N-CDs at different concentrations of PFBS. PFBS, a short-chain PFAS ($C_4 - SO_3H$),

demonstrated distinct colloidal interaction behavior with N-CDs compared to its longer-chain analogs.

The hydrodynamic size of N-CDs increased from 158 nm (control) to 314 nm at 2.5 ppm (ANOVA: $F= 3.66$, $p= 0.0437$) but remained relatively stable across higher PFBS concentrations (293-314 nm), indicating limited aggregation. In contrast, zeta potential exhibited a strongly concentration-dependent shift from -13 mV (control) to -2 mV at 5 ppm (ANOVA: $F= 40.18$, $p<0.0001$), reflecting substantial surface charge neutralization due to PFBS adsorption.

At lower concentrations, PFBS adsorption partially neutralized the N-CDs surface charge, reducing electrostatic repulsion and enabling the formation of aggregates that are twice the size of the control. The reduced hydrophobicity of PFBS due to short perfluorinated chain limited the interparticle bridging and hydrophobic-hydrophobic interactions. As PFBS concentration increased, further adsorption altered the surface charge, but the absence of extended hydrophobic tails and the high aqueous mobility of PFBS promoted dynamic, reversible surface interactions rather than stable aggregate formation.

The sulfonic acid moiety of PFBS contributes strong electrostatic affinity for the N-CDs surface, yet its short chain length restricts hydrophobic stabilization. Consequently, PFBS-induced colloidal behavior is dominated by surface-level adsorption and repulsive stabilization mechanisms. Compared to PFNA (C9-COOH), PFOA (C8-COOH), and PFOS (C8-SO₃H), PFBS elicited similar zeta potential shifts but exhibited a more moderate and consistent aggregation profile. Furthermore, the observed changes in fluorescence behavior, quenching followed by enhancement, aligns well (Fig 5.24) with the variations in hydrodynamic size and zeta potentials of

N-CDs (Fig 5.23). These findings underscore the role of chain length and functional group chemistry in modulating N-CDs - PFAS interactions, with PFBS favoring electrostatic over hydrophobic mechanisms.

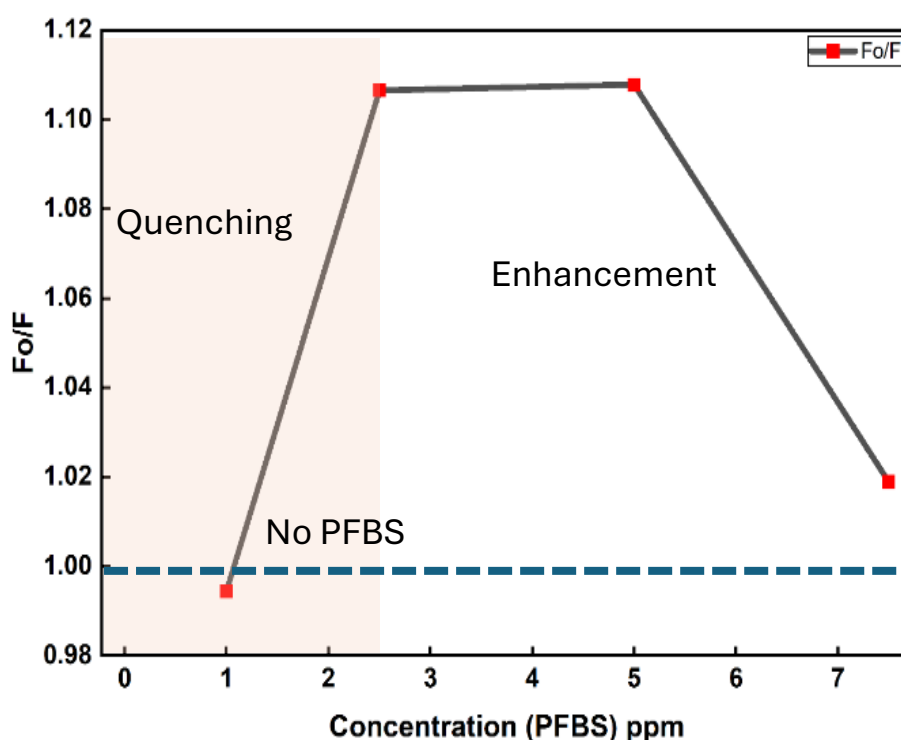


Figure 5.24. Stern–Volmer plot showing the variation in fluorescence intensity of N-CDs by the addition of PFBS (1-7.5 ppm) at pH 4.

5.5 Comparing the size and zeta potential based on carbon chain length

Figures 5.25 to 5.28 summarized the effect of fluorinated carbon chain length on hydrodynamic size and zeta potential. The interaction between N-CDs and five structurally distinct PFAS compounds was assessed by monitoring changes in hydrodynamic size and zeta potential across increasing PFAS concentrations (1–7.5 ppm). The interaction between N-CDs and five structurally distinct PFAS compounds was assessed by monitoring changes in hydrodynamic size and zeta potential across increasing PFAS concentrations (1–7.5 ppm).

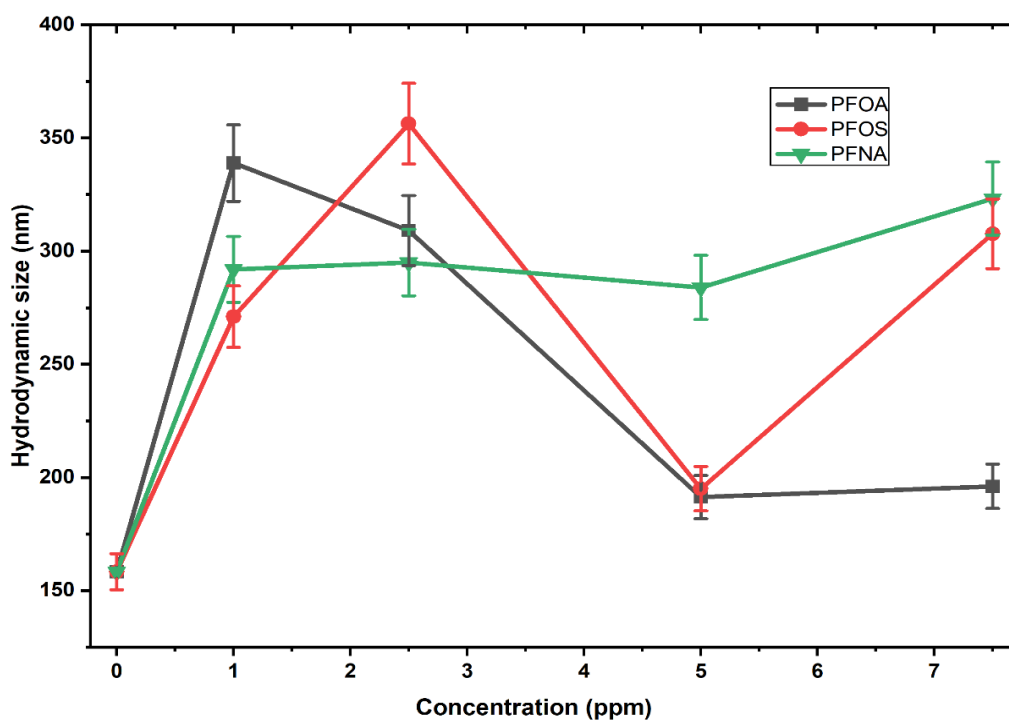


Figure 5.25. Hydrodynamic size variation of N-CDs upon interaction with long-chain PFAS (PFOA, PFOS, PFNA) at pH 4.

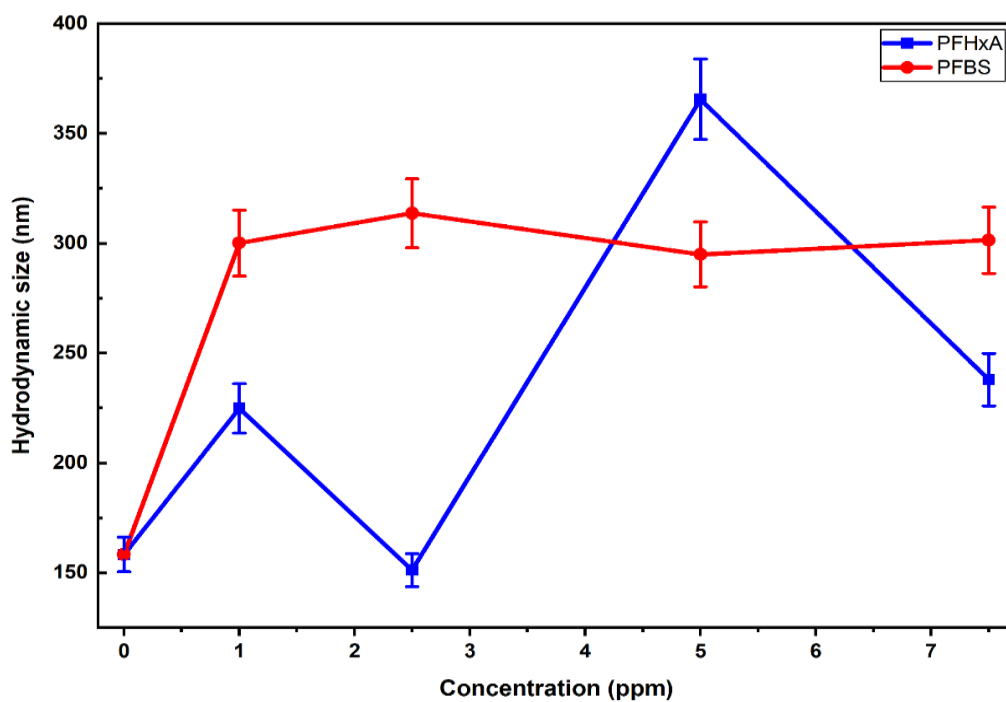


Figure 5.26. Hydrodynamic size variation of N-CDs upon interaction with short-chain PFAS (PFHxA, and PFBS) at pH 4.

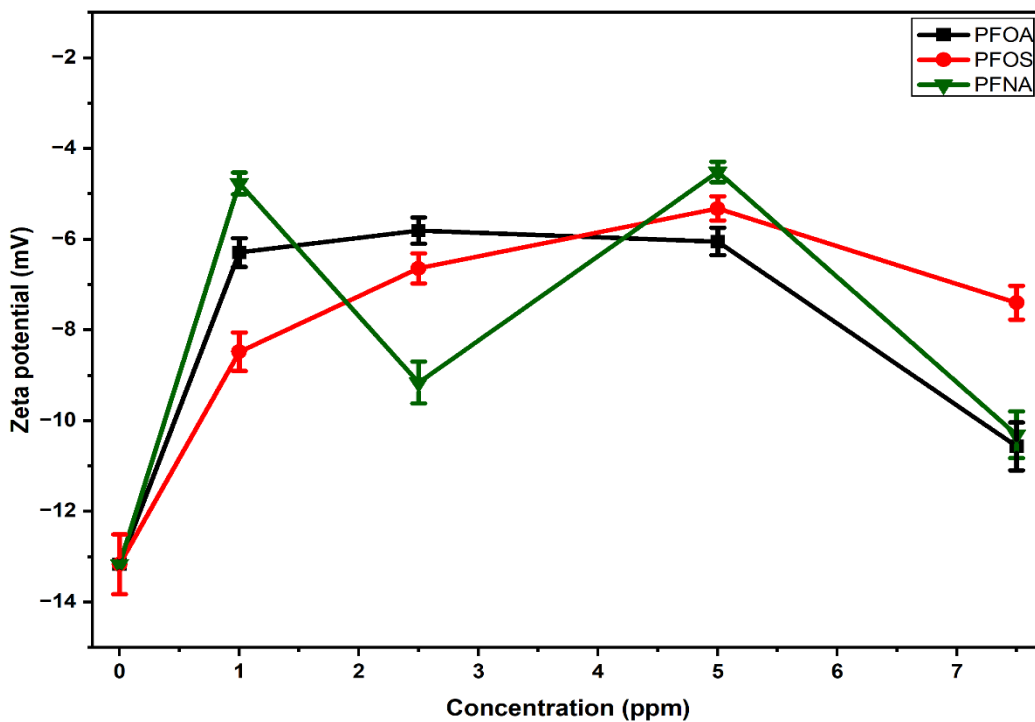


Figure 5.27. Zeta potential variation of N-CDs upon interaction with short-chain PFAS (PFOA, PFOS, PFNA) at pH 4.

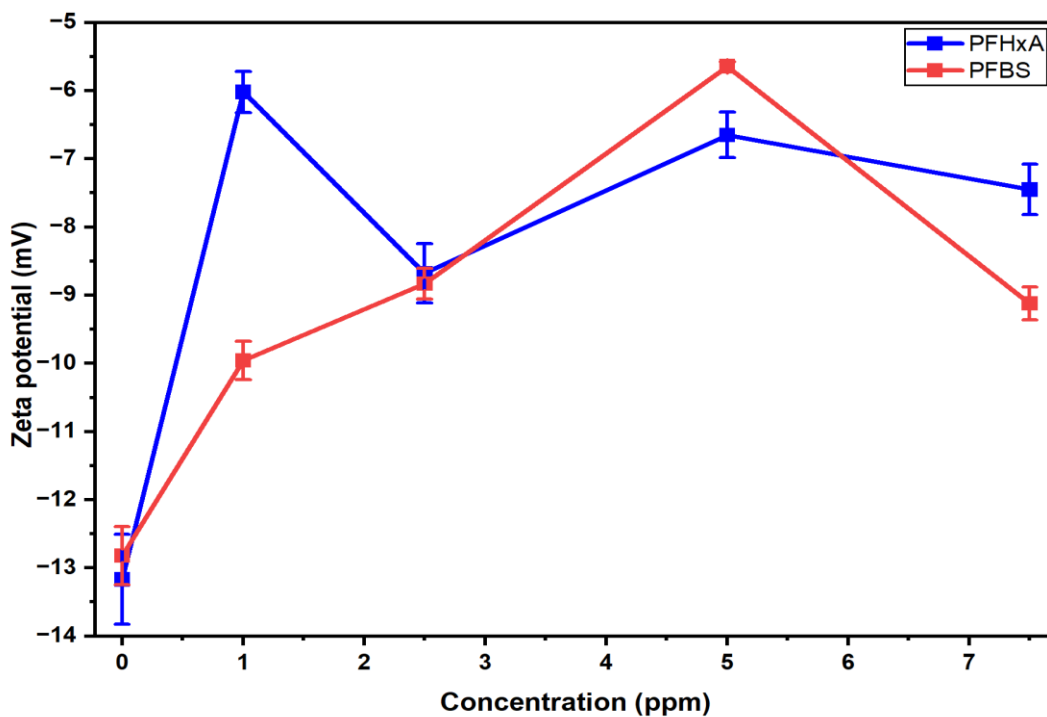


Figure 5.28. Zeta potential variation of N-CDs upon interaction with short-chain PFAS (PFHxA, PFBS) at pH 4.

Long-chain PFAS namely PFNA, PFOS, and PFOA exhibited significant increases in hydrodynamic size, particularly at lower concentrations, indicating strong initial adsorption onto the N-CDs surfaces. PFNA showed a gradual and stable increase in size, likely due to enhanced hydrophobic interactions from its longer carbon chain, while PFOS demonstrated a dynamic size profile, reflecting strong yet concentration-sensitive electrostatic interactions via its sulfonic head group. In contrast, PFOA displayed an initial size increase followed by a reduction at higher concentrations, suggesting potential rearrangement or desorption from the surface. Short-chain PFAS showed varied behavior: PFBS, despite its shorter chain, maintained a consistently large hydrodynamic size, likely due to strong electrostatic interactions conferred by its sulfonate group, whereas PFHxA induced erratic size changes, indicative of weak and reversible binding. Corresponding zeta potential measurements revealed a general shift toward less negative values upon PFAS addition, supporting surface adsorption. Sulfonate-containing PFAS (PFOS, PFBS) caused more pronounced charge neutralization than carboxylates, confirming the dominant role of electrostatic interactions in PFAS–N-CDs binding, particularly at acidic pH where amine groups on N-CDs are protonated. Collectively, these findings highlight that PFAS chain length and functional group chemistry play a crucial role in modulating the interaction strength and binding behavior with N-CDs.

5.6 Selectivity test

The fluorescence response of N-CDs in the presence of various common ions and PFAS is illustrated in Figure 5.29. The $(F-F_0)/F_0$ values were calculated to assess the relative change in fluorescence intensity upon exposure to each analyte, where F_0 is the fluorescence of N-CDs alone and F is the intensity after adding the interference ions. Most of the tested cations Na^+ , K^+ , Ca^{2+} , Mg^{2+} , Cu^{2+} and anions Cl^- , NO_3^- , SO_4^{2-}

induced only minor changes in fluorescence, indicating low interference. The similar results were reported (Lin et al., 2019). In contrast, PFAS, particularly PFBS and PFNA, caused a significant decrease in fluorescence, suggesting stronger interactions with N-CDs. The mixture of all PFAS showed the highest level of quenching, indicating possible cumulative or synergistic effects. These results highlight the selectivity of N-CDs toward PFAS over common environmental ions, supporting their potential application as a sensing platform for PFAS detection.

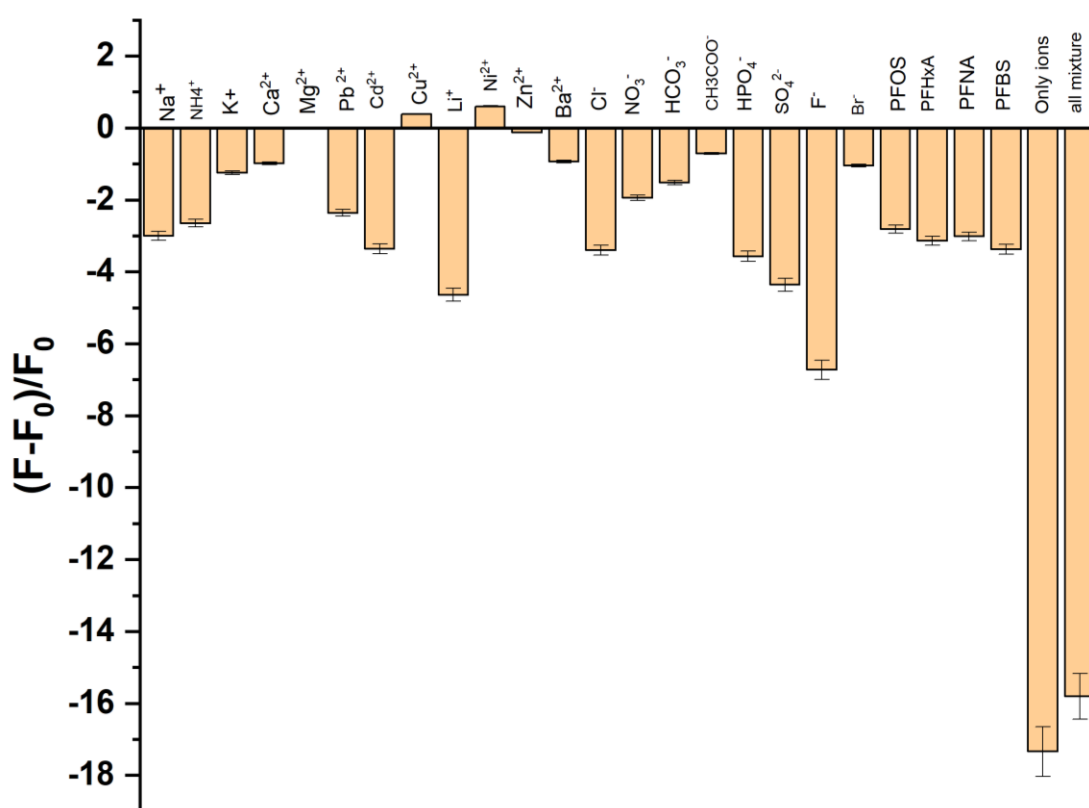


Figure 5.29. Fluorescence response ((F-F₀)/F₀) of nitrogen-doped carbon dots (N-CDs) upon interaction with different interfering ions (cations and anions), individual PFAS compounds (PFOS, PFHxA, PFNA, PFBS), and their mixture. Measurements were conducted at pH 4 with excitation at 365 nm.

5. 7 Elemental composition and bonding information after the addition of PFAS

X-ray Photoelectron Spectroscopy (XPS) was conducted to investigate the surface interaction mechanism between N-CDs and long-chain PFAS compounds, specifically PFOA and PFOS. Table 5.4 and 5.5 shows the elemental composition of the N-CDs,

after the addition of PFOA and PFOS (Fig 5.30 and 5.34), respectively. By comparing the XPS spectra of N-CDs before and after the addition of PFOA and PFOS, changes in the binding energies of key elements such as carbon (C 1s) (Fig 5.31 and Fig 5.35), nitrogen (N 1s) (Fig 5.32 and 5.36), and oxygen (O 1s) (Fig 5.33 and 5.37) were evaluated to determine possible (Fig 5.31, 5.32 and 5.33) interactions. The appearance or shift of specific peaks provides insights into potential electrostatic interactions, hydrogen bonding, or surface complexation. Furthermore, the detection of fluorine (F 1s) or sulfur (S 2p) peaks confirms the successful adsorption or interaction of PFOA and PFOS on the N-CDs surface. Overall, XPS analysis serves as a crucial tool to validate the proposed sensing mechanism and surface binding behavior of PFAS compounds with N-CDs. And it confirms the electrostatic interaction between PFAS and N-CDs.

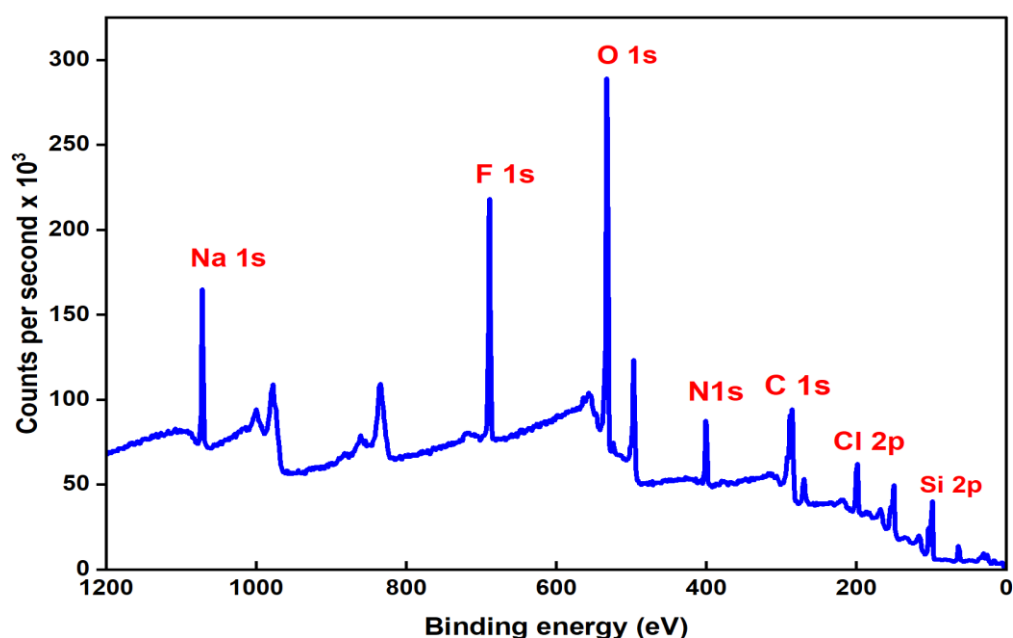


Figure 5.30. Wide scan spectrum of N-CDs with the interaction of PFOA showing the presence of Na 1s O 1s, N 1s, C 1s, F 1s, Cl 2p, and Si 2p peaks

Table 5.4. Elemental composition of N-CDs After interaction with PFOA

	BE (eV)	FWHM (eV)	RS F	Atomic conc. (%)	Error (%)	Mass conc. (%)	Error (%)
Si 2p	98.80	2.30	0.33	11.6	0.26	19.0	0.38
Cl 2p	198.80	3.35	0.89	3.2	0.14	6.6	0.29
C 1s	285.80	5.86	0.28	34.7	0.61	24.3	0.50
N 1s	400.80	2.77	0.48	6.6	0.26	5.3	0.21
O 1s	532.80	3.02	0.78	26.7	0.38	24.8	0.34
F 1s	688.80	2.98	1.00	13.3	0.29	14.7	0.31
Na 1s	1071.80	2.57	1.69	3.9	0.11	5.2	0.15

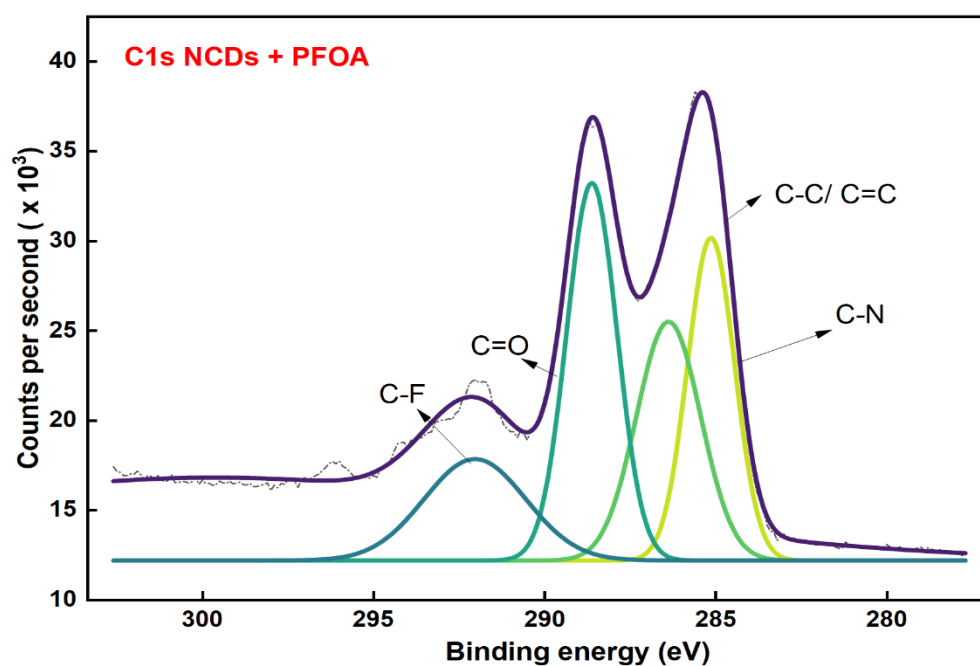


Figure 5.31. High-Resolution C 1s XPS spectra of N-CDs after interaction with PFOA

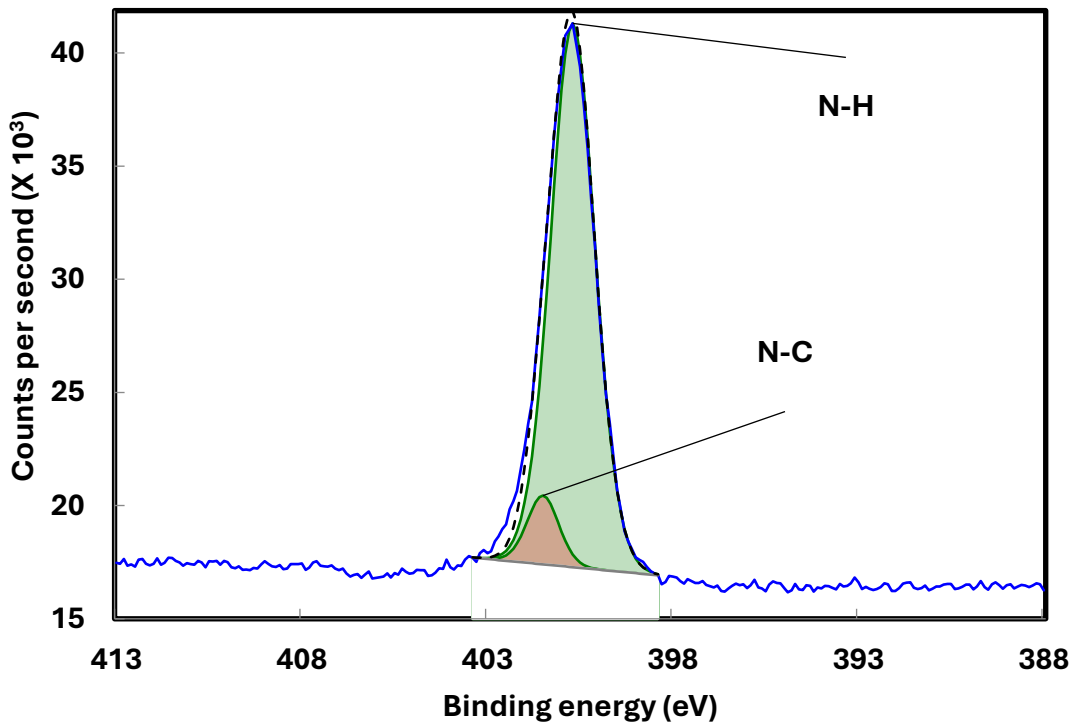


Figure 5.32. High-Resolution N1s XPS spectra of N-CDs after interaction with PFOA

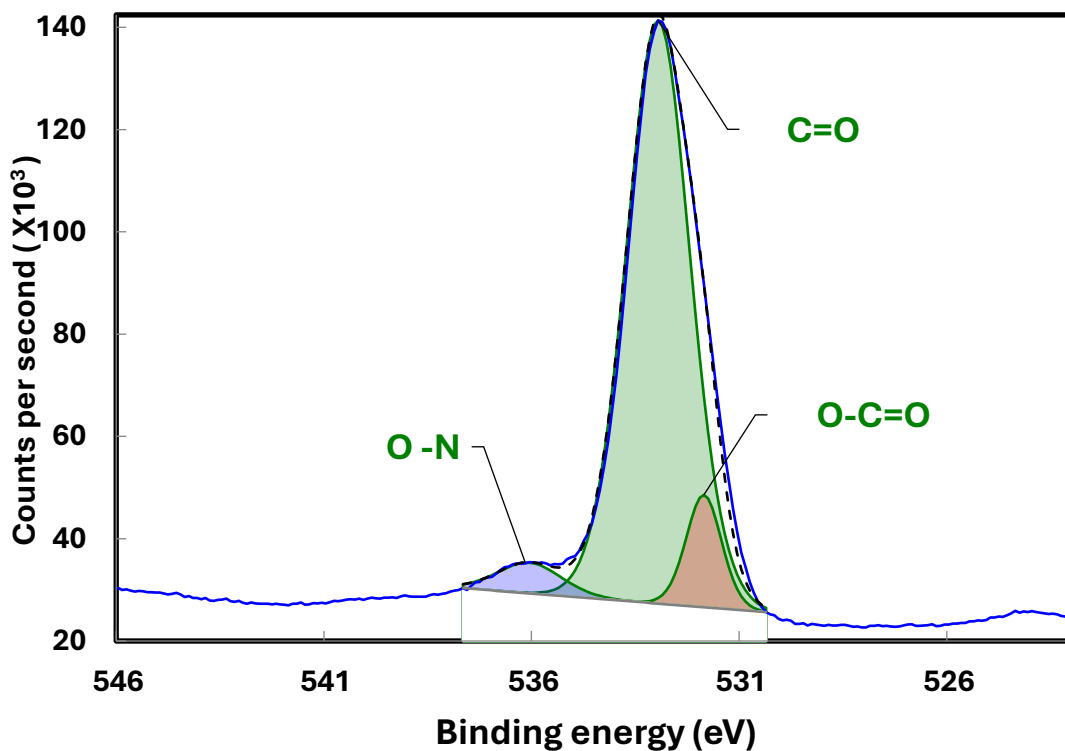


Figure 5.33. High-Resolution N 1s XPS spectra of N-CDs after interaction with PFOA

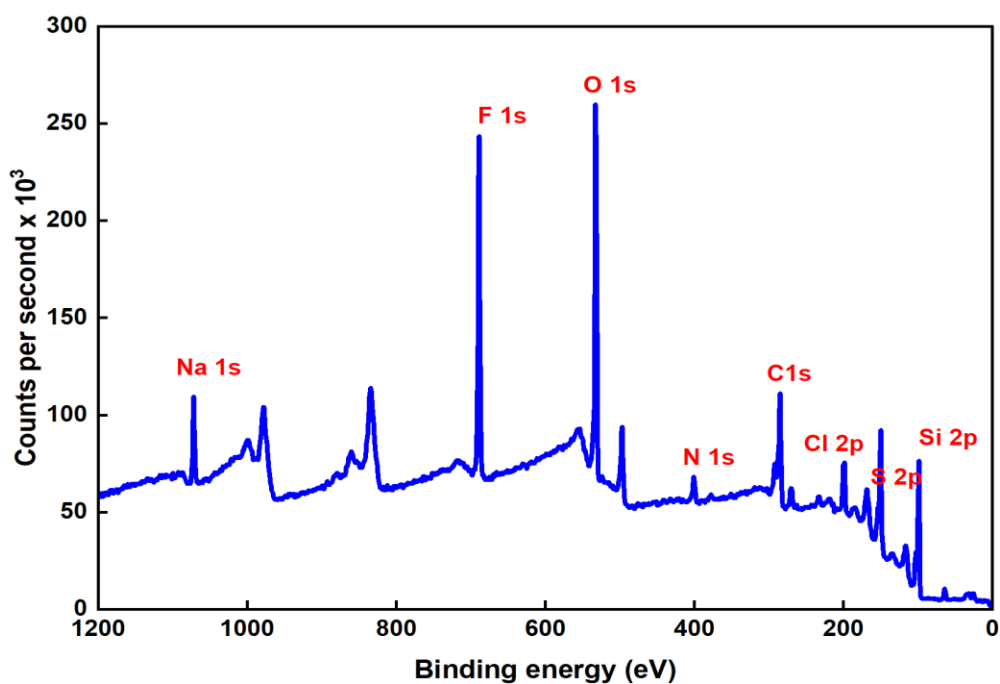


Figure 5.34. Wide scan spectrum of N-CDs with the interaction of PFOS showing the presence of Na 1s O 1s, N 1s, C 1s, F1s, Cl 2p, and Si 2p peaks.

Table 5.5. Elemental composition of N-CDs After interaction with PFOS

	BE (eV)	FWHM (eV)	RS F	Atomic conc. (%)	Error (%)	Mass conc. (%)	Error (%)
Si 2p	98.80	2.24	0.33	18.6	0.32	27.3	0.41
S 2p	167.80	5.83	0.67	5.7	0.30	9.6	0.48
Cl 2p	198.80	3.37	0.89	3.1	0.19	5.7	0.34
C 1s	284.80	3.22	0.28	29.4	0.76	18.4	0.56
N 1s	400.80	3.37	0.48	2.8	0.33	2.0	0.25
O 1s	532.80	2.76	0.78	22.4	0.39	18.7	0.31
F 1s	688.80	2.81	1.00	15.7	0.31	15.6	0.29
Na 1s	1071.80	2.78	1.69	2.2	0.11	2.6	0.14

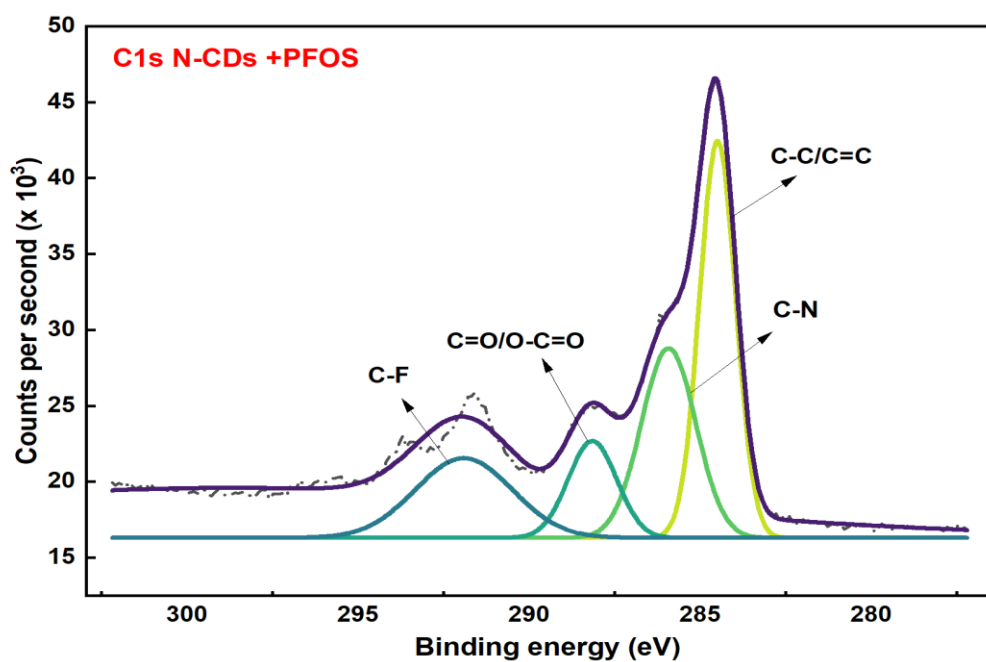


Figure 5.35. High-Resolution C 1s XPS spectra of N-CDs after interaction with PFOS

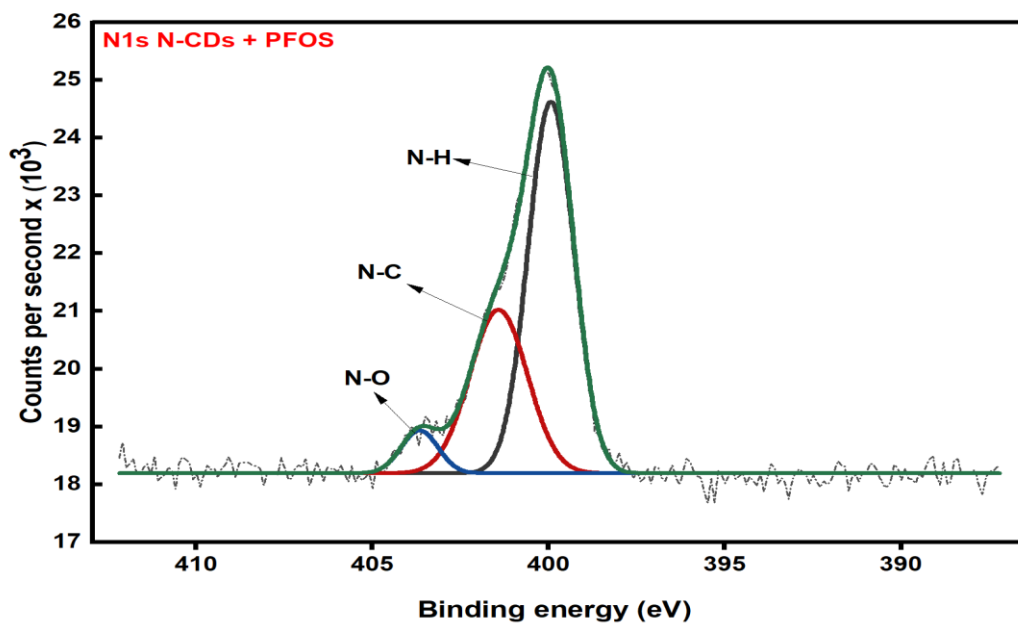


Figure 5.36. High-Resolution N1s XPS spectra of N-CDs after interaction with PFOS

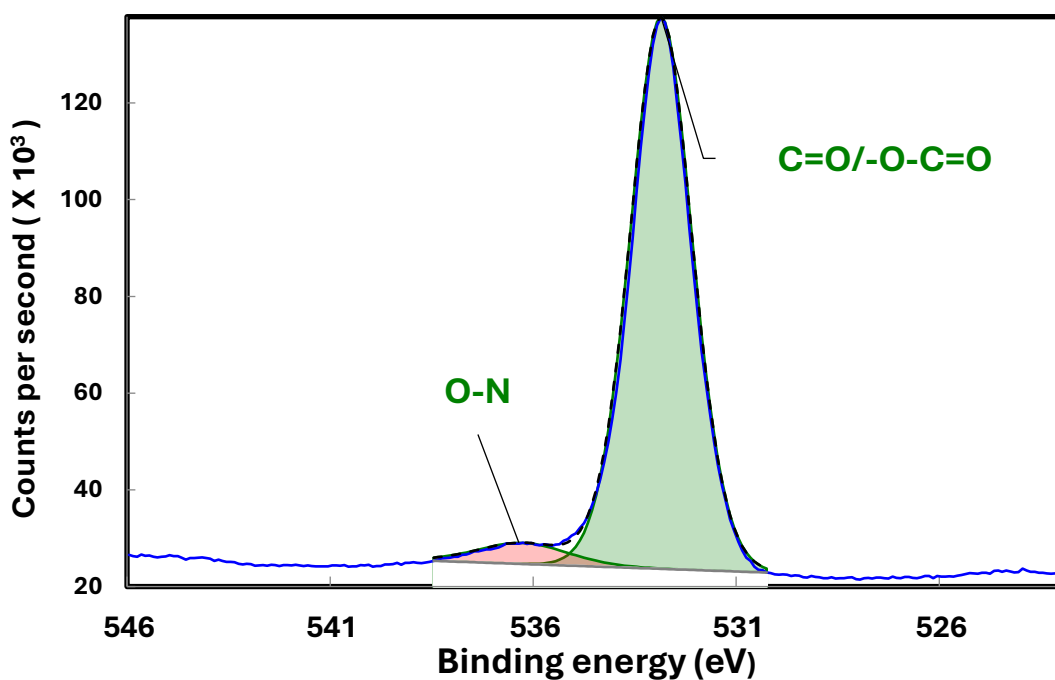


Figure 5.37. High-Resolution O1s XPS spectra of N-CDs after interaction with PFOS

5.8 Mechanistic interaction between PFAS and N-CDs

5.8.1 Electrostatic interactions

The possible interactions that can happen between N-CDs and PFAS are electrostatic interactions, hydrophobic interactions, and hydrogen bonding. The acid dissociation constant (pKa) value of commonly occurred PFAS in the environment is low, so they mostly occur in anionic species at environmentally relevant pH values (Wang et al., 2021). Even though the different study reported different pKa values, but it still is low enough for PFAS to yield anionic species in natural water. So, negatively charged anions of PFAS can interact with positively charged amine groups of N-CDs which is termed as electrostatic interaction. This interaction is sensitive to pH and coexisting ions in background. Since we confirmed our N-CDs has surface functional groups including -NH_2 , -OH , -COOH and C-OH and they can act as the critical active sites for PFAS interaction. Under low pH conditions, these functional groups can be

protonated and converted into positively charged ions ($-\text{NH}_2^+$, $-\text{COOH}_2^+$, $-\text{COH}^{2+}$, $-\text{OH}_2^+$) which have high chances to higher interaction of PFAS through electrostatic attraction. But, if the pH is high, the functional groups will lose their hydrogen ions, get deprotonated and there will be electrostatic attraction between N-CDs and PFAS. There will be a chance that both functional groups and PFAS acquire negative charge, so they push each other away, making it harder for interaction between PFAS and N-CDs ((Deng et al., 2015; Wang et al., 2021). In addition to pH, the increasing the ionic strength can also compress the electric double layer of N-CDs which reduces the electrostatic attraction between N-CDs and PFAS.

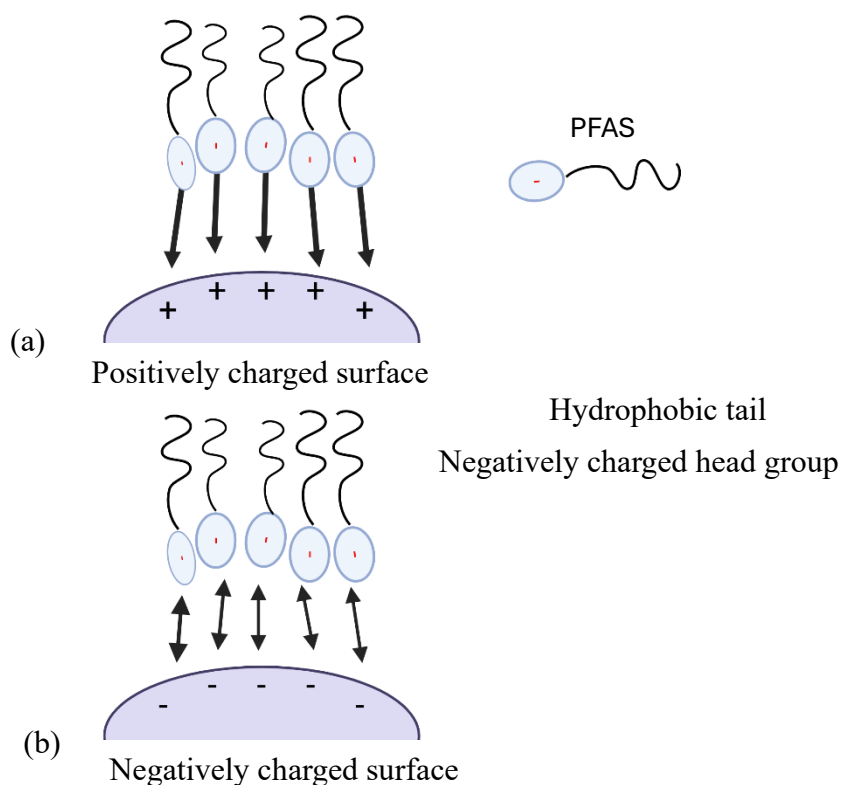


Figure 5.38. (a) Electrostatic attraction and (b) Electrostatic repulsion

When we compare both PFOA and PFOS, even though they have same number of carbon atoms, there are some major differences between them. PFOS has one extra CF_2 unit which make them more hydrophobic and sulfonate group in PFOS is relatively hard base which readily interacts on the oxide surfaces, which enhances the interaction between compared to carboxylic group (Fatima et al., 2025). This enhances the overall adsorption affinity of PFOS, especially in systems involving metal oxides or functionalized nanomaterials. In the context of electrostatic interactions with N-CDs, PFOS is expected to exhibit stronger binding than PFOA due to its lower pKa and the higher ionic character of the sulfonate group, which facilitates stronger electrostatic attraction

Since, N-CDs exhibit maximum fluorescence intensity at pH 4, which is the reason we have chosen pH 4 as the reference point for evaluating interactions with PFAS compounds. At pH 4, the functional groups of both PFOA and PFOS display different ionization behavior that significantly influence their interaction with N-CDs. The carboxylic acid group in PFOA has a pKa close to 4, meaning that at pH 4, it exists as a mixture of neutral ($-\text{COOH}$) and partially deprotonated ($-\text{COO}^-$) species. In contrast, PFOS contains a sulfonic acid group with a much lower pKa (3.27), which remains fully deprotonated under these conditions and exists entirely in the negatively charged $-\text{SO}_3^-$ form. Meanwhile, the amine groups present on the surface of N-CDs are protonated at pH 4, forming positively charged $-\text{NH}_3^+$ groups. This creates favorable electrostatic conditions for interactions with negatively charged PFAS molecules. Due to the complete deprotonation of PFOS and the higher charge density of its sulfonate group, PFOS is expected to exhibit stronger electrostatic attraction to the protonated N-CDs than PFOA.

5.8.2 Hydrophobic interactions

Hydrophobic interaction describes non-polar long-chain hydrophobic molecules with the tendency to repel polar molecules and with high affinity to attach on hydrophobic surface (Chandler, 2005).

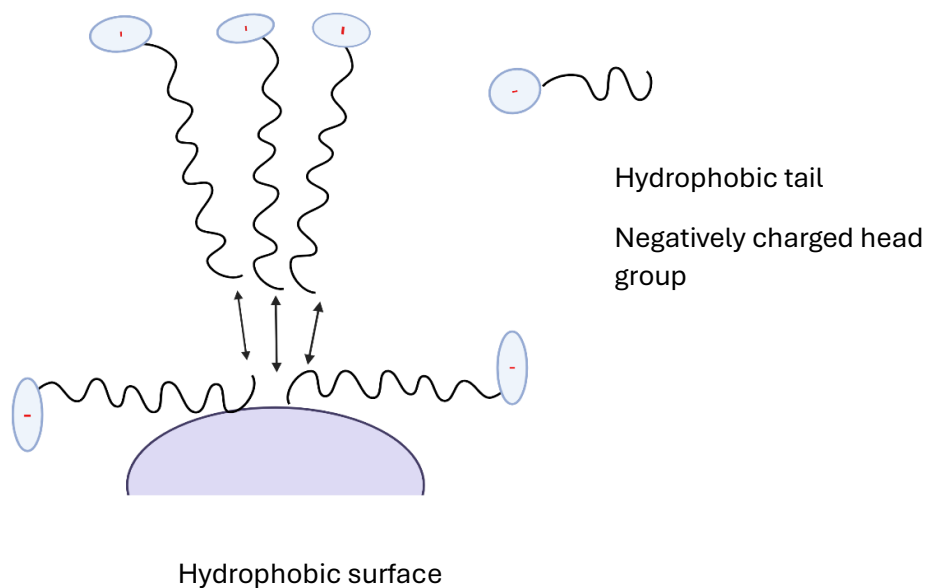


Figure 5.39. Hydrophobic interaction

N-CDs have graphitic carbon while PFAS have hydrophobic C-F chains which allows non-specific hydrophobic interactions between N-CDs and various PFAS. It has been reported that PFAS anions can be adsorbed onto negatively charged adsorbents, suggesting that the hydrophobic interaction can overcome the electrostatic repulsion between both negatively charged PFAS anions and adsorbents (Deng et al., 2015; Tang et al., 2010b; Yang et al., 2013; Zhou et al., 2010b). Specific mechanistic interactions for each PFAS are shown in the Figure 5.40.

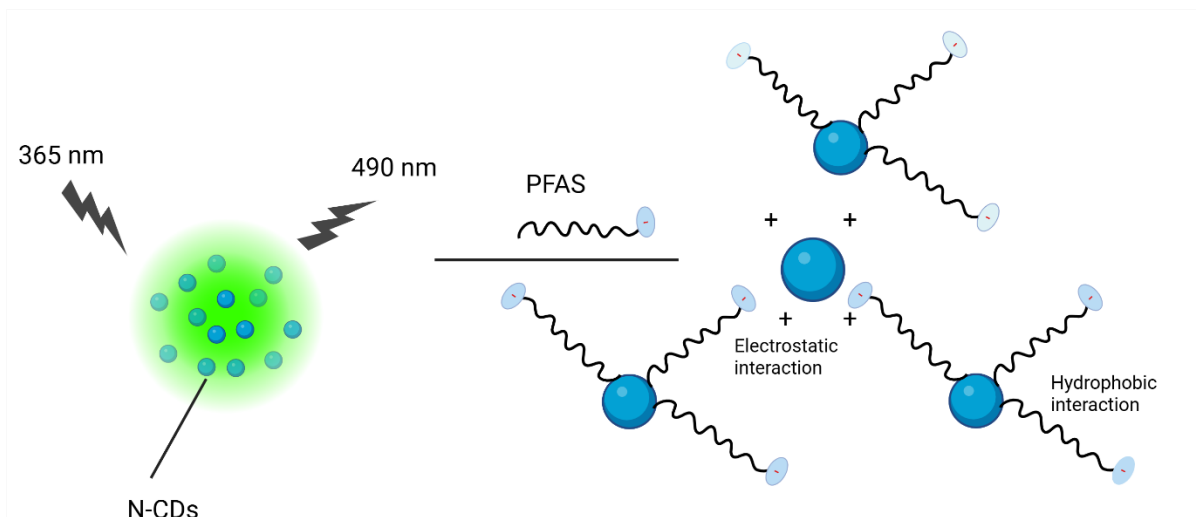


Figure 5.40. Schematic mechanism between N-CDs and PFAS showing the combined effect of electrostatic and hydrophobic effect.

When we compare the response of size, zeta potential and fluorescence response the interaction between N-CDs and each PFAS molecule behave differently with each other. We can confirm that there is a combination of both electrostatic and hydrophobic interactions are the main source of interactions. Initially when we add low concentration of PFAS the dominant mechanism is electrostatic while higher the concentration the hydrophobic effect comes to picture based on carbon chain length.

6. CONCLUSIONS

Fluorescent N-CDs exhibit high sensitivity to PFAS, with their fluorescence strongly influenced by pH, PFAS chain length, functional groups, and concentration in ultrapure water. Among five of the PFAS compounds, PFOA and PFOS shows better response than other molecules. Specific electrostatic attractions and non-specific hydrophobic–hydrophobic interactions including sorption and interparticle bridging played critical roles in fluorescence quenching and enhancement, respectively. At pH 4, N-CDs showed strong potential as fluorescent probes for elucidating the interaction mechanisms of various PFAS compounds. These findings not only introduce N-CDs as a promising class of sorbents but also offer a platform to investigate how they interact with individual PFAS molecules through distinct physicochemical pathways. However, N-CDs without tailored surface functionalities lack the selectivity required to distinguish between individual PFAS species in the presence of background ions. Future efforts focused on modifying the surface chemistry of N-CDs could significantly enhance their selectivity and sensing capabilities, enabling their application as effective and affordable probes for PFAS detection in drinking water systems. The interaction between N-CDs and PFAS shows different mechanisms among five compounds.

Upon exposure to five EPA-regulated PFAS, clear changes in hydrodynamic size, zeta potential, and fluorescence emission were observed in individual and mixture of PFAS- containing N-CDs solutions were observed. These changes confirmed physicochemical interactions between PFAS molecules and the surface of N-CDs, driven mainly by both specific electrostatic attractions and non-specific hydrophobic interactions. The fluorescence emission of N-CDs was quenched in a concentration-dependent manner, and Stern–Volmer plots revealed both linear and nonlinear quenching behavior depending on PFAS type and concentration. Statistical analysis,

including one-way ANOVA, validated the significance of these changes across concentrations. An important insight from this study is that the N-CDs used contained only 5.1% nitrogen, which limited the number of amine functional groups available for specific PFAS binding. Future studies should therefore focus on synthesizing N-CDs with higher nitrogen content or introducing additional amine functionalities to enhance electrostatic interactions with PFAS head groups. Such modifications are expected to significantly improve both the sensitivity and selectivity of N-CDs based fluorescent probes. In addition, interference studies with the common ions showed negligible fluorescence changes, confirming the selectivity of N-CDs toward PFAS. However, further studies are needed to enhance the specificity of the N-CDs through chemical functionalization, which are yet to be discovered. Interestingly, individual PFAS compounds exhibited different modes of interaction with N-CDs, leading to distinct quenching and enhancement mechanisms. This diversity highlights that a single sensor design may not be universally effective for all PFAS species. Instead, tailored sensing platforms with customized receptor chemistries are necessary to achieve reliable detection and discrimination among different PFAS molecules. Overall, the findings collectively establish a strong proof-of-concept for using N-CDs as a low-cost, sensitive, and rapid fluorescent sensing platform for PFAS screening in aqueous environments, and they provide a foundation for further optimization at lower, environmentally relevant concentrations.

7. RECOMMENDATIONS FOR FUTURE WORK

Building upon the findings of this study, several key areas are recommended for future investigation to improve the applicability and performance of N-CDs in PFAS detection.

1. Equimolar interaction study

To better understand the fundamental interaction mechanisms between N-CDs and various PFAS compounds, future experiments should be conducted using equimolar concentrations of both components. This will help isolate the true interaction dynamics and provide a clearer picture of the binding stoichiometry and kinetics.

2. Tailoring N-CDs for enhanced specificity

While the current study highlights the general sensitivity of N-CDs toward PFAS, their lack of selectivity in the presence of background ions remains a limitation. Future research should focus on modifying the surface chemistry of N-CDs such as by introducing specific functional groups or molecular recognition elements to enhance selective binding to targeted PFAS compounds. Such functionalization could enable discrimination between PFAS types and improve reliability in complex environments.

3. High throughput detection platform development

To translate the sensing approach into a practical application, a high-throughput format should be developed. Using 96-well plate assays combined with tailored N-CDs will allow for the rapid screening of multiple PFAS types simultaneously. This approach can also be used to systematically determine the limit of detection (LOD) and quantify performance under standardized and controlled conditions, which is essential for regulatory and field deployment.

4. Specificity testing in environmental matrixes

To evaluate the real-world applicability of N-CD-based sensors, future studies must explore their performance in diverse environmental matrices, including drinking water, surface water (e.g., lakes and rivers), and groundwater. These systems introduce natural organic matter, ions, and other competing contaminants that may interfere with detection. Validating the performance of N-CDs under such conditions will help identify matrix effects, enhance robustness, and guide optimization strategies for field deployment.

8. INTELLECTUAL MERITS AND BROADER IMPACTS

This project addresses critical environmental and societal challenges by developing a cost-effective, selective, and sensitive sensor for PFAS detection using N-CDs in drinking water. Since the contamination caused by PFAS is drastically increasing, if we could develop a sensor, it would be helpful for people to use this as a screening tool to understand whether their drinking water is contaminated with PFAS. The research advances scientific knowledge by elucidating the interaction mechanisms between PFAS and N-CDs, paving the way for innovative sensor technologies. The low-cost sensor has the potential to enable widespread water quality monitoring, particularly in underserved and rural communities, improving public health and access to clean water. The research promotes public awareness and engagement with environmental issues through collaboration with stakeholders such as water utilities and community organizations. Additionally, the project supports economic competitiveness by advancing sensor technology toward commercialization and fostering partnerships between academia and industry. Currently, several research efforts are underway to develop optical and electrochemical sensors for PFAS detection; however, none have reached commercialization due to challenges such as poor selectivity, matrix interference, and high limits of detection (LOD) relative to regulatory thresholds. This study primarily focused on understanding the fundamental interaction mechanisms between N-CDs and five EPA-regulated PFAS molecules rather than solely achieving an ultra-low LOD. By elucidating how PFAS molecular structure, chain length, and functional groups influence fluorescence behavior, this work provides valuable mechanistic insights for the rational design of next-generation PFAS sensors. The findings indicate that by selecting or engineering suitable receptor molecules with

targeted surface functionalities, the sensitivity and selectivity of N-CDs based probes can be significantly improved.

9. REFERENCES

- Andrews, D. Q., & Naidenko, O. V. (2020). Population-Wide Exposure to Per- and Polyfluoroalkyl Substances from Drinking Water in the United States. *Environmental Science & Technology Letters*, 7(12), 931–936. <https://doi.org/10.1021/acs.estlett.0c00713>
- Ateia, M., Wei, H., & Andreescu, S. (2024). Sensors for Emerging Water Contaminants: Overcoming Roadblocks to Innovation. *Environmental Science & Technology*, 58(6), 2636–2651. <https://doi.org/10.1021/acs.est.3c09889>
- Berthold, T. A., McCrary, A., deVilleneuve, S., & Schramm, M. (2023). Let's talk about PFAS: Inconsistent public awareness about PFAS and its sources in the United States. *PLOS ONE*, 18(11), e0294134. <https://doi.org/10.1371/journal.pone.0294134>
- Brendel, S., Fetter, E., Staude, C., Vierke, L., & Biegel-Engler, A. (2018). Short-chain perfluoroalkyl acids: Environmental concerns and a regulatory strategy under REACH. *Environmental Sciences Europe*, 30(1), 9. <https://doi.org/10.1186/s12302-018-0134-4>
- Buck, R. C., Franklin, J., Berger, U., Conder, J. M., Cousins, I. T., De Voogt, P., Jensen, A. A., Kannan, K., Mabury, S. A., & Van Leeuwen, S. P. (2011). Perfluoroalkyl and polyfluoroalkyl substances in the environment: Terminology, classification, and origins. *Integrated Environmental Assessment and Management*, 7(4), 513–541. <https://doi.org/10.1002/ieam.258>
- Cheng, Z., Dong, H., Liang, J., Zhang, F., Chen, X., Du, L., & Tan, K. (2019). Highly selective fluorescent visual detection of perfluorooctane sulfonate via blue fluorescent carbon dots and berberine chloride hydrate. *Spectrochimica Acta Part A: Molecular and Biomolecular Spectroscopy*, 207, 262–269. <https://doi.org/10.1016/j.saa.2018.09.028>
- Choi, J. W., Oh, J., Bennett, D. H., Calafat, A. M., Schmidt, R. J., & Shin, H.-M. (2024). Prenatal exposure to per- and polyfluoroalkyl substances and child behavioral problems. *Environmental Research*, 251, 118511. <https://doi.org/10.1016/j.envres.2024.118511>
- Clark, R. B., & Dick, J. E. (2020a). Electrochemical Sensing of Perfluorooctanesulfonate (PFOS) Using Ambient Oxygen in River Water. *ACS Sensors*, 5(11), 3591–3598. <https://doi.org/10.1021/acssensors.0c01894>
- Clark, R. B., & Dick, J. E. (2020b). Electrochemical Sensing of Perfluorooctanesulfonate (PFOS) Using Ambient Oxygen in River Water. *ACS Sensors*, 5(11), 3591–3598. <https://doi.org/10.1021/acssensors.0c01894>
- Clark, R. B., & Dick, J. E. (2021). Towards deployable electrochemical sensors for per- and polyfluoroalkyl substances (PFAS). *Chemical Communications*, 57(66), 8121–8130. <https://doi.org/10.1039/D1CC02641K>
- Currie, S. D., Wang, J.-S., & Tang, L. (2024). Impacts of PFAS Exposure on Neurodevelopment: A Comprehensive Literature Review. *Environments*, 11(9), 188. <https://doi.org/10.3390/environments11090188>
- Danaei, M., Dehghankhold, M., Ataei, S., Hasanzadeh Davarani, F., Javanmard, R., Dokhani, A., Khorasani, S., & Mozafari, M. R. (2018). Impact of Particle Size and Polydispersity Index on the Clinical Applications of Lipidic Nanocarrier Systems. *Pharmaceutics*, 10(2), 57. <https://doi.org/10.3390/pharmaceutics10020057>

- Deng, S., Nie, Y., Du, Z., Huang, Q., Meng, P., Wang, B., Huang, J., & Yu, G. (2015). Enhanced adsorption of perfluorooctane sulfonate and perfluorooctanoate by bamboo-derived granular activated carbon. *Journal of Hazardous Materials*, 282, 150–157. <https://doi.org/10.1016/j.jhazmat.2014.03.045>
- Fang, C., Zhang, X., Dong, Z., Wang, L., Megharaj, M., & Naidu, R. (2018). Smartphone app-based/portable sensor for the detection of fluoro-surfactant PFOA. *Chemosphere*, 191, 381–388. <https://doi.org/10.1016/j.chemosphere.2017.10.057>
- Fatima, M., Kelso, C., & Hai, F. (2025). Perfluorooctanoic Acid (PFOA) and Perfluorooctanesulfonic Acid (PFOS) Adsorption onto Different Adsorbents: A Critical Review of the Impact of Their Chemical Structure and Retention Mechanisms in Soil and Groundwater. *Water*, 17(9), 1401. <https://doi.org/10.3390/w17091401>
- Islam, G. J., & Arrigan, D. W. M. (2022). Voltammetric Selectivity in Detection of Ionized Perfluoroalkyl Substances at Micro-Interfaces between Immiscible Electrolyte Solutions. *ACS Sensors*, 7(10), 2960–2967. <https://doi.org/10.1021/acssensors.2c01100>
- Jiao, Z., Li, J., Mo, L., Liang, J., & Fan, H. (2018). A molecularly imprinted chitosan doped with carbon quantum dots for fluorometric determination of perfluorooctane sulfonate. *Microchimica Acta*, 185(10), 473. <https://doi.org/10.1007/s00604-018-2996-y>
- Karimian, N., Stortini, A. M., Moretto, L. M., Costantino, C., Bogialli, S., & Ugo, P. (2018). Electrochemosensor for Trace Analysis of Perfluorooctanesulfonate in Water Based on a Molecularly Imprinted Poly(*o*-phenylenediamine) Polymer. *ACS Sensors*, 3(7), 1291–1298. <https://doi.org/10.1021/acssensors.8b00154>
- Khan, R., Uygun, Z. O., Andreescu, D., & Andreescu, S. (2024). Sensitive Detection of Perfluoroalkyl Substances Using MXene–AgNP-Based Electrochemical Sensors. *ACS Sensors*, 9(6), 3403–3412. <https://doi.org/10.1021/acssensors.4c00776>
- Korak, J. A., & McKay, G. (2024). Critical review of fluorescence and absorbance measurements as surrogates for the molecular weight and aromaticity of dissolved organic matter. *Environmental Science: Processes & Impacts*, 26(10), 1663–1702. <https://doi.org/10.1039/D4EM00183D>
- Kwok, K. Y., Yamazaki, E., Yamashita, N., Taniyasu, S., Murphy, M. B., Horii, Y., Petrick, G., Kallerborn, R., Kannan, K., Murano, K., & Lam, P. K. S. (2013). Transport of Perfluoroalkyl substances (PFAS) from an arctic glacier to downstream locations: Implications for sources. *Science of The Total Environment*, 447, 46–55. <https://doi.org/10.1016/j.scitotenv.2012.10.091>
- Leung, S. C. E., Wanninayake, D., Chen, D., Nguyen, N.-T., & Li, Q. (2023a). Physicochemical properties and interactions of perfluoroalkyl substances (PFAS)—Challenges and opportunities in sensing and remediation. *Science of The Total Environment*, 905, 166764. <https://doi.org/10.1016/j.scitotenv.2023.166764>
- Leung, S. C. E., Wanninayake, D., Chen, D., Nguyen, N.-T., & Li, Q. (2023b). Physicochemical properties and interactions of perfluoroalkyl substances (PFAS)—Challenges and opportunities in sensing and remediation. *Science of The Total Environment*, 905, 166764. <https://doi.org/10.1016/j.scitotenv.2023.166764>
- Lin, L., Zhou, S., Guo, H., Chen, Y., Lin, S., Yan, L., Li, K., & Li, J. (2019). Nitrogen-doped carbon dots as an effective fluorescence enhancing system for the

- determination of perfluorooctyl sulfonate. *Microchimica Acta*, 186(6).
<https://doi.org/10.1007/s00604-019-3501-y>
- Mahoney, H., Xie, Y., Brinkmann, M., & Giesy, J. P. (2022). Next generation per- and poly-fluoroalkyl substances: Status and trends, aquatic toxicity, and risk assessment. *Eco-Environment & Health*, 1(2), 117–131.
<https://doi.org/10.1016/j.eehl.2022.05.002>
- Menger, R. F., Beck, J. J., Borch, T., & Henry, C. S. (2022). Colorimetric Paper-Based Analytical Device for Perfluorooctanesulfonate Detection. *ACS ES&T Water*, 2(4), 565–572. <https://doi.org/10.1021/acsestwater.1c00356>
- Mohammadi, S., Dorado, Z. N., & Sharifan, H. (2024a). Nanoscale Fluorinated Carbon Dots for the Detection of Perfluorooctanoic Acid in Aqueous Systems: A Fluorescence Assay Enhanced by Fluorophilic Interactions. *ACS Applied Nano Materials*, 7(18), 21410–21419. <https://doi.org/10.1021/acsanm.4c03109>
- Mohammadi, S., Dorado, Z. N., & Sharifan, H. (2024b). Nanoscale Fluorinated Carbon Dots for the Detection of Perfluorooctanoic Acid in Aqueous Systems: A Fluorescence Assay Enhanced by Fluorophilic Interactions. *ACS Applied Nano Materials*, 7(18), 21410–21419. <https://doi.org/10.1021/acsanm.4c03109>
- Mohammadi, S., Sandoval-Pauker, C., Dorado, Z. N., Senftle, T. P., Pankow, R., & Sharifan, H. (2025). Fluorescent Sodium Alginate Hydrogel–Carbon Dots Sensor for Detecting Perfluorooctanoic Acid in Potable Water. *Analytical Chemistry*, 97(18), 10075–10084.
<https://doi.org/10.1021/acs.analchem.5c01991>
- Naidu, R., Nadebaum, P., Fang, C., Cousins, I., Pennell, K., Conder, J., Newell, C. J., Longpré, D., Warner, S., Crosbie, N. D., Surapaneni, A., Bekele, D., Spiese, R., Bradshaw, T., Slee, D., Liu, Y., Qi, F., Mallavarapu, M., Duan, L., ... Nathanail, P. (2020). Per- and poly-fluoroalkyl substances (PFAS): Current status and research needs. *Environmental Technology & Innovation*, 19, 100915.
<https://doi.org/10.1016/j.eti.2020.100915>
- Nawara, K., & Waluk, J. (2017). Improved Method of Fluorescence Quantum Yield Determination. *Analytical Chemistry*, 89(17), 8650–8655.
<https://doi.org/10.1021/acs.analchem.7b02013>
- Niu, H., Wang, S., Zhou, Z., Ma, Y., Ma, X., & Cai, Y. (2014). Sensitive Colorimetric Visualization of Perfluorinated Compounds Using Poly(ethylene glycol) and Perfluorinated Thiols Modified Gold Nanoparticles. *Analytical Chemistry*, 86(9), 4170–4177. <https://doi.org/10.1021/ac403406d>
- Noel, Noel, E., Mattana, G., & McGoron, A. (2025). *A Comparative Analysis of Nanoparticle Sizing Techniques for Enhanced Drug Delivery Applications*. Florida International University. <https://doi.org/10.25148/FIUURJ.3.1.5>
- Perera, D. C., & Meegoda, J. N. (2024). PFAS: The Journey from Wonder Chemicals to Environmental Nightmares and the Search for Solutions. *Applied Sciences*, 14(19), 8611. <https://doi.org/10.3390/app14198611>
- Peveler, W. J., Yazdani, M., & Rotello, V. M. (2016). Selectivity and Specificity: Pros and Cons in Sensing. *ACS Sensors*, 1(11), 1282–1285.
<https://doi.org/10.1021/acssensors.6b00564>
- Prado, M. B., Truong, N. T., & Wanekaya, A. K. (2023). Improving the quantum yield of nitrogen-doped carbon dots by varying dopant ratios and pH. *Sensors and Actuators Reports*, 6, 100165. <https://doi.org/10.1016/j.snr.2023.100165>
- Qian, B., Rayner, J. L., Davis, G. B., Trinchi, A., Collis, G., Kyratzis, I. (Louis), & Kumar, A. (2024). Per- and poly-fluoroalkyl substances (PFAS) sensing: A focus on representatively sampling soil vadose zones linked to nano-sensors.

- Ecotoxicology and Environmental Safety*, 284, 116932.
<https://doi.org/10.1016/j.ecoenv.2024.116932>
- Rehman, A. U., Crimi, M., & Andreescu, S. (2023). Current and emerging analytical techniques for the determination of PFAS in environmental samples. *Trends in Environmental Analytical Chemistry*, 37, e00198.
<https://doi.org/10.1016/j.teac.2023.e00198>
- Sendão, R. M. S., Esteves Da Silva, J. C. G., & Pinto Da Silva, L. (2023). Polyfluoroalkyl Substances (PFASs) Detection Via Carbon Dots: A Review. *Sustainable Chemistry*, 4(4), 339–362.
<https://doi.org/10.3390/suschem4040024>
- Shaw, M., Samanta, D., Shaik, M. A. S., Bhattacharya, A., Basu, R., Mondal, I., & Pathak, A. (2023). Solvent-induced switching between static and dynamic fluorescence quenching of N, S Co-doped carbon dots in sensing of Crotonaldehyde: A detailed systematic study. *Optical Materials*, 137, 113600.
<https://doi.org/10.1016/j.optmat.2023.113600>
- Takayose, M., Akamatsu, K., Nawafune, H., Murashima, T., & Matsui, J. (2012). Colorimetric Detection of Perfluorooctanoic Acid (PFOA) Utilizing Polystyrene-Modified Gold Nanoparticles. *Analytical Letters*, 45(18), 2856–2864. <https://doi.org/10.1080/00032719.2012.696225>
- Taylor, C. M., Ellingsen, T. A., Breadmore, M. C., & Kilah, N. L. (2021). Porphyrin-based colorimetric sensing of perfluorooctanoic acid as proof of concept for perfluoroalkyl substance detection. *Chemical Communications*, 57(88), 11649–11652. <https://doi.org/10.1039/D1CC04903H>
- Thompson, D., Zolfigol, N., Xia, Z., & Lei, Y. (2024). Recent progress in per- and polyfluoroalkyl substances (PFAS) sensing: A critical mini-review. *Sensors and Actuators Reports*, 7, 100189. <https://doi.org/10.1016/j.snr.2024.100189>
- Wang, Y., Darling, S. B., & Chen, J. (2021). Selectivity of Per- and Polyfluoroalkyl Substance Sensors and Sorbents in Water. *ACS Applied Materials & Interfaces*, 13(51), 60789–60814. <https://doi.org/10.1021/acsami.1c16517>
- Xu, X., Ray, R., Gu, Y., Ploehn, H. J., Gearheart, L., Raker, K., & Scrivens, W. A. (2004). Electrophoretic Analysis and Purification of Fluorescent Single-Walled Carbon Nanotube Fragments. *Journal of the American Chemical Society*, 126(40), 12736–12737. <https://doi.org/10.1021/ja040082h>
- Yin, H.-Q., Tan, K., Jensen, S., Teat, S. J., Ullah, S., Hei, X., Velasco, E., Oyekan, K., Meyer, N., Wang, X.-Y., Thonhauser, T., Yin, X.-B., & Li, J. (2021). A switchable sensor and scavenger: Detection and removal of fluorinated chemical species by a luminescent metal–organic framework. *Chemical Science*, 12(42), 14189–14197. <https://doi.org/10.1039/D1SC04070G>
- Zhang, F., Liang, J., Liu, Y., Zhou, Q., Hong, Y., Chen, X., & Tan, K. (2022). A highly sensitive dual-readout assay for perfluorinated compounds based CdTe quantum dots. *Spectrochimica Acta Part A: Molecular and Biomolecular Spectroscopy*, 269, 120753. <https://doi.org/10.1016/j.saa.2021.120753>
- Zheng, Z., Yu, H., Geng, W.-C., Hu, X.-Y., Wang, Y.-Y., Li, Z., Wang, Y., & Guo, D.-S. (2019). Guanidinocalix[5]arene for sensitive fluorescence detection and magnetic removal of perfluorinated pollutants. *Nature Communications*, 10(1), 5762. <https://doi.org/10.1038/s41467-019-13775-1>